Programa de Doctorado
Física y Ciencias del Espacio
Universidad de Granada

Evolutionary tracks of quiet-Sun magnetic features

Iker Sánchez Requerey

Memoria presentada para optar al grado de
Doctor en Astrofísica

Director
Dr. D. Jose Carlos del Toro Iniesta

Instituto de Astrofísica de Andalucía
Consejo Superior de Investigaciones Científicas
11 de diciembre de 2015

Examination date: 2015 December 11
Thesis supervisor: Dr. Jose Carlos del Toro Iniesta

ISBN: 978-84-9125-411-9
Some of the figures included in this document have been previously published in
The Astrophysical Journal

DECLARACIÓN

El doctorando **Iker Sánchez Requerey** y el director de la tesis **Dr. Jose Carlos del Toro Iniesta** garantizamos, al firmar esta tesis doctoral, que el trabajo ha sido realizado por el doctorando bajo la dirección del director de la tesis y, hasta donde nuestro conocimiento alcanza, en la realización del trabajo, se han respetado los derechos de otros autores a ser citados, cuando se han utilizado sus resultados o publicaciones.

Iker Sánchez Requerey
El doctorando

Dr. Jose Carlos del Toro Iniesta
El director

Granada, 30 de octubre de 2015.

RESUMEN

Esta tesis presenta un estudio de estructuras magnéticas fotosféricas del Sol en calma. Los campos magnéticos del Sol en calma se organizan a pequeñas escalas, evolucionan rápidamente y producen débiles señales de polarización. Estas propiedades físicas exigen medidas de la mayor resolución espacial y temporal posible junto con altas sensibilidad y precisión polarimétricas. Estas limitaciones instrumentales han causado que el origen y evolución de estas pequeñas estructuras permanezca aún relativamente desconocido.

IMaX (siglas de Imaging Magnetograph eXperiment o *imaginador* magnetográfico experimental) es un espectropolarímetro con imagen que voló sobre el círculo polar ártico a bordo del globo estratosférico SUNRISE. IMaX se diseñó para aliviar los problemas anteriores y ha proporcionado observaciones con la inédita resolución espacial de unos cien kilómetros. Al volar en la estratosfera, obtuvo series temporales de imágenes virtualmente libres del *seeing* que cubrían vastas zonas del Sol. Estas características son de verdad cruciales para estudiar la naturaleza altamente dinámica del magnetismo del Sol en calma.

La tesis reúne pruebas empíricas sobre la magnetoconvección a las escalas más pequeñas jamás observadas. Presentamos trazas evolutivas de diversas estructuras magnéticas del Sol en calma que se encuentran en continua interacción con la convección fotosférica. Específicamente, estudiamos 1) la formación y evolución de un elemento magnético aislado; 2) la dinámica de estructuras magnéticas multinúcleo; y 3) la relación entre estructuras magnéticas y sumideros persistentes sostenidos por la convección en las uniones de varias células mesogranulares.

Vista a la escala de unos cien kilómetros, la evolución de la estructura magnética aislada se contempla como un proceso complicado en el que intervienen muchos fenómenos. Su formación comienza cuando un pequeño bucle magnético emerge a la fotosfera en una zona de flujo ascendente granular. Sus pies son barridos rápidamente hacia las líneas intergranulares cercanas donde se encuentran previamente algunas otras estructuras de polaridad positiva. El pie negativo se cancela con una estructura positiva mientras que los flujos convectivos granulares desplazan el positivo y otros remanentes hacia un sumidero persistente.

Sus campos magnéticos se aglutinan en el sumidero dando forma a un nuevo elemento cuya intensidad de campo se encuentra en valores de equipartición con la densidad de energía cinética de los movimientos convectivos. El flujo descendente intergranular empieza entonces a incrementarse en la estructura magnética, a la vez que los gránulos circundantes la comprimen hasta que alcanza intensidades de kilogauss. Durante este proceso, aparece un punto brillante en el borde de la concentración de flujo casi coespacial con una pluma de flujo ascendente. El desarrollo del elemento magnético no se detiene ahí sino que resulta ser inestable. De hecho, muestra un comportamiento oscilatorio ya que su intensidad magnética decae y se refuerza con el tiempo.

Si nos centramos en estructuras magnéticas extendidas que albergan varios puntos brillantes en su interior, encontramos que son resolubles en varios núcleos magnéticos más elementales, cada uno de los cuales se encuentra relacionado con un punto brillante. Los núcleos más internos son intensos y verticales. Están rodeados por un conjunto de campos magnéticos más débiles e inclinados. Nosotros interpretamos esas estructuras como ramilletes de concentraciones de flujo en la baja fotosfera que se expanden con la altura hasta mezclarse en una única marquesina común en las capas fotosféricas altas. Los flujos convectivos granulares locales gobiernan la evolución de los núcleos magnéticos individuales. Mediante tal interacción, los núcleos se intensifican, se fragmentan y se funden de la misma manera que otras observaciones fotométricas informan que hacen las cadenas de puntos brillantes. Tal comportamiento evolutivo se traduce en oscilaciones de campo de la estructura global. Nosotros concluimos que tales oscilaciones —previamente descubiertas en pequeños elementos magnéticos del Sol en calma— obedecen más a la presión de los movimientos granulares que a modos oscilatorios propios de tubos delgados de flujo magnético.

Finalmente, analizamos la relación entre flujos mesogranulares, flujos descendentes localizados y campos magnéticos del Sol en calma. Comenzamos por un estudio estadístico de los sumideros. Algunos se muestran como remolinos mientras que otros despliegan flujos radialmente convergentes. Su distribución espacial los sitúa en los vértices de mesogránulos vecinos. Demostramos cuantitativamente que los campos más intensos tienden a concentrase en los sumideros. Por el contrario, los bucles magnéticos a pequeña escala no muestran distribución preferente alguna a escalas mesogranulares. Así mismo, analizamos en detalle uno de los mesogránulos y descubrimos que los bucles magnéticos que aparecen en el seno de su celda mesogranular pueden ser arrastrados por los flujos hacia uno de los vértices. Si nuestras observaciones se confirman, estos resultados pueden implicar que la formación de elementos magnéticos a través de la concentración de pies de bucles en vértices mesogranulares es ubicua en la superficie solar.

SUMMARY

This thesis presents a study of quiet-Sun magnetic features in the solar photosphere. Magnetic fields in the quiet Sun organize on small spatial scales, evolve very rapidly, and produce weak polarization signals. With these properties their observation requires high spatial and temporal resolution together with sensitive and accurate polarimetric measurements. It is for these instrumental limitations that the origin and evolution of these features remains elusive.

The Imaging Magnetograph eXperiment (IMaX) is an imaging spectropolarimeter that flew over the Artic Circle aboard the SUNRISE balloon-borne stratospheric mission. IMaX was designed to mitigate the above mentioned issues and has provided polarimetric observations with unprecedentedly high spatial resolution of a hundred kilometers. Flying in the stratosphere, it obtained stable, nearly seeing-free time series, and its imaging capabilities allowed to cover large areas of the Sun simultaneously. All these features are indeed crucial when studying the highly dynamic nature of the quiet-Sun magnetism.

The thesis gathers empirical evidence of magnetoconvection at the smallest scales ever observed. The evolutionary tracks of several different quiet-Sun magnetic structures in a continuous interaction with photospheric convection are presented. Specifically, we study 1) the formation and evolution of an isolated magnetic element; 2) the dynamics of multi-core magnetic structures; and 3) the relation between magnetic features and convectively driven, long living sinks at the junctions of several mesogranular cells.

Seen at a scale of one hundred kilometers, we find that the evolution of an isolated quiet-Sun magnetic element is a complex process where many phenomena are involved. The formation starts when a small-scale magnetic loop emerges through the solar surface in a granular upflow. Its footpoints are soon swept to nearby intergranular lanes where some, weak positive polarity patches are already present. The negative polarity footpoint cancels out with an opposite polarity feature while the positive one and other remaining patches are advected by converging granular flows toward a long-living sink. The magnetic fields agglomerate in the sink and a new element with a magnetic field strength in equipartition with the kinetic energy density of convective motions is formed. The intergranular downflow

then begins to increase within the magnetic feature while the surrounding granules compress it until kiloGauss field strengths are reached. During this process, a bright point appears at the edge of the flux concentration almost co-spatial with an upflow plume. The development of the magnetic element does not stop here since we discover that is indeed unstable. The magnetic element displays an oscillatory behavior as the field strength weakens and rises again with time.

Focusing on extended magnetic structures that harbor multiple bright points in their interiors, we find that they are resolvable into a series of more elemental inner magnetic cores, each of which appears related with a single bright point. The inner cores are strong and vertical. They all are surrounded by common, weaker, and more inclined fields. We interpret these structures as bundles of flux concentrations in the lower photosphere that expand with height to merge into a common canopy in the upper photospheric layers. The evolution of the individual magnetic cores is completely governed by the local granular convection flows. Through this interaction, they continuously intensify, fragment, and merge in the same way that chains of bright points in photometric observations have been reported to do. This evolutionary behavior results in magnetic field oscillations of the global entity. We conclude that the magnetic field oscillations previously discovered in small quiet-Sun magnetic elements correspond to the forcing by granular motions and not to characteristic oscillatory modes of thin flux tubes.

Finally, we analyze the relation between mesogranular flows, localized downdrafts, and quiet-Sun magnetic fields. We study first the statistical properties of the sinks. Some of them manifest as whirlpools while the others display radially symmetrical converging flows. Their spatial distribution reveals that they are located at the vertices between neighboring mesogranules. We quantitatively proof that the strongest fields tend to concentrate at sinks. Meanwhile, the small-scale magnetic loops do not show any preferential distribution at mesogranular scales. We also analyze one of the mesogranules in more detail and observe that magnetic loops appearing inside the mesogranular cell can be advected by horizontal flows toward its vertex. If confirmed by new observations, these results can imply that the formation of magnetic elements through the concentration of loop footpoints in mesogranular vertices is ubiquitous over the solar surface.

AGRADECIMIENTOS

Este trabajo de tesis me ha permitido conocer gente estupenda que, de una manera u otra, ha contribuido a que esto saliera adelante. Estos inolvidables cuatro años no hubieran sido posibles sin esas muchas personas a las que deseo agradecer en este apartado.

En primer lugar, mi más sincero agradecimiento a Jose Carlos por confiar siempre en mi, por mantener el equilibrio perfecto entre trabajo y amistad, y sobre todo por el apoyo, tanto a nivel profesional como personal, que siempre me ha dado. Ha sido un placer trabajar con un gran científico y persona como él.

Un especial agradecimiento a José Antonio por haberme recibido en mi primera estancia en el Instituto de Astrofísica de Canarias, por todos los conocimientos adquiridos con él, por su humildad y generosidad infinita. Sin duda, buena parte de esta tesis se la debo a él. También quiero agradecer a mi otro maestro del IAC, Basilio, por recibirme siempre con los brazos abiertos y por todo lo que me ha enseñado.

Si hay dos compañeros del Instituto de Astrofísica de Andalucía que han sido importantes para mi durante estos años, esos son sin duda Antxon y Gorosabel. Gracias Antxon por introducirme en vuestras tertulias desde el primer día que pisé la cafetería. Mila esker Javier zure alboan motz egiten ziren bidai guzti horiegatik. Beti izan zara eta izango zara eredu niretzat.

No puedo olvidarme en mis agradecimientos de todos los compañeros del equipo de rugby, en particular de aquellos que viajasteis a Vélez-Málaga, Jaén y Huelva, y sobre todo de los que os habéis convertido, con el tiempo, en grandes amigos fuera de Fuentenueva. De forma muy especial agradezco a Juan, Requena y Antorcha, por todos los buenos momentos vividos en Zacatín y Realejo. También a mis gudaris aventajados Pablo, Borja, Samu, Cañavate y Sylvain, fue un verdadero placer acogeros en mi tierra. Durante este último año se han convertido igualmente en imprescindibles mis amigos del roco Rubén, Charly y Borja, con los que he podido disfrutar de muchos buenos momentos de escalada.

Eta noski, nire erkerrik beroenak familiari, guraso eta arrebari bereziki, beti behar nuen babesa eta konfiantza eman didazuelako.

Llegamos al final de este capítulo, Marina. Gracias a ti, la distancia no ha sido un impedimento para sentir tu cariño cada día. Eres lo mejor que me llevo de este tiempo. Y como sucede en los libros, terminamos con este capitulo y ya asoma el siguiente a la vuelta de la esquina. Emaidazu berriro ongi etorria, gelditzeko nator eta!

CONTENTS

1

INTRODUCTION

The solar photosphere is a unique laboratory for studying ubiquitous astrophysical processes such as the interaction between plasma and magnetic fields. At this thin layer sunspots appear as the most outstanding footprints of solar activity in white light. Outside them, in the *quiet Sun*, only convective granules seem to pervade the vast majority of the solar surface. When seen in polarized light, however, a reticular network of magnetic structures is revealed. The regions between them, the so-called internetwork, have been thought to be devoid of magnetic signals for long. In the last years, the development of new instrumentation with steadily increasing spatial resolution and polarimetric sensitivity has turned our understanding of the internetwork magnetic fields upside down. From being basically quiet (i.e., non magnetic), it has started to exhibit an extraordinary magnetic activity. This revolution has been led by seeing-free, space-borne missions that together with the advent of sophisticated numerical models have led to a new age of discoveries. The aim of this thesis is to contribute to the understanding of the quiet-Sun magnetism based on the analysis of spectropolarimetric data from the SUNRISE balloon-borne solar observatory.

1.1 The solar structure

Deep in the solar core, at a temperature of $\sim 1.5 \times 10^7$ K, quantum-tunneling effect drives nuclear fusion between protons. The energy released through this process travels outward, first as radiation (in the innermost 70% of the solar radius) and later by convection (see textbooks by, e.g., Stix 2002; Foukal 2004). At the visible surface of the Sun, more than 90 % of the solar radiation escapes into space through radiative cooling of convective material. The escaping photons carry away some of the thermal energy of the rising plasma. As a

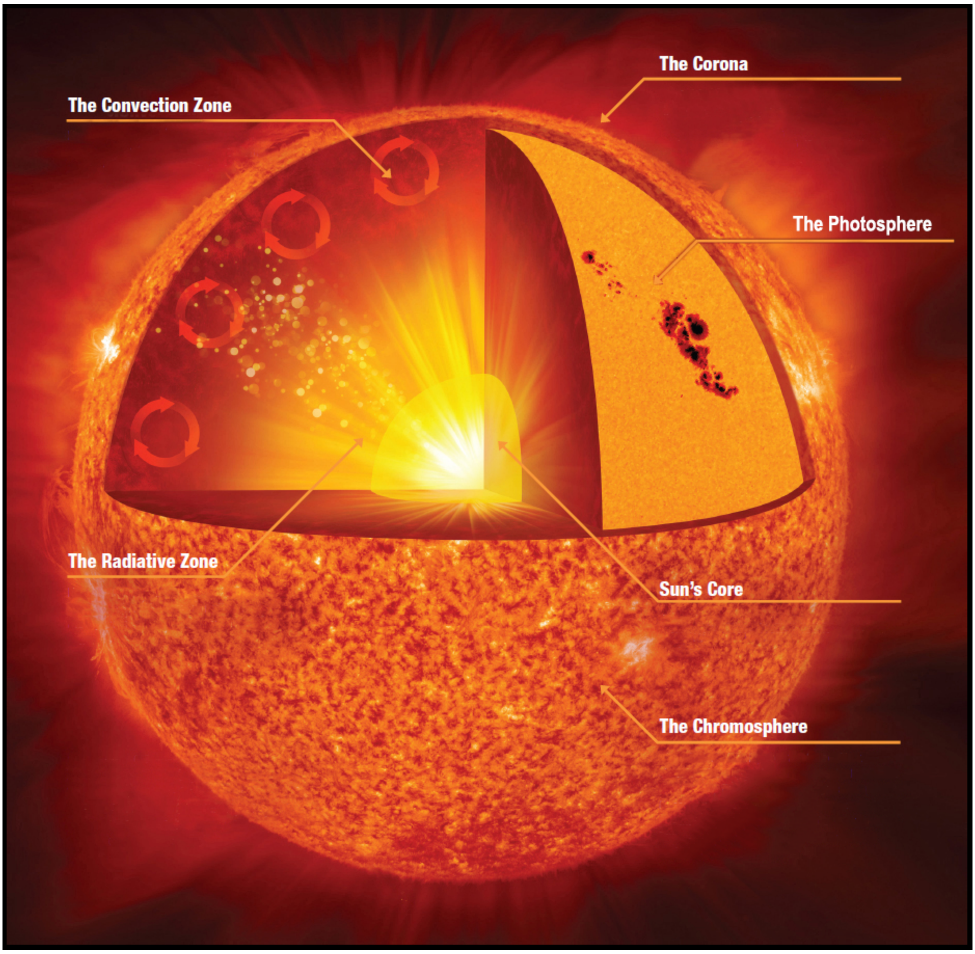

Figure 1.1: Illustration of the Sun structure from the core to the corona. See text for details. Image adapted from NASA/Jenny Mottar.

result, the plasma cools down, moves horizontally, and sinks back down into the Sun. This convection is observed as a granular pattern in the intensity variations of visible light images, where bright (hot) granules are surrounded by dark (cooler) lanes (see Nordlund et al. 2009, for a review). The bright granules have a diameter of approximately 1 Mm and are related with convective upflows, whereas the dark intergranular lanes are associated with convective downflows.

The solar atmosphere is the region from which photons escape into space. According to the different physical properties, it can be divided in three main layers, namely, the *photosphere*, the *chromosphere*, and the *corona*. The base of the photosphere (also called the solar surface) is defined as the region where the continuum optical depth, τ_c, at 500 nm, is unity. Its effective temperature is $\sim$5700 K and it spans vertically for about 500 km. At this height, the temperature reaches its minimum value $\sim$4500 K (temperature minimum; e.g., Foukal 2004). Starting from the temperature minimum, the chromosphere is a $\sim$1500 km wide layer where a broad temperature plateau of $\sim 10^4$ K (e.g., Stix 2002) is reached. The particle density drops rapidly from $10^{23}\,\mathrm{m}^{-3}$ to $10^{19}\,\mathrm{m}^{-3}$ in this layer. Above the chromosphere the solar corona extends from the top of a narrow *transition region* (within which the temperature abruptly increases from $\sim 10^4$ K to $\sim 10^6$ K) out into the *solar wind* (e.g., Priest 2014). The Sun structure from the core to the corona is illustrated in Figure1.1.

The heating of the upper solar atmosphere is one of the most important problems in astrophysics (Klimchuk 2006; Parnell & De Moortel 2012). There is still no clear consensus about the mechanism (or mechanisms) which heats the chromosphere to 10^4 K and the corona to 10^6 K, in comparison with the 6000 K photosphere. The difficulties arises from the fact that the different atmospheric layers (which differ strongly in their plasma properties) are not energetically isolated from the others and, rather, the whole solar atmosphere forms a highly coupled system. Since the magnetic field of the Sun connects the different atmospheric layers, it is generally accepted that the solar magnetism plays a key role in the chromospheric and coronal heating. The magnetic field is created in the solar interior, is measured with highest sensitivity on the photosphere and is responsible for most of the dynamical processes in the solar atmosphere (see Wiegelmann et al. 2014, for a review).

1.2 Quiet-Sun magnetic fields

Magnetic fields in the Sun were first discovered in sunspots by Hale (1908, see Del Toro Iniesta 1996 for a review of historical details) and later in their near vicinity (Babcock & Babcock 1955), at plage regions (also called faculae when seen in the solar limb). In the solar photosphere sunspots appear darker (cooler) than their surroundings while plage regions are seen as conspicuous bright (hot) areas around sunspots. The non-stationary evolution of magnetic fields at these regions was soon related with the solar activity, which manifests as eruptive processes, coronal activity, and geomagnetic disturbances, among others. This connection between solar activity and magnetic fields gave rise to the concept of *active* region. Since then, the areas of the solar surface outside sunspot and plage regions are termed the *quiet Sun* (see recent reviews by de Wijn et al. 2009; Sánchez Almeida & Martínez González 2011; Martínez Pillet 2013; Bellot Rubio & Orozco Suárez 2015).

The Sun was considered non magnetic everywhere outside active regions until the 1970's when a substantial amount of the solar magnetic flux was found. In particular, Howard & Stenflo (1972) estimated that more than 90% of the total magnetic flux at the solar surface is concentrated in the boundaries of supergranules, which have diameters of about 30 Mm (see Rieutord & Rincon 2010, for a review). Full disk longitudinal magnetograms reveal that the magnetic fields at these locations display a reticular pattern which forms the so-called magnetic *network* (see Figure 1.2 (b)). The magnetic field in the network has field strengths of the order of kiloGauss (e.g., Stenflo 1973; Wiehr 1978; Solanki & Stenflo 1984; Stenflo & Harvey 1985; Solanki et al. 1987; Grossmann-Doerth et al. 1996). Weaker magnetic signals were soon discovered in the interiors of supergranular cells (Livingston & Harvey 1971, 1975; Smithson 1975) and the term intranetwork (Martin 1984) or *internetwork* (Lites et al. 1993) was created. Internetwork (IN) magnetic fields cover the vast majority of the solar surface and they have been estimated to contribute the solar magnetic flux with $\sim 10^{26}$ Mx per day (Zhou et al. 2013), over 4 orders of magnitude higher than the active region contribution.

At the solar disk center, and under the weak field regime (e.g., Landi Degl'Innocenti & Landolfi 2004), the circular and linear polarization states of the outcoming light are mostly produced by the longitudinal and transverse (horizontal) components of the magnetic field, respectively. In the jargon of solar physicists, differences between circular polarization maps at two wavelengths are commonly known as longitudinal magnetograms where positive (negative) polarities stand for magnetic fields pointing toward the observer (down into the Sun). Observed in circularly polarized light, IN magnetic fields appear as small discrete magnetic features (*magnetic elements*) with mixed polarities (Livingston & Harvey 1975). The lifetime of magnetic elements range from 1 to 20 minutes (Zhou et al. 2010), but many of them survive several hours while they interact with other features (de Wijn et al. 2008). As soon as linearly polarized light was measured, a new component of the quiet Sun magnetism became apparent in the form of arcsecond scale linear polarization patches (Lites et al. 1996). These patches, or Horizontal Internetwork Fields (HIFs) as they were called, are very dynamic (Danilovic et al. 2010b), with a lifetime of less than 10 minutes, comparable to that of granules. Some of them appear between two opposite-polarity patches. Such structures are interpreted as low-lying (photospheric) magnetic loops (Martínez González et al. 2007) where the two opposite circular patches and the linear one are created by the two footpoints and the apex of the loop, respectively (Centeno et al. 2007). A significant fraction of them emerge through the solar surface in the form of Ω-loops (Martínez González & Bellot Rubio 2009). They carry an enormous amount of flux to the photosphere, with values of 1.1×10^{24} Mx day^{-1} (Martínez González & Bellot Rubio 2009) and 9.8×10^{24} Mx day^{-1} (Jin et al. 2009) over the solar surface for Ω-loops and HIFs, respectively. About 23 % of the loops reach the chromosphere and thus may supply a substantial amount of energy to the upper atmospheric layers (Martínez González & Bellot Rubio 2009).

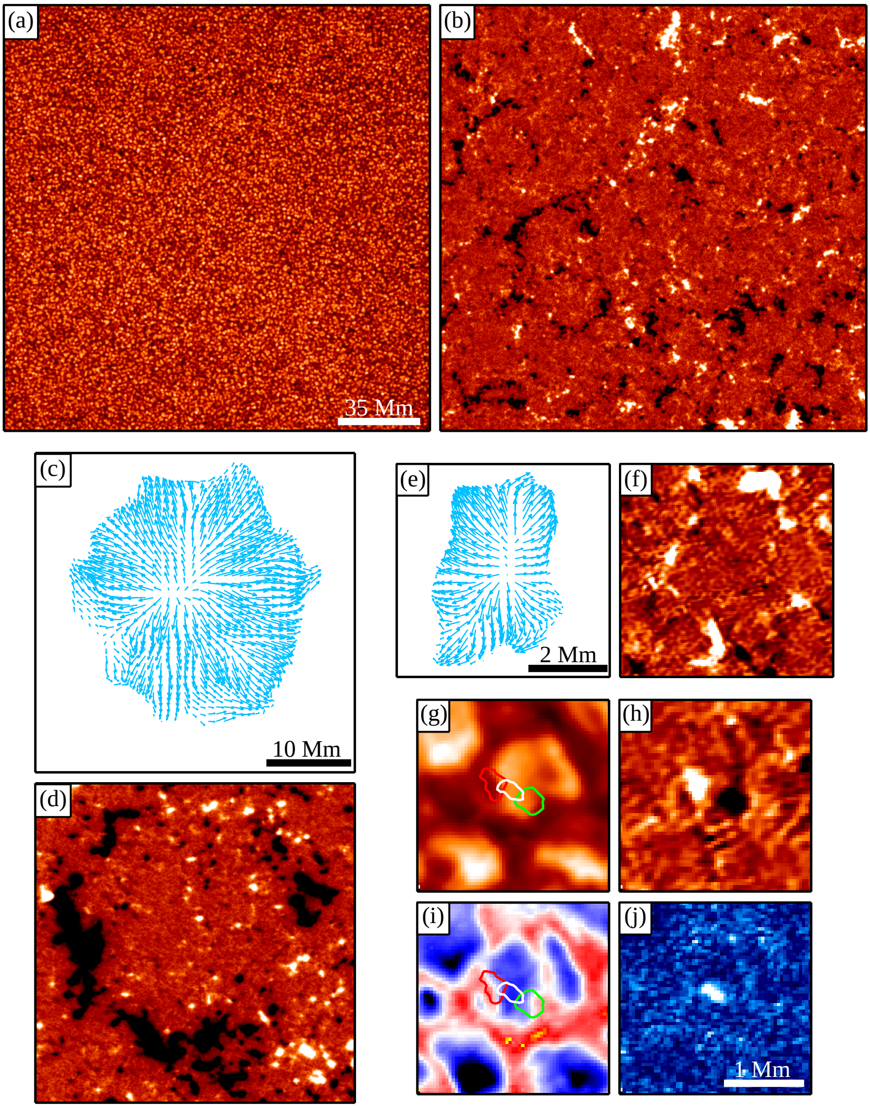

Figure 1.2: Quiet Sun at the disk center as observed by SDO/HMI: (a) continuum intensity; (b) longitudinal magnetogram. Supergranular cell as observed by *Hinode*/NFI (courtesy Milan Gošić): (c) supergranular flow field; (d) longitudinal magnetogram. Mesogranular cell as observed by Sunrise/IMaX: (e) mesogranular flow field, (e) longitudinal magnetogram. Small-scale Ω-loop as observed by Sunrise/IMaX: (g) continuum intensity; (h) longitudinal magnetogram; (i) line-of-sight velocity; (j) linear polarization. Red, green, and white contours represent positive polarity, negative polarity, and linear polarization patches, respectively.

1.2.1 Spatial distribution of quiet-Sun magnetic fields

Figure 1.2 shows images from quiet-Sun regions observed with different instruments and spatial resolutions. Panel (a) and (b) display a wide quiet-Sun area at disk center observed with the Helioseismic and Magnetic Imager (HMI; Scherrer et al. 2012) aboard the Solar Dynamics Observatory (SDO; Pesnell et al. 2012) at the spatial resolution of $1''$. The solar surface convection is observed as a granular pattern in the continuum intensity image of panel (a). The co-spatial longitudinal magnetogram illustrates the reticular pattern produced by the magnetic network in panel (b). An individual supergranular cell is shown in Figure 1.2 (c) and (d) as observed with the Narrowband Filter Imager (NFI; Tsuneta et al. 2008) on board the *Hinode* satellite (Kosugi et al. 2007). The panels display the horizontal flow field map of the supergranular cell and the corresponding longitudinal magnetogram, respectively. The horizontal supergranular flow goes from the center of the cell toward its boundary where the network patches are observed. With a spatial resolution of about $0.''3$, many IN magnetic elements are also found in the interior of the magnetic network. Different features of such IN areas are also displayed in panels (e)–(j) with a higher spatial resolution of $0.''15$–$0.''18$. These images have been acquired with the Imaging Magnetograph eXperiment (IMaX; Martínez Pillet et al. 2011a) aboard the SUNRISE (Solanki et al. 2010; Barthol et al. 2011) balloon-borne solar observatory. Detailed information of the different panels is given later in the text.

The ratio between the gas pressure and the magnetic pressure is called the plasma β. β is clearly greater than unity in the solar interior and much less than one in the corona. Typically, the photosphere is identified as the layer where $\beta \sim 1$. However, many places in the photosphere should have $\beta \geq 1$ because many quiet-Sun magnetic structures are observed to evolve in the solar surface influenced by granular motions. Long-living IN elements move radially toward the network (de Wijn et al. 2008) as they are advected by horizontal supergranular flows (Orozco Suárez et al. 2012). During their migration, IN magnetic elements interact frequently with other structures (de Wijn et al. 2008) and they are continuously being buffeted by neighbouring granules (Manso Sainz et al. 2011), thus producing random motions at shorter time scales. Many magnetic elements disappear inside the IN by cancellations or fading below the detection limit (Gošić et al. 2015), whereas others survive long enough to reach the network (Wang & Zirin 1988; Orozco Suárez et al. 2012; Gošić et al. 2014). The latter ones merge (cancel) with same-polarity (opposite-polarity) network flux concentrations and modify the network flux budget. Using stable longitudinal magnetogram observations with durations longer than 20 hours, Gošić et al. (2014) found that merging processes appear to be dominant. Through this positive net flux contribution, the IN magnetic elements could replace the entire network flux in approximately 1 day.

Between the well-known granular and supergranular convective scales (see e.g., Nordlund et al. 2009; Rieutord & Rincon 2010, for reviews), many observations suggest the existence of an intermediate scale of convection (5-10 Mm of size, November et al. 1981) known as mesogranulation (November et al. 1981; Simon et al. 1988; Title et al. 1989; Brandt et al. 1991; Muller et al. 1992; Roudier et al. 1998; Shine et al. 2000; Leitzinger et al. 2005). Figure 1.2 (e) displays the horizontal velocity flow field of a single mesogranule. It depicts a very similar shape as that of a supergranule, but with one order of magnitude smaller size. Despite many investigations, there is an ongoing debate about whether mesogranulation is a distinct scale of solar convection (Rieutord et al. 2000; Cattaneo et al. 2001; Domínguez Cerdeña 2003; Rast 2003; Roudier et al. 2003; Roudier & Muller 2004; Matloch et al. 2009, 2010; Yelles Chaouche et al. 2011; Bushby & Favier 2014). Others suggest them to be persistent granule associations that produce mesogranular-sized positive horizontal flow divergences. Specifically, they have been related to “trees of fragmenting granules” (Roudier et al. 2003; Roudier & Muller 2004), which consist of a family of repeatedly exploding granules. Regardless of their nature, it has recently become clear that magnetic elements accumulate at mesogranular boundaries (Yelles Chaouche et al. 2011). Roughly 85 % of the pixels harboring longitudinal magnetic fields[1] with values larger than 100 G are located in the near neighborhood of mesogranular lanes. Figure 1.2 (e)–(f) show an example where many magnetic features are observed all around a mesogranule.

Linear polarization patches seem to be also organized on mesogranular scales (Lites et al. 2008; Danilovic et al. 2010b). Visual evidence has been obtained showing that they are co-spatial with mesogranular boundaries (Ishikawa & Tsuneta 2010). However, quantitative information of such a relation is still missing. The most exhaustive statistical analysis of the evolution of HIFs has been performed by Danilovic et al. (2010b). They found that these features are preferentially located at the edges of granules, with most of them falling into the intergranular lanes at some point during their evolution. This is consistent with the evolution found for emerging magnetic loops, which appear first within a granule and then are swept into the intergranular lanes (Centeno et al. 2007). Figure 1.2 (g)-(j) shows an example of one of these Ω-loops emerging above a granule. At the center of panel (h) the two opposite polarity footpoints are observed. These footpoints are connected by a small linear polarization patch in panel (j). Their contours are shown on the continuum intensity and line-of-sight velocity maps, panel (g) and (i), respectively. The loop is rising within a convective upflow as represented by blue areas in the velocity map.

---

[1] Whenever we loosely speak in this thesis about the *longitudinal magnetic field* we mean, indeed, the longitudinal component of the magnetic field.

1.2.2 Magnetic field strength and inclination in the IN

The question about whether IN magnetic fields are weak or strong was a matter of a heated debate over the past decade (see e.g., de Wijn et al. 2009; Bellot Rubio & Orozco Suárez 2015, for a review). The discussion was primarily motivated by the contradictory results obtained from ground-based observations when different spectral regions were used. While the field strengths inferred through visible Fe I lines at 630 nm used to favor kG fields (Sánchez Almeida & Lites 2000; Domínguez Cerdeña et al. 2003a,b; Lites & Socas-Navarro 2004), those obtained from near-IR lines used to derive hG fields (Lin 1995; Lin & Rimmele 1999; Khomenko et al. 2003). Theoretical arguments suggested that visible Fe I lines at 630 nm could be affected by the noise (Bellot Rubio & Collados 2003) and crosstalks between the thermodynamic and magnetic parameters (Martínez González et al. 2006). In both cases the reason was attributed to the lower magnetic sensitivity of the visible lines.

The controversy started to be elucidated with the development of new solar instruments with improved angular resolution. Thanks to its unprecedented stability, a major contribution was carried by the Japanese *Hinode* satellite. The Spectro-Polarimeter (SP; Lites et al. 2013) on board *Hinode*'s 0.5-m Solar Optical Telescope (SOT; Tsuneta et al. 2008) performs full Stokes vector spectropolarimetric observations of the Fe I lines at 630 nm with a spatial resolution of 0.″32. The analysis of these data through Milne-Eddington (ME) inversions of the radiative transfer equation (e.g., Orozco Suárez et al. 2007a,b; Asensio Ramos 2009; Borrero & Kobel 2011; Jin et al. 2012; Orozco Suárez & Bellot Rubio 2012) showed a predominance of hG fields, in agreement with those derived from ground-based measurements of near-IR lines. Same results were found by Martínez González et al. (2008) trough the combined inversion of visible and near-IR lines measured simultaneously at the same telescope. These new results reconciled visible and near-IR measurements and a consensus was reached regarding the IN field strength distribution.

The first inversions of the *Hinode*/SP data also revealed a surprisingly large amount of inclined magnetic fields (e.g., Orozco Suárez et al. 2007b; Lites et al. 2008), suggesting that the orientations of IN fields are not isotropically distributed. Soon doubts concerning the reliability of the magnetic parameters inferred from ME inversions appeared. Some authors suggested that the large abundance of horizontal fields could be biased (de Wijn et al. 2009; Asensio Ramos 2009; Borrero & Kobel 2011). Since a large fraction of the analyzed pixels have linear polarization signals dominated by noise, they concluded that most of the weak horizontal fields were not real, but due to noise. These doubts were tackled with both solid theoretical arguments (Del Toro Iniesta et al. 2010) and new high sensitivity *Hinode*/SP measurements (Orozco Suárez & Bellot Rubio 2012). In the latter, they used four times less noisy data and they confirmed the idea that IN fields are weak and

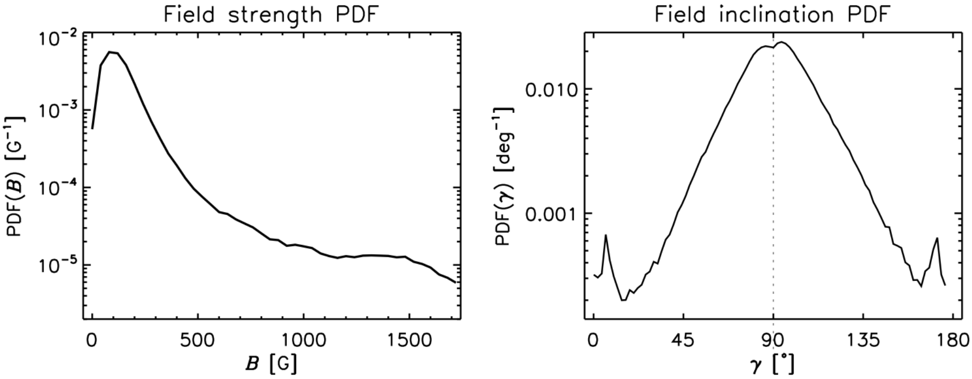

Figure 1.3: Magnetic field strength (left) and inclination (right) probability density functions for internetwork regions resulting from a ME inversion of spectropolarimetric data obtained with the *Hinode*/SP at a noise level of 3×10^{-4}. Only pixels whose Stokes profile amplitude exceed a polarization threshold of 4.5 times the noise level were included in the analysis. From Orozco Suárez & Bellot Rubio (2012).

very inclined. The magnetic field strength and inclination distributions resulting from these observations are depicted in Figure 1.3. The distributions show that most of the magnetic fields have hG strengths and horizontal inclinations (90°). Interestingly, the field strength distribution extends up to kG values and two little, nearly vertical, humps are observed at inclination values close to 0° and 180°. If the related field strengths are weak, they could be associated with the footpoints of small-scale magnetic loops. If instead their fields are strong, they could be related with kG magnetic elements.

1.2.3 Formation of magnetic elements

The formation of strong magnetic elements is thought to be well understood from a theoretical point of view. Convective eddies expel magnetic fields into intergranular lanes (Weiss 1966). The flux is there concentrated roughly up to the equipartition field strength, $\sim 500\,$G, the level where the magnetic energy density becomes equal to the kinetic energy density of granular flows. The enhanced magnetic pressure suppresses the convective energy transport and the gas cools down inside the flux concentration (Webb & Roberts 1978; Spruit & Zweibel 1979). Attracted by gravity, the dense cool gas sinks down and leads to the partial evacuation of the magnetic feature (*convective collapse*; Parker 1978). The gas pressure drops inside the magnetic element and it is compressed by surrounding plasma. Through this process, the flux concentration is further intensified up to 1–2 kG field strengths (Spruit 1979) and the horizontal pressure balance is again established.

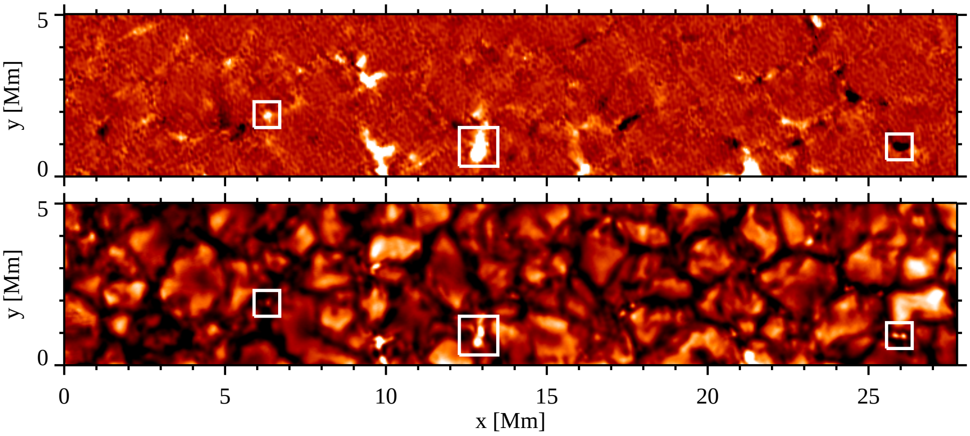

Figure 1.4: Co-spatial images from both the IMaX and SuFI instruments aboard the SUNRISE balloon-borne solar observatory. Top panel: longitudinal magnetogram as observed by IMaX. Bottom panel: CN-band image at 388 nm as observed by SuFI. Examples of magnetic concentrations with associated bright points are marked by white boxes. The left most one shows a small magnetic element with a related BP, while the two right most magnetic features contain two BPs.

One observation of such an intensification process from equipartition to kG values and a simultaneous strong downflow in a magnetic element has been interpreted as an evidence for a convective collapse (Nagata et al. 2008). Realistic magnetoconvection models show that magnetic fields are advected by convective motions to well localized sinks located at the vertices of granular and mesogranular downflow lanes (Stein & Nordlund 2006; Danilovic et al. 2010a). There, they are concentrated and intensified by converging granules. Observation of the entire process requires high resolution spectropolarimetric images over relatively long time periods. Such observations have recently been achieved with the balloon-borne SUNRISE observatory.

1.2.4 Bright points and magnetic flux tubes

Strong magnetic concentrations in the solar photosphere show up as small point-like bright features in intergranular lanes (e.g., Berger & Title 2001; Sánchez Almeida et al. 2010; Viticchié et al. 2010). Figure 1.4 displays a magnetogram co-spatial with a CN-band filtergram. White boxes show three clear examples where magnetic structures appear associated with bright points (BPs). The largest magnetic features can be related with BP groups (see the two rightmost boxes). Based on a recent comparison between SUNRISE observations and 3D magnetohydrodynamical (MHD) simulations, Riethmüller et al. (2014) deduced that BPs are associated with kG magnetic elements.

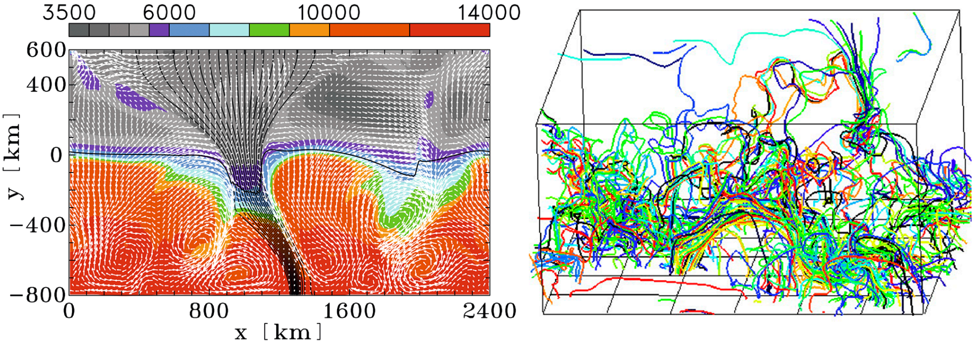

Figure 1.5: Left panel: 2D MHD model of a flux tube. The temperature (background image), the velocity field (arrows), and magnetic field lines (thin lines). The thick horizontal curve indicates continuum optical depth unity. From http://www.kis.uni-freiburg.de/~steiner/. Right panel: 3D magnetoconvection simulation. Magnetic field lines of a snapshot viewed from an angle. From Stein & Nordlund (2006).

Magnetic concentrations in the solar surface are generally modeled by magnetostatic *flux tubes* (Spruit 1976). Strong magnetic field inhibits the convective motions and results in a partially evacuated tube (see Section 1.2.3). Since the energy input from below is reduced, the temperature is lower than in the outside plasma at equal geometric height. The gas pressure is also lower in the tube and so is the opacity. Therefore, the optical depth unity level is depressed inside the tube and it is located at a geometrically deeper layer compared to surrounding plasma (Wilson depression effect). The temperature is higher at deeper layers but still cooler than in the tube at equal optical depth. The less opaque magnetic flux tube also causes a lateral inflow of radiation into their evacuated interiors. This horizontal influx of radiation is sufficient to heat the tube up to a temperature which is higher than the photospheric temperature at the same optical depth. As a consequence, the flux concentration appears brighter than its surrounding material. This is true for small magnetic structures as those found in the quiet Sun. At larger scales, the influx of radiation only heats a thin part of the outer surface, and thus sunspots appear dark in the solar photosphere.

More sophisticated 2D models of flux tubes show that they are far for being static (Steiner et al. 1996, 1998). The flux tubes are instead very dynamic, they move and bend continuously as they are buffeted by surrounding granules. An example of such a flux tube model is displayed in the left panel of Figure 1.5, where the Wilson depression effect is clearly shown by the horizontal thick black curve, which indicates the location of the continuum optical depth unity. In 3D magnetoconvection simulations, the concept of isolated flux tube is not valid anymore (Stein & Nordlund 2006). The topology is rather complex, coherent bundles of field lines are only seen at the surface and they are connected to many different locations both below and above the surface (see right panel in Figure 1.5).

From the observational point of view, BPs have been widely used as proxy diagnostics to study the evolution of magnetic elements (e.g., Muller & Roudier 1992; Roudier et al. 1994; Berger & Title 1996; de Wijn et al. 2005; Jafarzadeh et al. 2013; Utz et al. 2014). This has been primarily motivated by their small point-like nature which makes them easier to be tracked compared to the more extended magnetic structures. In addition, intensity tracers are far more easier to be observed at high angular resolution than the associated magnetic features. Discerning the vector magnetic field requires high precision polarimetric measurements only achievable under extremely stable seeing conditions. Molecular lines such as the Fraunhofer G band and CN band have been extensively used due to their high contrast. Those lines are strongly weakened inside flux concentrations and when integrated over the passband the BPs appear much brighter than in continuum images (Kiselman et al. 2001). Intensity tracers have however many limitations as strong flux concentrations are required to form a bright point (Berger & Title 2001; Ishikawa et al. 2007; Riethmüller et al. 2014). This is not, nevertheless, a sufficient condition, as many strong magnetic elements do not have a related BP. The contrast of BPs decreases as the inclination angle between the vector magnetic field and the line of sight increases (Beck et al. 2007a). In addition, during their lifetime, magnetic structures can be related to different BPs at different times. The magnetic flux exists before and after the appearance and disappearance of each individual BP (de Wijn et al. 2005). All these restrictions call for the need of sensitive polarimetric observations.

1.2.5 Origin of IN magnetic fields

Whenever there is a continuous injection of magnetic flux at the solar surface, the existence of strong magnetic elements in the convective downflows can be found (Section 1.2.3). The fundamental question now is to know where this flux comes from. One possibility is that the quiet Sun magnetic field is recycled from decaying active regions as the debris fragments of magnetic flux submerge and rise again in other places of the solar surface. In fact, magneto-convection models that study the interaction of convective flows with an imposed magnetic field can reproduce many of the observed quiet-Sun features (e.g., Khomenko et al. 2005; Stein & Nordlund 2006; Bushby et al. 2008), including the concentration of magnetic flux in mesogranular lanes (Stein & Nordlund 2006). If the input field is coming from decaying active regions, then it would be generated by the global solar dynamo and a dependence on the solar cycle would be expected. However, it has been found that IN longitudinal magnetic field shows little correlation with the strength of the surrounding network field (Lites 2011), and also very slight dependence on the sunspot number (Jin & Wang 2015a). In addition, the occurrence rate of linear polarization patches is the same in both the quiet Sun and in plage regions (Ishikawa & Tsuneta 2009). It does not vary along the solar cycle (Jin & Wang 2015b). Another possibility is that IN magnetic fields are generated locally through a small-scale dynamo action driven by near-surface convective flows (Petrovay & Szakaly 1993). The small-scale dynamo can operate on both granular (Cattaneo 1999; Vögler & Schüssler 2007) and mesogranular scales (Bushby et al. 2012; Bushby & Favier 2014; Rempel 2014). However, it is more efficient when mesogranulation is also present (Bushby & Favier 2014). In fact, the photospheric magnetic energy is doubled as a strong mesogranular network is formed (Rempel 2014).

1.3 Motivation of this work

Our understanding of the dynamics and evolution of quiet-Sun magnetic fields has been limited by the need of stable seeing conditions to achieve high spatial resolution together with sufficient stability and polarimetric sensitivity. One possibility to fulfill this requirement is to fly a telescope outside the perturbing action of the Earth atmosphere.

The Imaging Magnetograph eXperiment is a spectropolarimeter with full polarization and imaging capabilities which is designed to fly as a post-focus instrument of the 1-m telescope aboard the SUNRISE balloon-borne solar observatory. It provides nearly diffraction limited observations of the Stokes profiles of the solar photospheric Fe I line at 525.02 nm. Being stratospheric (the balloon reached 40 km of altitude), SUNRISE has been able to get rid of most of the atmosphere, hence improving the image quality. An image stabilization system has maintained the spatial resolution for long periods of time, thus allowing to explore the evolution of photospheric features. With an unprecedented spatial resolution of $0\overset{\prime\prime}{.}15$–$0\overset{\prime\prime}{.}18$ (after reconstruction) and high time cadence of 33 s, we have for the first time the opportunity to study the evolution of spatially resolved quiet-Sun magnetic structures (Lagg et al. 2010).

IMaX is already leading new insights into the magnetism and convection of the quiet-Sun photosphere (e.g., Borrero et al. 2010; Bonet et al. 2010; Khomenko et al. 2010; Steiner et al. 2010; Martínez González et al. 2011). The Solar Physics Group at the Instituto de Astrofísica de Andalucía (IAA-CSIC) has participated in the design, development, and construction of IMaX, and on its scientific definition and analysis. The present thesis is devoted to the study of quite-Sun magnetic fields through the exploitation of these high-quality data. We analyze the evolution of several different quiet-Sun magnetic structures, and we characterize their spatial distribution in the solar photosphere. Specifically, we study 1) the formation and evolution of an isolated magnetic element; 2) the dynamics of multi-core magnetic structures; and 3) the relation between magnetic features and convectively driven, long living sinks at the junctions of several mesogranular cells.

2

SPECTROPOLARIMETRY

Some basic concepts of spectropolarimetry are introduced in this Chapter. The knowledge of the measurements and analysis of light will be especially useful later in this thesis in order to better understand the inference of physical quantities such as solar magnetic fields and line-of-sight (LOS) velocities. The Chapter includes a mathematical formulation of polarized light, an overview of the spectropolarimetric measurements carried out with the Imaging Magnetograph eXperirnent, and a description of the radiative transfer equation in the presence of a magnetic field. For further reading on spectropolarimetry, we refer to Del Toro Iniesta (2003).

2.1 Measurements of polarized light

In a homogeneous isotropic medium, Maxwell's equations ensure that both the electric (**E**) and magnetic field vectors, satisfy the homogeneous wave equation

$$\nabla^2\mathbf{E} - \frac{\varepsilon\mu}{c^2}\ddot{\mathbf{E}} = 0. \tag{2.1}$$

The simplest solution for that equation is a plane wave, where the electric and magnetic vectors are orthogonal to each other in the plane perpendicular to the ray path direction. This is a good approximation to more elaborate solutions (e.g., spherical waves) when the observer is far enough from the light source, as is the case for most astrophysical applications. A polychromatic light beam can be described as the superposition of monochromatic (single frequency) plane waves. If the beam propagates through the z-axis, at a given point in the space, the description of the electric field of a polychromatic wave can always be put in the form

$$\begin{aligned} E_x(t) &= \mathscr{E}_x(t)\ e^{-i(\omega t-\delta_x(t))}, \\ E_y(t) &= \mathscr{E}_y(t)\ e^{-i(\omega t-\delta_y(t))}, \\ E_z(t) &= 0, \end{aligned} \tag{2.2}$$

where $\mathscr{E}_x(t)$ and $\mathscr{E}_y(t)$ represent the amplitudes of the x and y components, $\delta_x(t)$ and $\delta_y(t)$ are their phase shifts, and ω the angular frequency. For simplicity we omit the argument (t) hereafter.

These quantities, however, are not measurable with available devices because they are complex, and the polarization properties of any electromagnetic wave is better described by the Stokes parameters:

$$\begin{aligned} I &= \kappa(\langle\mid E_x\mid^2\rangle+\langle\mid E_y\mid^2\rangle) = \kappa\langle\mathscr{E}_x^2+\mathscr{E}_y^2\rangle, \\ Q &= \kappa(\langle\mid E_x\mid^2\rangle-\langle\mid E_y\mid^2\rangle) = \kappa\langle\mathscr{E}_x^2-\mathscr{E}_y^2\rangle, \\ U &= \kappa(\langle E_x^* E_y\rangle+\langle E_x^* E_y\rangle) = 2\kappa\langle\mathscr{E}_x\mathscr{E}_y\cos\delta\rangle, \\ V &= i\kappa(\langle E_x^* E_y\rangle-\langle E_x^* E_y\rangle) = 2\kappa\langle\mathscr{E}_x\mathscr{E}_y\sin\delta\rangle, \end{aligned} \tag{2.3}$$

where κ is a dimensional constant which translates the Stokes parameters into intensity units, $\langle\rangle$ means time average, * stands for complex conjugate, and $\delta=\delta_x-\delta_y$ is the phase difference between the two components. Note that all four Stokes parameters are real and have dimensions of energy. They are thus measurable and they must obey the inequality: $I^2 \geq Q^2+U^2+V^2$. Although not straightforward, the above inequality can be interpreted as a proof that polychromatic light is not always polarized. As a matter of fact, any polychromatic beam can be decomposed in two, one totally unpolarized and another totally polarized, whose energy is given by the right-hand side of the inequality. It can therefore be read as "the energy content of any polychromatic beam is always larger than or equal to the energy content of its polarized component". When equality holds, light is said to be *totally polarized*, whereas when $Q=U=V=0$, light is said to be *natural* or *completely unpolarized*. Otherwise, the light beam is said to be *partially polarized*.

In order to measure the Stokes parameters two specific optical devices are needed: a *linear polarizer* and a *linear retarder*. A linear polarizer is a device which selectively allows the passage of completely linearly polarized light at an angle θ. This characteristic angle marks the orientation of the so-called *optical axis* of the linear polarizer. The electric field aligned to the optical axis is completely transmitted; while the orthogonal component is completely absorbed. So that at the output, the magnitude of the new electric beam is given by:

$$E_\theta = E_x \cos\theta + E_y \sin\theta. \tag{2.4}$$

On the other hand, a linear retarder is an optical device which introduces a *retardance* (phase difference) δ between both orthogonal components of $\mathbf{E}$ associated to the beam. The phase-shifted component is parallel to the so-called *slow axis* and perpendicular to the *fast axis*. If we consider a retarder whose fast axis is aligned with the x-axis of the reference coordinate system, the outgoing E'_x and E'_y are

$$\begin{aligned} E'_x &= E_x, \\ E'_y &= E_y\, e^{i\delta}. \end{aligned} \tag{2.5}$$

Now, if we consider an optical system having those two devices in a row (first the retarder and then the polarizer), the output electric vector amplitude is given by:

$$E_\theta = E_x \cos\theta + E_y \sin\theta e^{i\delta}, \tag{2.6}$$

and the measurable beam intensity is

$$I_{\text{meas}} = \langle E_\theta E^*_\theta \rangle. \tag{2.7}$$

Making use of the Stokes parameters (2.3), and assuming that $\kappa = 1$, the time-averaged electric field square modulus can be recast in the more useful form

$$I_{\text{meas}}(\theta,\delta) = \frac{1}{2}(I + Q\cos 2\theta + U\cos\delta \sin 2\theta + V\sin\delta \sin 2\theta). \tag{2.8}$$

Accordingly, we can infer I, Q, U and V by just varying θ and δ. This can be done by using different optical devices and setups. In the specific case of our optical system,

$$\begin{aligned} I &= I_{\text{meas}}(0,0) + I_{\text{meas}}(\frac{\pi}{2},0), & Q &= I_{\text{meas}}(0,0) - I_{\text{meas}}(\frac{\pi}{2},0), \\ U &= I_{\text{meas}}(\frac{\pi}{4},0) - I_{\text{meas}}(\frac{3\pi}{4},0), & V &= I_{\text{meas}}(\frac{\pi}{4},\frac{\pi}{2}) - I_{\text{meas}}(\frac{3\pi}{4},\frac{\pi}{2}), \end{aligned} \tag{2.9}$$

since the equations for Q, U, and V are differences, these parameters are zero for the case of natural light. Stokes I is the total intensity, namely, the sum of any two orthogonal polarization states. Polarization information is provided by Q, U, and V. Specifically, Q is the difference between the intensities of linear components at 0° and 90°, U is the difference between the intensities of linear components at 45° and 135°, and V is the difference between the intensities of right-handed and left-handed circularly polarized light. The Stokes parameters can be grouped in the so-called *Stokes vector*,

$$\mathbf{I} = (I, Q, U, V)^T, \tag{2.10}$$

which describes the polarized state of the light, and T represents the transpose.

2.2 Spectropolarimetry with IMaX

So far we know how to measure the polarization state of light by means of two especially suited devices. Once we know the mathematical basis of the Stokes parameters, we are in a position to introduce a little some real solar spectropolarimetry and, in particular, on that performed by the Imaging Magnetograph eXperiment (IMaX; Martínez Pillet et al. 2011a). In this Section we will focus on its optical setup, designed for retrieving the full Stokes vector. Further details on IMaX observational properties will be described in Section 3.1.1.

IMaX is an imaging magnetograph capable of obtaining two-dimensional maps of Stokes profiles from which we can derived physical parameters such as the vector magnetic field and the LOS velocity in a given region of the solar surface. Figure 2.1 shows the optical design of IMaX, which is made up of two main optical parts: the spectrum analyzer, and the polarimeter. The former uses a Fabry–Pérot interferometer based on a $\mathrm{LiNbO_3}$ etalon. The etalon is a double pass, narrow-band tunable filter which achieves a spectral resolution of 8.5 pm. The polarimeter uses two liquid crystal variable retarders (LCVRs) as the polarization modulator and a beamsplitter as the polarization analyzer. This optical configuration and the highly Zeeman-sensitive line of Fe I at 525.02 nm used by IMaX allows us to observe the four Stokes parameters at various wavelength points inside the spectral line. The spectral line is sampled in various ways depending on the applied observing mode (see Section 3.1.1). In what follows we introduce the polarization and spectrum analyzers.

2.2.1 Polarimetric analysis

With two conceptually identical LCVRs and a beamsplitter, IMaX is able to produce the modulation schemes needed for measuring the full Stokes vector. As shown in Figure 2.1, the light beam passes through the retarders first and across the beamsplitter later. The LCVRs have their fast axis at 0° and 45°, and they introduce retardances of σ and ρ respectively. The optical axis of the beam splitter is aligned with the vertical direction, and consequently it forms an angle of 0° and 90° for each orthogonal polarization state. Proceeding as in the previous Section, the two perpendicular measured intensities can be represented

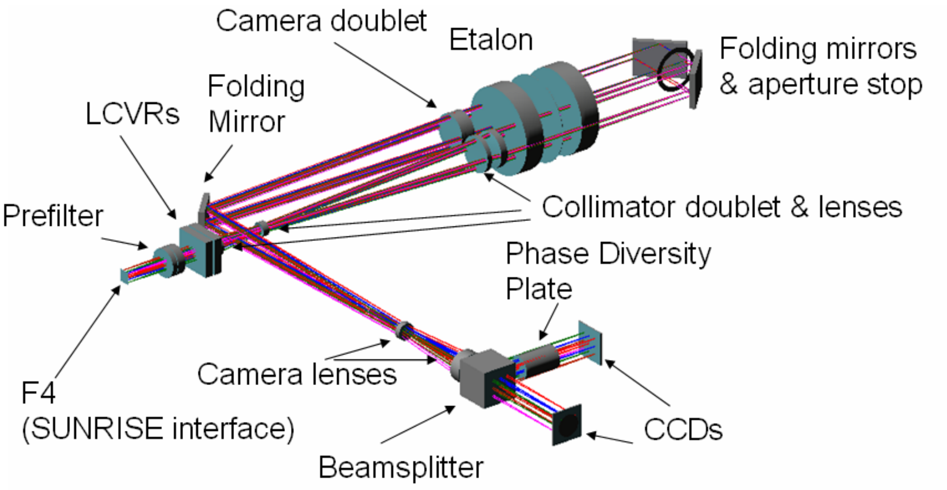

Figure 2.1: IMaX optical design (self-explained). From Martínez Pillet et al. (2011a).

as the following linear combination of the Stokes parameters:

$$\begin{aligned} I_{\mathrm{meas},1} &= \frac{1}{2}(I + Q\cos\rho + U\sin\rho\sin\sigma - V\sin\rho\cos\sigma), \\ I_{\mathrm{meas},2} &= \frac{1}{2}(I - Q\cos\rho - U\sin\rho\sin\sigma + V\sin\rho\cos\sigma). \end{aligned} \tag{2.11}$$

The LCVRs use voltages in the range of 0–10 V to obtain retardances between 535° and 20° (Martínez Pillet et al. 2011a). The four Stokes parameters are measured by applying four different combinations of voltages to the LCVRs. In order to maximize the so-called polarimetric efficiency (see Del Toro Iniesta & Collados 2000) and minimize the switching times of the LCVRs, Martínez Pillet et al. (2004) propose the following retardance values:

$$\begin{aligned} (\sigma_1, \sigma_2, \sigma_3, \sigma_4) &= (315, 315, 225, 225), \\ (\rho_1, \rho_2, \rho_3, \rho_4) &= (305.264, 54.736, 125.264, 234.736), \end{aligned} \tag{2.12}$$

for the first and second retarders, respectively. As demonstrated by Martínez Pillet (2007) and Del Toro Iniesta & Martínez Pillet (2012), such a combination of retardances enables to reach the theoretically optimum efficiencies. This modulation scheme leads to four independent intensity measurements:

$$\begin{aligned} I_1 &= I + \frac{1}{\sqrt{3}}Q + \frac{1}{\sqrt{3}}U + \frac{1}{\sqrt{3}}V, & I_2 &= I + \frac{1}{\sqrt{3}}Q - \frac{1}{\sqrt{3}}U - \frac{1}{\sqrt{3}}V, \\ I_3 &= I - \frac{1}{\sqrt{3}}Q - \frac{1}{\sqrt{3}}U + \frac{1}{\sqrt{3}}V, & I_4 &= I - \frac{1}{\sqrt{3}}Q + \frac{1}{\sqrt{3}}U - \frac{1}{\sqrt{3}}V, \end{aligned} \tag{2.13}$$

which in turn provide all four Stokes parameters as

$$\begin{aligned} I &= \frac{1}{4}I_1 + \frac{1}{4}I_2 + \frac{1}{4}I_3 + \frac{1}{4}I_4, & Q &= \frac{\sqrt{3}}{4}I_1 + \frac{\sqrt{3}}{4}I_2 - \frac{\sqrt{3}}{4}I_3 - \frac{\sqrt{3}}{4}I_4, \\ U &= \frac{\sqrt{3}}{4}I_1 - \frac{\sqrt{3}}{4}I_2 - \frac{\sqrt{3}}{4}I_3 + \frac{\sqrt{3}}{4}I_4, & V &= \frac{\sqrt{3}}{4}I_1 - \frac{\sqrt{3}}{4}I_2 + \frac{\sqrt{3}}{4}I_3 - \frac{\sqrt{3}}{4}I_4. \end{aligned} \tag{2.14}$$

According to Eq. (2.11), two independent determinations of $\mathbf{I}$ are obtained by each camera, the combination of which improves significantly the final signal to noise (S/N) ratio of the observations.

2.2.2 Spectral analysis

The spectral sampling of the Fe I line at 525.02 nm is performed through a Fabry–Pérot interferometer, which is made of a solid $\mathrm{LiNbO_3}$ etalon. As the beam passes through the etalon, it is multiply reflected to produce a multiple-beam interference and maximize the transmission at some wavelengths. Changing the refractive index within by applying an external electric field, the wavelength at which the transmission is highest is modified. Through this process, the line can be scanned in a straightforward way. Telecentric and collimated mountings are two of the most common optical setups adopted for Fabry–Pérot interferometers. IMaX uses a collimated configuration, which results in a better spectral resolution and image quality than that for the telecentric one (Kentischer et al. 1998). Unfortunately, with this setup, the maximum transmissions are dependent on the incident angle of the ray, and a blueshift over the field of view (FOV) is produced. This issue requires special care with the maximum angle of incidence. The focal length of the collimator guarantees that the angle of incidence on the etalon does not exceed 0.44°, which produces a wavelength drift of 2.8 pm (over the largest circular FOV).

Solid $\mathrm{LiNbO_3}$ etalons have many advantages for their implementation in balloon platforms, such as their low weight and volume. In contrast, their tuning speed is their largest disadvantage. The etalon spends 80 ms tuning the typical step of about 4 pm used by IMaX (Martínez Pillet et al. 2011a). Since measurements should be carried out in a time shorter than the characteristic variation of solar structures, this limits the number of wavelength samples that are measured.

Finally, an important issue is to reduce the amplitude of the secondary transmission peaks. To this end, the system is also equipped with an interference pre-filter (with a band-pass of 0.1 nm) which strongly reduces their amplitude. The spectral resolution achieved by the instrument is 9.3 pm in a single pass. As the beam goes through the etalon twice the spectral resolution is improved by a factor $\sqrt{2}$ over the single pass case. However, due to the stray light coming from the side lobes, the final effective spectral resolution is degraded to 8.5 pm.

2.3 The radiative transfer equation in a magnetized atmosphere

Now that we are familiar with the propagation of light through different homogeneous optical devices, we can now go a step further and study the propagation of light in an inhomogeneous medium such as the solar photosphere. In particular on that atmosphere permeated by a magnetic field, which makes the medium anisotropic as it breaks the symmetry by introducing a preferential direction. The transport of light through such a medium is governed by the radiative transfer equation (RTE) for polarized light. Following, for instance, the notation in Del Toro Iniesta (2003), the transport of radiative energy through magnetized and plane-parallel anisotropic atmospheres is described by:

$$\frac{d\mathbf{I}}{d\tau_{\mathrm{c}}} = \mathbf{K}(\mathbf{I}-\mathbf{S}) \tag{2.15}$$

where τ_{c} is the continuum optical depth, $\mathbf{S}$ is the source function vector, and $\mathbf{K}$ is the propagation matrix. Under the local thermodynamic equilibrium (LTE) assumption, $\mathbf{S} = (B_\nu, 0, 0, 0)^T$, where $B_\nu(T)$ is the Planck function at the local temperature, T. All the information about the polarization state of the light is contained in the Stokes vector, $\mathbf{I} = (I, Q, U, V)^T$, while $\mathbf{K}$ and $\mathbf{S}$ include all the medium properties and geometry relevant for the formation of the Stokes spectrum. The propagation matrix $\mathbf{K}$ can be written as:

$$\mathbf{K} = \begin{pmatrix} \eta_I & \eta_Q & \eta_U & \eta_V \\ \eta_Q & \eta_I & \rho_V & -\rho_U \\ \eta_U & -\rho_V & \eta_I & \rho_Q \\ \eta_V & \rho_U & -\rho_Q & \eta_I \end{pmatrix}, \tag{2.16}$$

where

$$
\begin{aligned}
\eta_I &= 1+\frac{\eta_0}{2}[\phi_{\rm p}\sin^2\gamma+\frac{\phi_{\rm b}+\phi_{\rm r}}{2}(1+\cos^2\gamma)],\\
\eta_Q &= \frac{\eta_0}{2}[\phi_{\rm p}-\frac{\phi_{\rm b}+\phi_{\rm r}}{2}]\sin^2\gamma\cos 2\varphi,\\
\eta_U &= \frac{\eta_0}{2}[\phi_{\rm p}-\frac{\phi_{\rm b}+\phi_{\rm r}}{2}]\sin^2\gamma\sin 2\varphi,\\
\eta_V &= \frac{\eta_0}{2}[\phi_{\rm r}-\phi_{\rm b}]\cos\gamma,\\
\rho_Q &= \frac{\eta_0}{2}[\psi_{\rm p}-\frac{\psi_{\rm b}+\psi_{\rm r}}{2}]\sin^2\gamma\cos 2\varphi,\\
\rho_U &= \frac{\eta_0}{2}[\psi_{\rm p}-\frac{\psi_{\rm b}+\psi_{\rm r}}{2}]\sin^2\gamma\sin 2\varphi,\\
\rho_V &= \frac{\eta_0}{2}[\psi_{\rm r}-\psi_{\rm b}]\cos\gamma.
\end{aligned}
\tag{2.17}
$$

γ and φ represent the inclination angle (with respect to the propagation direction) and the azimuth angle (with respect to the Stokes Q positive direction) of the vector magnetic field, respectively. η_0 stands for the ratio between the line and continuum absorption coefficients, and it depends on two thermodynamic variables: temperature, T, and density, ρ, or the electron pressure, $p_{\rm e}$, through the Boltzmann and Saha equilibrium population equations. $\phi_{\rm p,b,r}$ and $\psi_{\rm p,b,r}$ are the absorption and dispersion profiles, where p,b,r indices stand for the π, $\sigma_{\rm b}$ and $\sigma_{\rm r}$ components of the "normal" Zeeman triplet. In the most general case, when we account for the "anomalous" Zeeman effect, the absorption and dispersion profiles can be cast as a sum of as many Zeeman components as those allowed by quantum mechanics:

$$
\begin{aligned}
\phi_\alpha &= \frac{1}{\sqrt{\pi}}\sum_i S_{\alpha,i}\,H(u,a),\\
\psi_\alpha &= \frac{1}{\sqrt{\pi}}\sum_i S_{\alpha,i}\,F(u,a).
\end{aligned}
\tag{2.18}
$$

$S_{\alpha,i}$ stand for the strength of each Zeeman component and are proportional to the transition probability, with $\alpha=+1,0,-1$, or b,p,r, referring to three different polarization states, namely, linearly polarized light along the vector magnetic field and circularly polarized light (left- and right-handed) in the plane perpendicular to the vector magnetic field. $H(u,a)$ and $F(u,a)$ are the Voigt and Faraday-Voigt functions:

$$
\begin{aligned}
H(u,a) &= \frac{a}{\pi}\int_{-\infty}^{\infty} e^{-y^2}\frac{1}{(u-y)^2+a^2}dy,\\
F(u,a) &= \frac{1}{\pi}\int_{-\infty}^{\infty} e^{-y^2}\frac{u-y}{(u-y)^2+a^2}dy,
\end{aligned}
\tag{2.19}
$$

where $u = u_0 - u_{\text{LOS}} + u_{B,\alpha,i}$. These three variables are dimensionless and they are defined as:

$$u_0 = \frac{\lambda - \lambda_0}{\Delta\lambda_{\text{D}}}, \qquad u_{\text{LOS}} = \frac{\lambda_0 v_{\text{LOS}}}{c\Delta\lambda_{\text{D}}}, \qquad u_{B,\alpha,i} = -\frac{\Delta\lambda_{B,\alpha,i}}{\Delta\lambda_{\text{D}}}. \tag{2.20}$$

λ_0 is the central wavelength of the spectral line, c is the speed of light and v_{LOS} the plasma bulk velocity along the LOS. $\Delta\lambda_{\text{D}}$ is the Doppler width, which accounts for the broadening of the spectral line due to the Doppler effect produced by the thermal motions of atoms and ions. It is related to the temperature, T, of the medium by

$$\Delta\lambda_{\text{D}} = \frac{\lambda_0}{c}\sqrt{\frac{2kT}{m} + v_{\text{mic}}^2}, \tag{2.21}$$

where k is the Boltzmann constant and m the rest mas of the atom. v_{mic} is the so-called microturbulence velocity, which is an *ad hoc* parameter introduced for accounting for those motions on smaller scales than the mean free path of photons. Last but not least, $\Delta\lambda_{B,\alpha,i}$ is the wavelength shift of the different Zeeman components due to the Zeeman splitting, and it is related to the magnetic field strength, B, by

$$\Delta\lambda_{B,\alpha,i} = \frac{e\lambda_0^2 B}{4\pi mc^2}(M_{l,i}(g_l - g_u) - \alpha g_u), \tag{2.22}$$

where e and m stand for the charge and mass of the electron; l and u are the lower and upper levels of the transition, M is the magnetic quantum number, and g is the *Landé* factor of each Zeeman sublevel involved in the transition.

At this point, it is worth noting that the physical quantities of the medium such as the temperature, T, the LOS velocity, v_{LOS}, and the vector magnetic field (B, γ and φ) among others are included in the propagation matrix and in the source function. Knowing the atmospheric parameters from where a given solar spectral line is formed, we could in principle solve the RTE and obtain the Stokes parameters of the outcoming light beam. However, what we measure with spectropolarimeters like IMaX is nothing but the Stokes parameters of the polarized light. Therefore, what we have to solve is the inverse problem. The medium properties are obtained form the measured Stokes spectrum. This is a formidable problem, but fortunately resolvable, as we shall see in Section 3.2.

3

INSTRUMENTATION, DATA, AND ANALYSIS

The study of the quiet-Sun magnetism demands high spatial and temporal resolution, along with high polarimetric sensitivity and accuracy. Magnetic fields in the solar photosphere are seen as structures up to the smallest observable scales, and their evolution is found to be highly dynamic (e.g., Bellot Rubio & Orozco Suárez 2015). We use observations from the SUNRISE balloon-borne solar observatory which allows to resolve magnetic structures with sizes of about 100 km, up to the diffraction limit of the 1-m telescope. Being a stratospheric mission, it gets rid of most of the turbulent Earth's atmosphere, which provides nearly seeing-free imaging conditions.

In this Chapter, we describe the SUNRISE mission and its two main post-focus instruments, the data that we use for this thesis, and the method applied for inferring the physical quantities at the solar surface.

3.1 SUNRISE stratospheric balloon-borne solar observatory

The SUNRISE stratospheric balloon-borne solar observatory (Solanki et al. 2010; Barthol et al. 2011) consists of a 1-m Gregory-type reflector telescope with two post-focus science instruments: the Imaging Magnetograph eXperiment (IMaX; Martínez Pillet et al. 2011a), a spectropolarimeter, and the SUNRISE Filter Imager (SuFI; Gandorfer et al. 2011), a multi-channel UV filter imager. During the whole observation time the science images of both instruments are coaligned and corrected for residual motions of the system by the Correlating Wavefront Sensor (CWS; Berkefeld et al. 2011) and stabilized by the Image Stabilization Light Distribution (ISLiD; Gandorfer et al. 2011) unit. The latter also allows simultaneous

Figure 3.1: SUNRISE before launch in ESRANGE on 2009 June 8. From Barthol et al. (2011).

observations by distributing the radiation according to the wavelength of each instrument (525.05 nm IMaX; 200–400 nm SuFI).

SUNRISE flew on a zero-pressure helium balloon in the framework of NASA's Long Duration Balloon program. The first science flight was successfully launched on 2009 June 8 from ESRANGE near Kiruna (northern Sweden). Figure 3.1 shows an image of the gondola payload and the partly filled balloon just before launch. It then traveled westward for almost six days over the Arctic Circle at a mean cruise altitude of 36 km, and landed on Somerset island (northern Canada) on 2009, June 13. Figure 3.2 shows the trajectory of the first SUNRISE flight. The Sun was extremely quiet at that time, and essentially all of the data correspond to internetwork regions with a few network elements.

3.1.1 IMaX: the Imaging Magnetograph eXperiment

The Imaging Magnetograph eXperiment, IMaX, is an imaging spectropolarimeter with full Stokes vector capabilities at the Zeeman-sensitive Fe I line at 525.02 nm (Landé factor g = 3; Martínez Pillet et al. 2011a). It contains two main optical parts: a spectrograph, and a polarimeter. The spectrograph consists of a double pass LiNbO$_3$ etalon and narrow band pre-filter (with a FWHM of 0.1 nm) to achieve a spectral resolution of 8.5 pm. The polarimeter

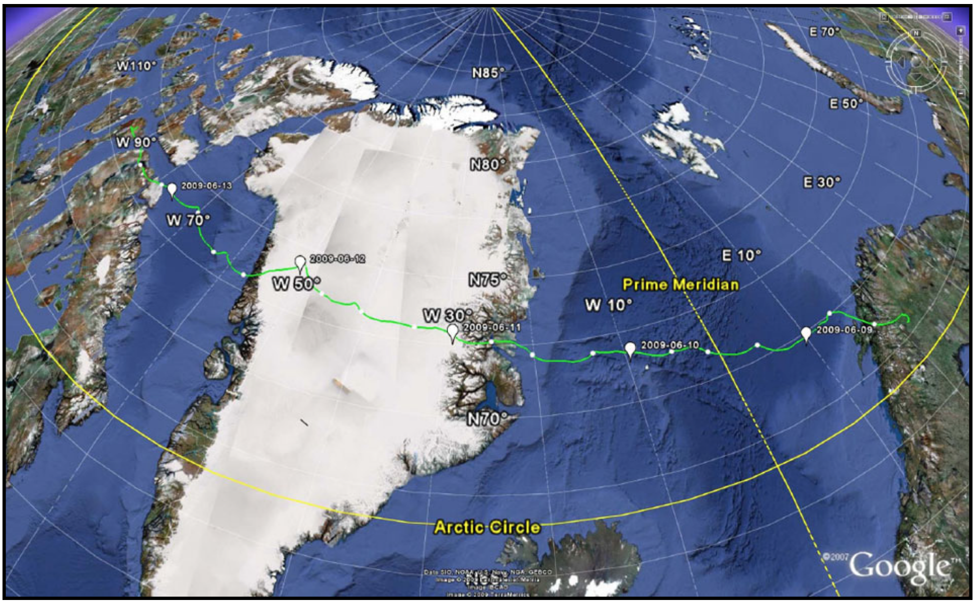

Figure 3.2: SUNRISE flight trajectory from Kiruna in northern Sweden to Somerset island (northern Canada). From Barthol et al. (2011).

performs fast polarization modulation, based on two liquid crystal variable retarders, and dual-beam polarization analysis that, together with the spectrograph, allows to obtain the four Stokes parameters in various wavelength positions. Such measurements were discussed with some detail in Section 3.2.

During the flight different observing modes were used according to the acquired number of wavelengths (N_λ), accumulations (N_A), and polarization states. Three spectral observing modes with, 2, 4 and 11 points inside the spectral line plus one at the nearby continuum were used. An observing mode is called vectorial (labeled V) if all the four Stokes parameters are measured, while a longitudinal mode (labeled L) only cares about circular polarization, namely, only Stokes I and V are measured. Table 3.1 lists all the IMaX observing modes used during the first SUNRISE flight. Labels at the left column represent the polarization states (V and L) followed by wavelengths number (N_λ) and accumulation number (N_A).

The light beam is divided into two orthogonal polarization states by the beamsplitter. The images are recorded in two synchronized 1024×1024 pixels CCD cameras, with a spatial sampling of 0.055 arcsec per pixel. After every observing run, a thick glass plate is inserted into the light path in front of one of the cameras to acquire a set of 30 in-focus and out-of-focus image pairs for post-facto phase diversity (PD) reconstruction (Gonsalves 1982; Paxman et al. 1996). Before data reduction, several procedures were used for dark-

Table 3.1: IMaX observing modes during the first SUNRISE flight.

Observing mode	Cadence (s)	Line samples (pm)	Continuum (pm)
V5-6	33	-8, -4, +4, +8	+22.7
V5-3	18	-8, -4, +4, +8	+22.7
V3-6	20	-6, +6	+22.7
L3-2	8	-6, +6	+22.7
L12-2	31	-19.25 to +19.25 each 3.5	+19.25

current subtraction, flat-field correction, and polarization cross-talk removal. Through the PD inversion technique, the point-spread function (PSF) is retrieved and the science images are reconstructed by deconvolving this PSF from the originally recorded images. The process requires an apodization that effectively reduces the IMaX field of view (FOV) down to about $43'' \times 43''$. The spatial resolution has been estimated to be $0\farcs15$–$0\farcs18$ after reconstruction. The noise level in each Stokes parameter is about 3×10^{-3} in units of the continuum intensity, and the rms contrast of the quiet-Sun granulation obtained from continuum data is about 13.5 % (Solanki et al. 2010), which testifies to the outstanding quality of IMaX images. For more information on IMaX we refer the reader to the paper by Martínez Pillet et al. (2011a).

3.1.2 SuFI: the SUNRISE Filter Imager

The SUNRISE Filter Imager, SuFI, provides images at violet and near ultraviolet wavelengths. It consists of a filter wheel with five filters and a mechanical shutter for exposure control (Gandorfer et al. 2011). The wavelengths sampled are: 214 nm (FWHM ∼ 10 nm), 300 nm (FWHM ∼ 5 nm), 312 nm (FWHM ∼ 1.2 nm), CN-band head at 388 nm (FWHM ∼ 0.8 nm), and core of Ca II H at 396.8 nm (FWHM ∼ 0.18 nm). However, only the CN-band and Ca II H images are used in this thesis.

A 2048 × 2048 pixels UV-enhanced CCD, with a spatial sampling of 0.0207 arcsec pixel^{-1} is employed. Focused images are acquired on one half of the detector, while the other half receives an image with a defocus of one wave at 214 nm, which results in a FOV of $13'' \times 38''$. This strategy is used for post-facto PD reconstruction (Hirzberger et al. 2011).

The time cadence varies depending on the light level entering SuFI and the number of filters used. The light level decreases towards shorter wavelengths, and hence the exposure time varies from 1 s (at 396.8 nm) to 30 s (at 214 nm). The typical time cadence ranged between 2–12 s whenever the 214 nm filter was not included. A detailed description of SuFI is given by Gandorfer et al. (2011).

3.2 Diagnostics of physical quantities

We have already seen that IMaX was designed for measuring the Stokes profiles that emerge from the solar atmosphere. The formation of these profiles are well described by the RTE for polarized light (see Section 2.3). This equation shows that the Stokes spectrum depends on the physical properties of the medium. In particular, the atmosphere is specified by a number of physical parameters and their stratification at different optical depths. Typically, the temperature, T, the electron pressure, $p_{\rm e}$, the microturbulence velocity, $v_{\rm mic}$, the LOS velocity, $v_{\rm LOS}$, the magnetic field strength, B, inclination, γ, and azimuth, φ, are included. This set of parameters forms the so-called *model atmosphere*, which can be represented by a vector,

$$\mathbf{x}(\tau_{\rm c}) = [T(\tau_{\rm c}), p_{\rm e}(\tau_{\rm c}), v_{\rm mic}(\tau_{\rm c}), v_{\rm LOS}(\tau_{\rm c}), B(\tau_{\rm c}), \gamma(\tau_{\rm c}), \varphi(\tau_{\rm c}), v_{\rm mac}(\tau_c)], \tag{3.1}$$

where $v_{\rm mac}$ is the macroturbulence velocity, an ad-hoc parameter that accounts for turbulent motions that are not resolved by the spatial resolution element.

For a given model atmosphere, we can solve the RTE and obtain the synthetic Stokes profiles. This is not, however, a straightforward task and we are not going to enter into the details here. For the description of various numerical solutions, we refer the reader to Landi Degl'Innocenti (1987), Rees et al. (1989), Bellot Rubio et al. (1998), and Semel & López Ariste (1999).

3.2.1 The inversion problem

The fundamental problem in solar physics is the inference of the physical quantities that describe the different processes taking place in the solar atmosphere. Unfortunately we do not have the ability to directly measure the magnetic, dynamic, and thermal properties of the solar features. Rather, what we measure is nothing but the (polarized) light that escapes from the Sun. Therefore, we have to content with indirect inferences of the physical parameters retrieved through the Stokes profiles. The simplest approach is that of a direct comparison between synthetic and observed profiles, where the model atmosphere is modified randomly until a good match is obtained. This is however inefficient when the number of free parameters increases or a large amount of data is used. Hence, automatic procedures are highly desirable. The inversion codes deal with this problem through automatic minimization of the mean quadratic distance between the synthetic and the observed Stokes spectrum given by a merit function such as

$$\chi^2(\mathbf{x}) = \frac{1}{\nu}\sum_{s=1}^{4}\sum_{i=1}^{N_\lambda}\frac{[I_s^{\mathrm{obs}}(\lambda_i) - I_s^{\mathrm{syn}}(\mathbf{x},\lambda_i)]^2}{\sigma_{s,i}^2}w_s^2, \tag{3.2}$$

where ν represents the number of degrees of freedom, namely, the difference between the number of observables ($4N_\lambda$) and the free parameters (the number of elements in $\mathbf{x}$, n). Indices s and i scan the four Stokes parameters and the wavelength samples, respectively. The measured uncertainties are given by $\sigma_{s,i}$ and w_s are arbitrary weights for the different Stokes profiles. $I_s^{\mathrm{obs}}(\lambda_i)$ and $I_s^{\mathrm{syn}}(\mathbf{x},\lambda_i)$ are the observed and synthetic Stokes profiles, respectively.

In order to obtain a physically meaningful model atmosphere, $\mathbf{x}$, an absolute minimum of the merit function has to be found. This is not trivial as the merit function is a non-linear function in an n-dimensional space. In addition, it may have several local minima, which further increase the problem. In the next Section we briefly introduce one of the most successful inversion codes that has been applied to photospheric Stokes profiles.

3.2.2 SIR: Stokes Inversions based on Response functions

The Fe I spectral line at 525.02 nm that IMaX observes is formed in the solar photosphere. In this layer the density is high enough that LTE approximation turns out to be a satisfactory approach. The LTE hypothesis assumes that the collision rates between material particles are frequent enough that the energy level populations of atoms depend only on local values of temperature and density. Hence, the local number of absorbers and emitters in the various quantum states are given by the Boltzmann and Saha population equations.

The SIR inversion code (Ruiz Cobo & Del Toro Iniesta 1992) solves the RTE to compute the synthetic Stokes profiles under the assumption of LTE and for plane-parallel atmospheres. The code uses the Levenberg-Marquardt algorithm to modify the initial model and find the absolute minimum of the merit function. The method is actually a combination of the gradient descent method and the Gauss-Newton method. When the parameters are far from their optimal value the algorithm acts more like the gradient-descent method, which takes large steps down the gradient but it is inaccurate in the final convergence. When the solution is close to the minimum then the Gauss-Newton method is used, which takes small steps down to the minimum.

SIR deals with the full stratification of the model parameters. The number of free parameters is reduced by evaluating perturbations to the different model quantities at a few depth grid points called *nodes*. The nodes are used for perturbing the whole atmosphere through a polynomial spline interpolation. For example, when a single node is used, the whole atmosphere is modified by a constant; if two nodes are selected, the atmosphere is

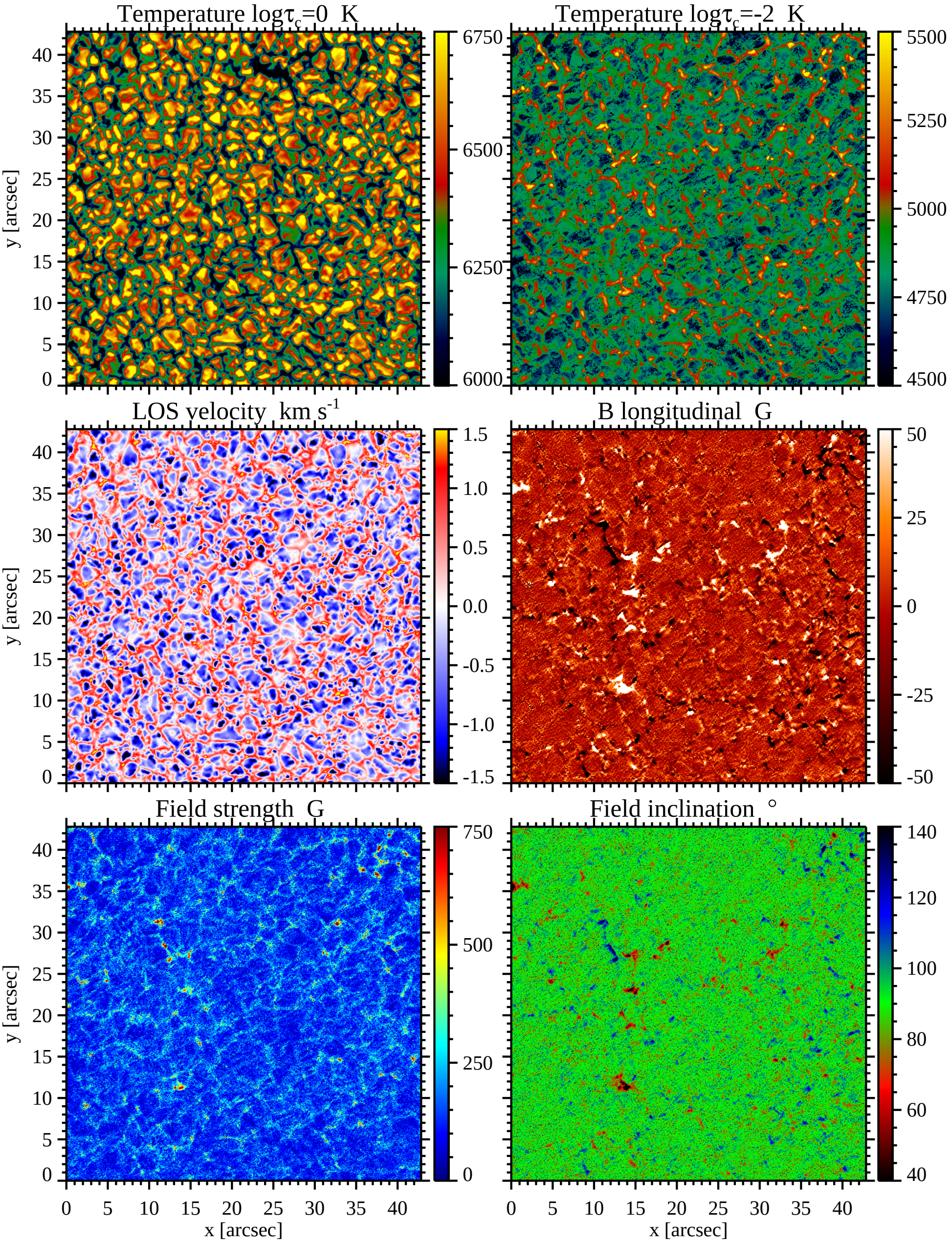

Figure 3.3: Results of the SIR inversions for the data taken by SUNRISE/IMaX on 2009 June 9 at 00:37:09 UT. See text for details.

perturbed by a straight line passing trough the nodes; the perturbation is parabolic when the number of nodes is equal to three, and so on. *Equivalent* response functions are calculated to include the sensitivity of all depth grid points (see Ruiz Cobo & Del Toro Iniesta 1994). The equivalent response functions are linear combinations of the response functions at all the grid points so that the information from the whole atmosphere is used. For further reading on the SIR code, we refer the reader to Ruiz Cobo & Del Toro Iniesta (1992), Del Toro Iniesta & Ruiz Cobo (1996) or Del Toro Iniesta (2003).

Inversion strategy

We initialize the code with the Harvard-Smithsonian Reference Atmosphere (Gingerich et al. 1971, with added magnetic and velocity parameter values). We perform a Milne-Eddington-like approach, which assumes that the magnetic field strength B, the inclination and the azimuth angles γ and φ, the LOS velocity $v_{\rm LOS}$, and the microturbulent velocity $v_{\rm mic}$ are constant with depth. Due to the high spatial resolution of the data, the magnetic filling factor, f (which specifies the fraction of the pixel filled with magnetic field), is assumed to be unity and the macroturbulent velocity $v_{\rm mac}$ is set to zero. From B and γ we also derive the longitudinal component of the magnetic field $B_{\rm long} = B\cos\gamma$ (longitudinal magnetogram). The temperature T, is modified with two nodes located at the first and last point of the stratification ($\log\tau_{\rm c} = 1.4$ and -4.0), where $\tau_{\rm c}$ is the continuum optical depth at 500 nm. We estimate the noise-induced uncertainty in the field strength and LOS velocity by repeating the inversions with 100 different realizations of added noise (with amplitudes of $3\times10^{-3}I_{\rm c}$) to the observed Stokes profiles. The standard deviation of all these values is 150 G and 150 $\rm m\,s^{-1}$, respectively.

Figure 3.3 shows an example of the physical parameters resulting from the SIR inversions of the IMaX data. From top to bottom and left to right, we show the temperature at $\log\tau_{\rm c} = 0$ and $\log\tau_{\rm c} = -2$, the LOS velocity, the longitudinal component of the magnetic field, the field strength, and inclination. At $\log\tau_{\rm c} = 0$ the temperature resembles the solar granulation, where hot and cold areas correspond to granules and intergranules, respectively. Upper in the photosphere, at $\log\tau_{\rm c} = -2$, the granulation temperature is reversed, and the hottest regions outline a mesogranular size network. In the LOS velocity image downflows (redshifts) are shown in red and outflows (blueshifts) in blue. The longitudinal magnetogram makes it evident the mixed polarity nature of the quiet-Sun magnetic fields. The largest structures have stronger field strength and they are more vertical than the weakest ones.

4

THE HISTORY OF A QUIET-SUN MAGNETIC ELEMENT

Isolated flux tubes are considered to be fundamental magnetic building blocks of the solar photosphere. Their formation is usually attributed to the concentration of magnetic field to kG strengths by the convective collapse mechanism. However, the small size of the magnetic elements in quiet-Sun areas has prevented this scenario from being studied in fully resolved structures. Here we report on the formation and subsequent evolution of one such photospheric magnetic flux tube, observed in the quiet Sun with unprecedented spatial resolution ($0\farcs15$–$0\farcs18$) and high temporal cadence (33 s). The observations were acquired by the Imaging Magnetograph eXperiment aboard the SUNRISE balloon-borne solar observatory. The equipartition field strength magnetic element is the result of the merging of several same polarity magnetic flux patches, including a footpoint of a previously emerged loop. The magnetic structure is then further intensified to kG field strengths by convective collapse. The fine structure found within the flux concentration reveals that the scenario is more complex than can be described by a thin flux tube model with bright points and downflow plumes being established near the edges of the kG magnetic feature. We also observe a daisy-like alignment of surrounding granules and a long-lived inflow towards the magnetic feature. After a subsequent weakening process, the field is again intensified to kG strengths. The area of the magnetic feature is seen to change in anti-phase with the field strength, while the brightness of the bright points and the speed of the downflows vary in phase. We also find a relation between the brightness of the bright point and the presence of upflows within it.

4.1 Introduction

The interaction between convection, radiation, and magnetic field in the electrically conducting solar plasma leads to the creation of a rich variety of magnetic structures. Many of these have kG field strengths and range in size from the largest sunspots, tens of Mm in size, down to the smallest network and internetwork structures, i.e., "magnetic elements" on spatial scales of 100 km or less. The observations of decaying sunspots into smaller structures as well as the formation of pores from the accumulation of smaller magnetic features, has led to the notion that magnetic elements are fundamental entities of magnetic flux from which larger structures are assembled (see, e.g., Solanki 1993; de Wijn et al. 2009, for reviews).

The formation of magnetic elements is thought to be well understood from a theoretical point of view. It is generally accepted that the first step in producing such flux tubes is the *flux expulsion* mechanism. As suggested by Parker (1963) and Weiss (1964, 1966), the magnetic flux is advected by horizontal flows and concentrated in convective downflow areas, roughly up to the equipartition field strength (300–500 G), for which the magnetic energy density equals the kinetic energy density of the gas flow. These equipartition flux concentrations reduce the convective heat transfer, leading to super adiabatic cooling (Webb & Roberts 1978; Spruit & Zweibel 1979). This evacuates the flux tube, in such a way that the gas pressure of the surrounding plasma compresses the flux concentration until kG field strengths are reached (Parker 1978; Spruit 1979). This process is known as *convective collapse*, which is thought to be the fundamental step of flux-tube creation.

Later, numerical studies revealed further details of the final state of the magnetic feature. Hasan (1985) found that non-adiabatic effects arising from the radiative exchange between the flux tube and the external medium lead to overstable oscillations as the final state of a collapsed flux tube. On the other hand, Takeuchi (1999) reached a static solution, and showed that if the downflow in a collapsing flux tube becomes strong enough, an upward-traveling shock can develop as the downward flow bounces back in the dense deeper layers. This "rebound shock" reverses the magnetic flux intensification, and may lead to the dissolution of the magnetic flux concentration.

All these results are based on one-dimensional calculations, and rely on the thin flux-tube approximation. Grossmann-Doerth et al. (1998) made use of two-dimensional numerical simulations to study the interaction between the surrounding convective flow and the flux tube. They were the first to find the rebound shock solution for initial field strengths of 400 G. However, this result changes when the initial field is weaker, for which the flux sheet reaches a stable state rather than being dispersed. Steiner (1999) used similar numerical simulations and found a more "quiescent phase" during the time period between the formation of a magnetic flux tube and its dissolution or reformation. During this phase the magnetic field strength remains quite constant and the flux tube exhibits small internal gas motions. As a consequence of the interaction with the surrounding granular convection, the flux concentration moves laterally, bending and swaying, gets "squeezed", and during most of the time is bordered by strong, narrow downflows. These strong downflows get narrower with depth and accelerate strongly until they evolve into "jets" (Steiner et al. 1998). They are maintained by the cooling of the gas surrounding the flux concentration through radiative heat losses into the magnetic structure (Deinzer et al. 1984). More recently, Kato et al. (2011) carried out two-dimensional radiation MHD simulations, and showed that these downflow jets can indeed excite a downflow within the magnetic flux concentration, which rebounds and develops into an upward-travelling shock front. Through this mechanism, the atmosphere within the tube oscillates at the acoustic cutoff frequency. Furthermore, Jess et al. (2012) found that upwardly propagating acoustic waves are ubiquitous in quiet-Sun magnetic bright points and 3D MuRAM (Vögler et al. 2005) simulations.

From an observational point of view, spectropolarimetric evidence of convective collapse and subsequent destruction of magnetic flux by an upward-moving front in the quiet Sun was reported by Bellot Rubio et al. (2001). Magnetic flux intensification events have also been observed with the *Hinode* Spectro-Polarimeter. First, a single event by Nagata et al. (2008), where a strong downflow is detected while field strength intensifies and a bright point appears followed by a transient upflow, and then, a statistical analysis of 49 convective collapse events by Fischer et al. (2009).

The interaction between magnetic fields and convection is important to understand the formation and evolution of magnetic structures on the solar surface. Muller et al. (1989) observed that the presence of isolated Network Bright Points (NBPs) disturbs the surrounding granules which elongate in the direction of the magnetic features, forming a characteristic "daisy-like" structure. This granular pattern is formed as the small bright point appears while the surrounding granules converge (Muller & Roudier 1992). Bellot Rubio et al. (1997, 2000) found from the inversion of full Stokes profiles of the Fe I 630 nm lines that magnetic flux tubes in facular regions are surrounded by intense downdrafts, and suggested that these downdrafts produce downflows of lesser magnitude in the tube interior. Close to small magnetic flux concentrations, Rimmele (2004) observed strong, narrow ($<0''.2$) downflow plumes at the edge of many small flux tubes, while there was little gas motion inside the flux concentration, confirming earlier results showing almost unshifted Stokes V zero-crossing in network and plage regions (Solanki 1986; Martínez Pillet et al. 1997).

Isolated magnetic elements are the key to understanding a variety of solar structures, like plages, or the network. Unfortunately, these basic units are generally so small that they have mainly been studied using indirect techniques, either through the interpretation of Stokes spectra of the unresolved feature, or using their association to G-band bright points.

Recently, IMaX allowed photospheric quiet-Sun magnetic flux tubes to be spatially resolved even in the quiet Sun (Lagg et al. 2010; Martínez González et al. 2012b).

Here, we take advantage of these unprecedented high quality observations to report on the formation and evolution of a small kG flux concentration and its interaction with the surrounding granulation. The data suggest that the magnetic element is formed by advective coalescence of small-scale flux patches and a subsequent convective collapse phase. Once formed, the evolution of the mature flux tube is much more complicated than that explained by static flux-tube models. Many different phenomena are involved, namely: converging granules and granular fragments, downflow jets, bright points (BPs), oscillations in all basic physical quantities, small-scale upflow plumes, etc.

4.2 Observations and data analysis

We analyze disk center quiet-Sun IMaX spectropolarimetric observations. The data set was obtained on 2009 June 9, 00:36:03–00:58:46 UT. IMaX measured the full Stokes vector in five wavelength positions across the Fe I 525.02 nm line (Landé factor g = 3) at λ = -8, -4, +4, +8, and +22.7 pm from the line center (V5-6 mode). The temporal cadence of a full observing cycle is 33 s, with a pixel size of $0\farcs055$.

IMaX data reduction routines were used for dark-current subtraction, flat-field correction, and polarization crosstalk removal. The blueshift over the field of view (FOV) produced by the Fabry-Pérot interferometer is corrected in the inferred velocity values. The applied restoration technique requires an apodization that effectively reduces the IMaX FOV down to about $43'' \times 43''$. The spatial resolution has been estimated to be $0\farcs15$–$0\farcs18$ (after reconstruction), and the noise level in each Stokes parameter is about 2.5×10^{-3} in units of the continuum intensity. The rms contrast of the quiet-Sun granulation obtained from IMaX continuum data is around 13.5%, which testifies to the high quality of the SUNRISE/IMaX images. For further details about data reduction, we refer to Martínez Pillet et al. (2011a).

We obtained maps of the mean circular polarization averaged over the line, $V_{\rm s}$, and of the mean linear polarization signal, $L_{\rm s}$, given respectively by

$$
\begin{aligned}
V_{\rm s} &= \frac{1}{4\langle I_{\rm c}\rangle} \sum_{i=1}^{4} \varepsilon_i \cdot V_i, \\
L_{\rm s} &= \frac{1}{4\langle I_{\rm c}\rangle} \sum_{i=1}^{4} \sqrt{Q_i^2 + U_i^2},
\end{aligned}
\tag{4.1}
$$

where $\langle I_{\rm c}\rangle$ is the continuum intensity averaged over the IMaX FoV, $\varepsilon = [1, 1, -1, -1]$ and i runs over the first four wavelength positions within the spectral line. In the weak field regime, V_{s} very approximately scales with the longitudinal magnetic component, while L_{s} is a measure of the transverse (horizontal) component of the magnetic field.

We carried out inversions of the Stokes vector observed with IMaX using the SIR code (Ruiz Cobo & Del Toro Iniesta 1992). This code, based on the Levenberg-Marquardt algorithm, numerically solves the radiative transfer equation along the line of sight under the assumption of local thermodynamic equilibrium and minimizes the difference between the measured and the computed synthetic Stokes profiles using response functions.

Using two nodes at which the temperature is explicitely determined, the inversion yields the temperature stratification in the range $-4.0 < \log \tau_{\mathrm{c}} < 1.4$ through inter- and extrapolation, where τ_{c} is the continuum optical depth at 500 nm. However it is worth noting that with only 5 wavelength points and a single, very temperature dependent spectral line, the temperature is not constrained reliably in layers above $\log \tau_{\mathrm{c}} = -1.5$ or -2 (depending on the type of feature and the strength of the line). We also obtain the height-independent magnetic field strength B, the inclination and azimuth angles γ and φ, the LOS velocity, and the microturbulent velocity, using one node for each of them. The magnetic filling factor is assumed to be unity and the macroturbulent velocity is set to zero due to the high spatial resolution of the data.

Figure 4.1 displays a map of the mean circular polarization for the FoV covered by the observations, about $43'' \times 43''$over a quiet region at disk center. It shows many internetwork flux concentrations along with stronger and larger flux elements probably belonging to the network.

After applying a p-mode subsonic filter (Title et al. 1989) to the continuum intensity and LOS velocity maps, we focus on a smaller area of $12\overset{\prime\prime}{.}1 \times 12\overset{\prime\prime}{.}1$, indicated by the white dashed-line square in Figure 4.1. On this subfield, we aligned the continuum intensity maps by applying a cross-correlation technique on two consecutive images. The same displacement correction was also applied to the other parameters of interest. Finally, we restricted ourselves to study an even smaller area of $5\overset{\prime\prime}{.}5 \times 5\overset{\prime\prime}{.}5$, displayed by the white solid-line square in Figure 4.1. Within this area, we constructed movies of the continuum intensity, LOS velocity, circular polarization, and field strength, and we obtained horizontal velocity maps of the first three parameters time averaged over a given interval by using the local correlation tracking (LCT) technique (November 1986) as implemented by Molowny-Horas & Yi (1994). This technique selects small sub-fields around the same pixel in contiguous frames, and correlates them to find the best-match displacement. The sub-fields are defined by a Gaussian tracking window with a full width at half maximum (FWHM) of $0\overset{\prime\prime}{.}3$. In order to help the algorithm, the original images are interpolated in time (linearly) and space (bi-linearly) so that the pixel size and cadence is reduced to $0\overset{\prime\prime}{.}028$ and 11 s respectively. These interpolations do not add any significant information and therefore do not change the

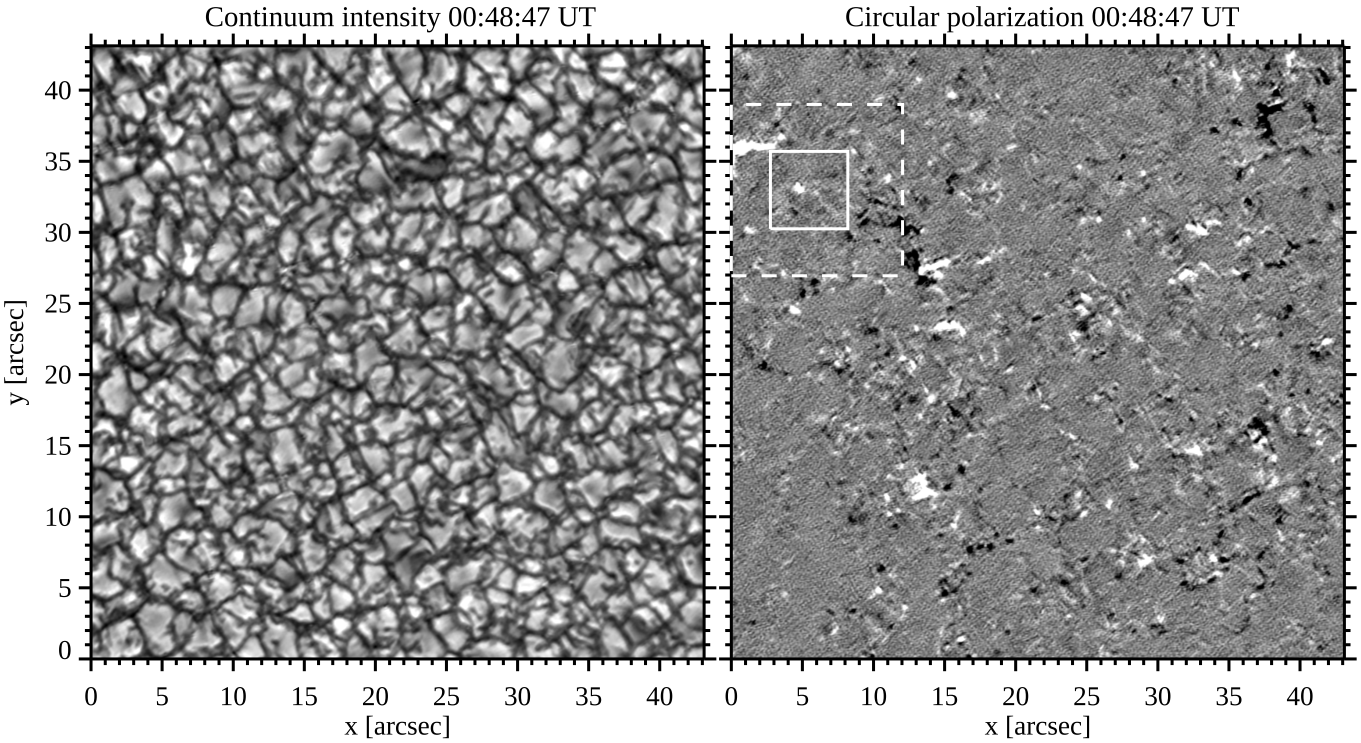

Figure 4.1: Left panel: Continuum intensity map, I_c. Right panel: Map of the mean circular polarization signal V_s with a scale range of [-1,1]% of the I_c, covering the FOV of IMaX of about $43'' \times 43''$. The dashed-line square, with a FOV of $12\overset{\prime\prime}{.}1 \times 12\overset{\prime\prime}{.}1$, indicates the location whose continuum intensity has been aligned by cross-correlating two consecutive images. The inner solid line square, with a FOV of $5\overset{\prime\prime}{.}5 \times 5\overset{\prime\prime}{.}5$, indicates the subregion where the magnetic element is studied in detail, as shown in the sequences displayed in Figures 4.2, 4.4, and 4.6.

results. They only help to get less noisy velocity maps. An example of such horizontal velocity maps is shown in Figure 4.3 which is discussed later in Section 4.3.

4.3 Flux concentration

Figure 4.2 displays a temporal sequence of the continuum intensity I_c normalized to the average value over the IMaX FoV, the LOS velocity retrieved with SIR, and the circular polarization V_s maps. Note that not all frames in the figure are consecutive. The sequence describes the first phase in the magnetic structure evolution, mostly characterized by the rise of a small-scale magnetic flux loop and the granular dragging of its footpoints to nearby intergranular lanes. The high and constant spatial resolution of the data allows us to trace the dynamics of sub-arcsecond magnetic patches. We use this property to track the advection of polarization signal by the horizontal plasma flows. Red and blue contours encircle areas with positive and negative circular polarization respectively, whereas green contours indicate regions with a significant linear polarization signal.

In frame 1, at coordinates $[0\farcs75, 1\farcs25]$ there is a small-scale loop (Martínez González et al. 2007; Martínez González & Bellot Rubio 2009; Danilovic et al. 2010b) with a bipole flux of 4×10^{16} Mx and a field strength peak of 300 G above a pre-existing granule.[1] Two opposite-polarity footpoints are connected by a quite strong L_s signal between them. A statistical study of granular scale loops has already been carried out by Martínez González et al. (2012a), using these IMaX data. From the same SUNRISE science flight, Guglielmino et al. (2012) reported on the evolution of a larger, intermediate-scale, magnetic bipole.

Here, the evolution of the loop can easily be followed in the subsequent V_s frames. The footpoints move from within the granule to nearby intergranular lanes. This motion represents a phase of flux expulsion. At the same time, the Ω-shaped loop is rising as witnessed by the progressive disappearance of the L_s signal (the loop top) while the footpoints stay in the photosphere. Therefore, the underlying granule not only helps to bring the loop to higher layers but also advects the footpoints to the intergranular lanes. At frame 6, the negative footpoint disappears, which is more likely due to cancellation with an opposite polarity patch appearing from frame 2 to 5 at coordinates $[0\farcs75, 1\farcs5]$, just above the negative footpoint. Note that the weakening of the L_s signal occurs when flux is cancelling, hence suggesting that cancellation also contributes to the disappearance of L_s. This cancellation of opposite-polarity magnetic patches should be related with some form of magnetic reconnection, in a similar way as the strong blueshift events first observed by Borrero et al. (2010)

---

[1] Unless otherwise stated, fluxes are calculated throughout the Chapter by considering the area enclosed by contours of $V_\mathrm{s} = 8 \times 10^{-3}$. Field strength values are calculated as averages over 3×3 pixel boxes to reduce the influence of noise.

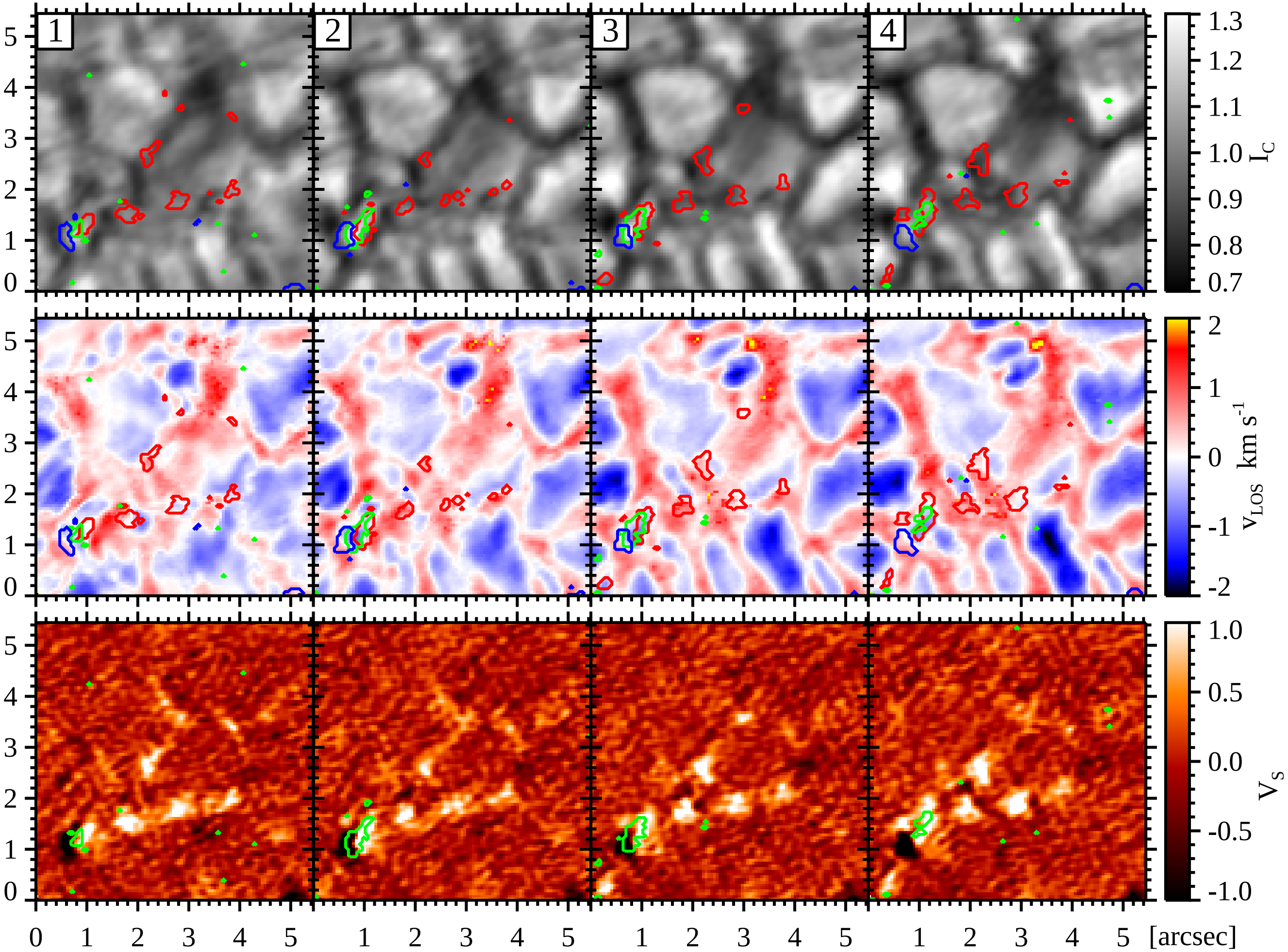
1
2
3
4
0
1
2
3
4
5
[arcsec]
1.3
1.2
1.1
1.0
0.9
0.8
0.7
I_C
2
1
0
-1
-2
v_{LOS} km s^{-1}
1.0
0.5
0.0
-0.5
-1.0
V_S

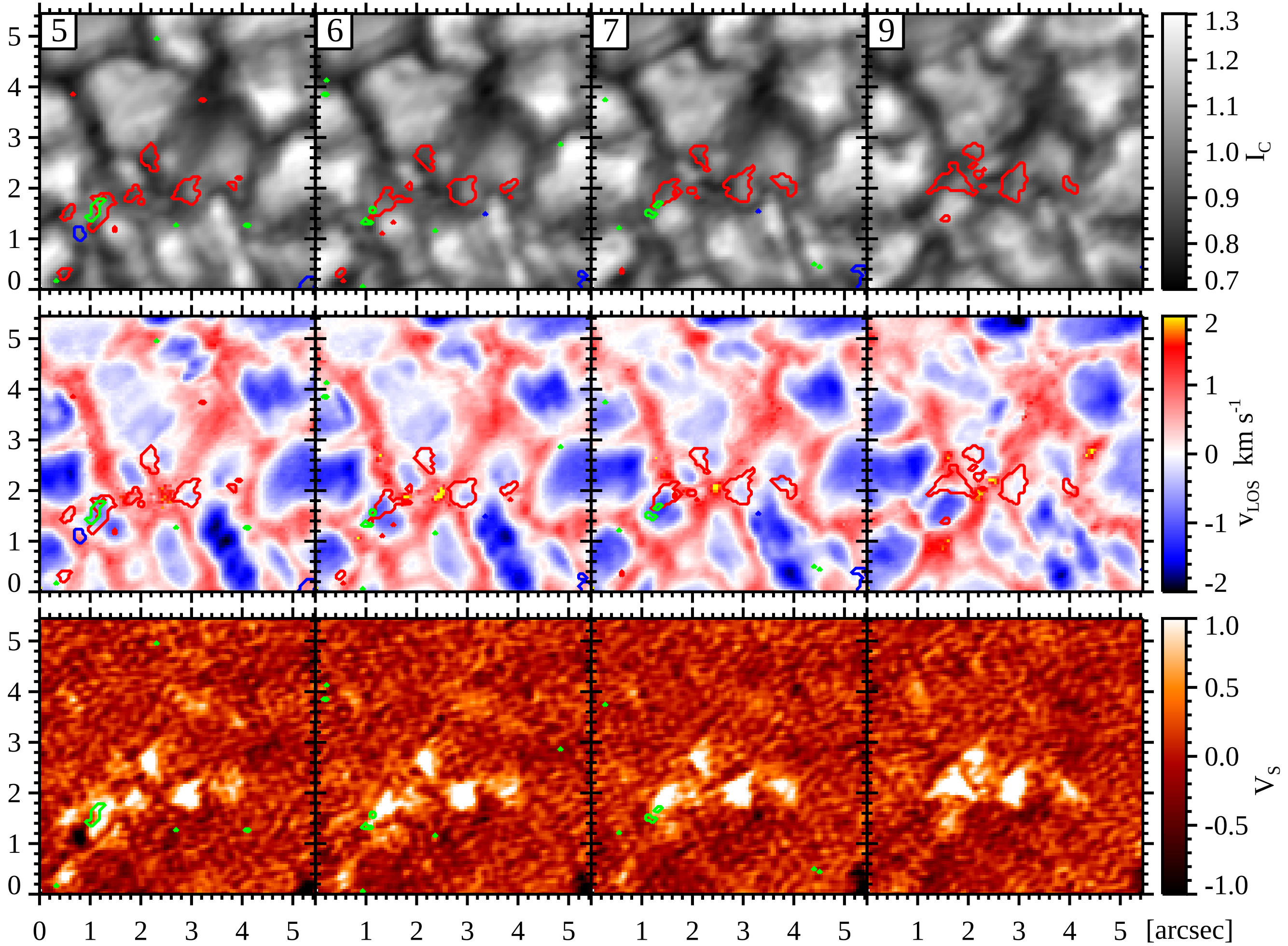
5
6
7
9
0
1
2
3
4
5
[arcsec]
1.3
1.2
1.1
1.0
0.9
0.8
0.7
I_C
2
1
0
-1
-2
v_{LOS} km s^{-1}
1.0
0.5
0.0
-0.5
-1.0
V_S

Figure 4.2: (Previous page.) Temporal sequence of the continuum intensity maps (top rows), LOS velocity (middle rows), and total circular polarization $V_{\rm s}$ (bottom rows) during the flux concentration phase. Red (blue) contours over the maps represent a circular polarization signal of $+0.8$ (-0.8)% of the $I_{\rm c}$, and green contours represent a linear polarization signal of 0.8% of the $I_{\rm c}$. The elapsed time between consecutive frames is 33.25 s (except between the last two frames), and runs from left to right, as numbered in continuum intensity maps. This figure is also available within Animation 1 in the electronic edition of Requerey et al. (2014).

using the same IMaX data. In fact, the supersonic upflow associated with this particular magnetic cancellation event is visible in the beginning of Animations 1 and 3 at coordinates $[5'', 33'']$ in Borrero et al. (2010). These quiet-Sun jets have been confirmed in *Hinode*/SP data (Martínez Pillet et al. 2011b), and their relation with horizontal field patches have been highlighted by Quintero Noda et al. (2013).

By the time the positive footpoint moves towards the intergranular lane and the negative one is canceled, three additional patches of positive $V_{\rm s}$ have appeared in contiguous convective downflow areas (frame 9 in Figure 4.2). The whole evolution (frames 1 through 21) of those small magnetic features can be followed in the Animation 1 included in the electronic edition of Requerey et al. (2014). As expected from the small sizes of these magnetic patches, they move along intergranular lanes driven by the horizontal displacement of the granules. This dragging of magnetic patches, gives rise to a number of merging and splitting processes, which result in a bigger and stronger magnetic structure at the end of this phase (frame 21 in the animation). As a result, the magnetic element carries a flux of 5×10^{17} Mx with a field strength peak of 600 G. Note that this and other field strength values given in this work are lower limits, since the inversion assumes filling factor unity. We can call these later stages of evolution as “flux concentration by granular advection”.

Figure 4.3 displays the horizontal velocity maps inferred by the LCT and averaged over this phase ($\sim$ 11 minutes, frames 1-21). The flows derived from the circular polarization show motions of magnetic features. On the other hand, the flows derived from the brightness and the LOS velocities show the evolution of granulation with time. The Gaussian tracking window with a FWHM of $0\rlap{.}''3$ could allow us to infer flows at a sub-granular scale. However, as we are averaging over a time period (21 frames, 11 minutes) much longer than that expected for the lifetime of internal convective velocities, the evolution of granules is the dominant contributor to these horizontal flows. This is supported by Verma et al. (2013), who presented a rigorous testing of the LCT algorithm by comparing their results with velocities in an MHD simulation. In particular, they found that proper motions of single granules are well captured when flow maps are averaged over 15 and 30 minutes, and claim that

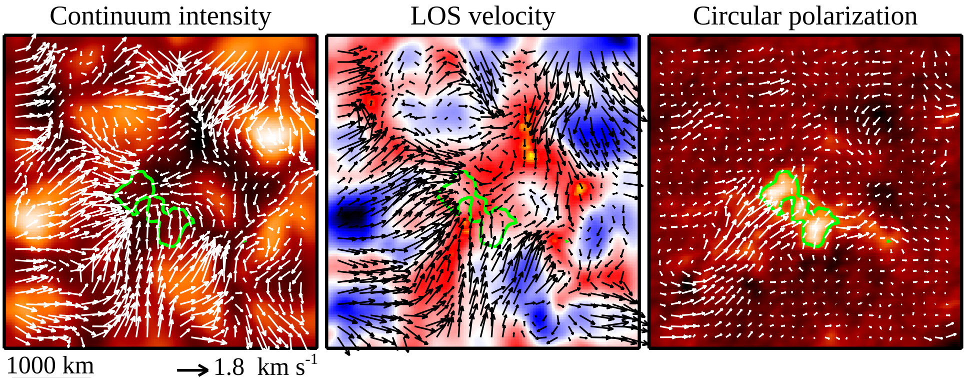

Figure 4.3: Horizontal velocity maps derived through the LCT technique averaged over the flux concentration phase (∼ 11 minutes, frames 1-21). Proper motions of the parameters shown in Figure 4.2 are displayed. From left to right: continuum intensity, LOS velocity, and mean circular polarization. The images are averaged in time over this phase. The length of the black arrow at the lower right corner of the first panel corresponds to $1.8\,\mathrm{km\,s^{-1}}$. Green contours over the averaged maps represent a circular polarization signal of $+0.5\,\%$ of the I_c.

even with very narrow sampling windows and short time cadences, recovering details of the plasma flows might be unreliable.

The proper motions of continuum intensity and LOS velocity illustrate how granules converge towards the center of the maps where the strongest magnetic flux concentration is found. The circular polarization map shows that the small magnetic patches also move in the same direction as the granules, so that the magnetic flux is concentrated in the center of the map. Any motion of magnetic features then simply implies a motion caused by the evolution of granulation. Thus, the magnetic features can stay within the lanes all the time and still move dragged by these flows. Therefore, Figure 4.3 is indicative of flux concentration by granular advection.

In summary, we can say that this phase encompasses four clear stages, namely, a) the rise of an Ω loop within a granule; b) the expulsion of footpoints towards nearby intergranular lanes; c) flux cancellation of one of the footpoints with an opposite-polarity patch, likely through a reconnection process; and d) the increase of flux in the other footpoint by merging with pre-existing patches of the same polarity, driven by granular advection.

4.4 Formation of a kiloGauss magnetic flux tube

Figure 4.4 shows the formation of a small kG flux concentration. In frame 22 there is a small magnetic patch formed during the flux concentration phase described above. The magnetic

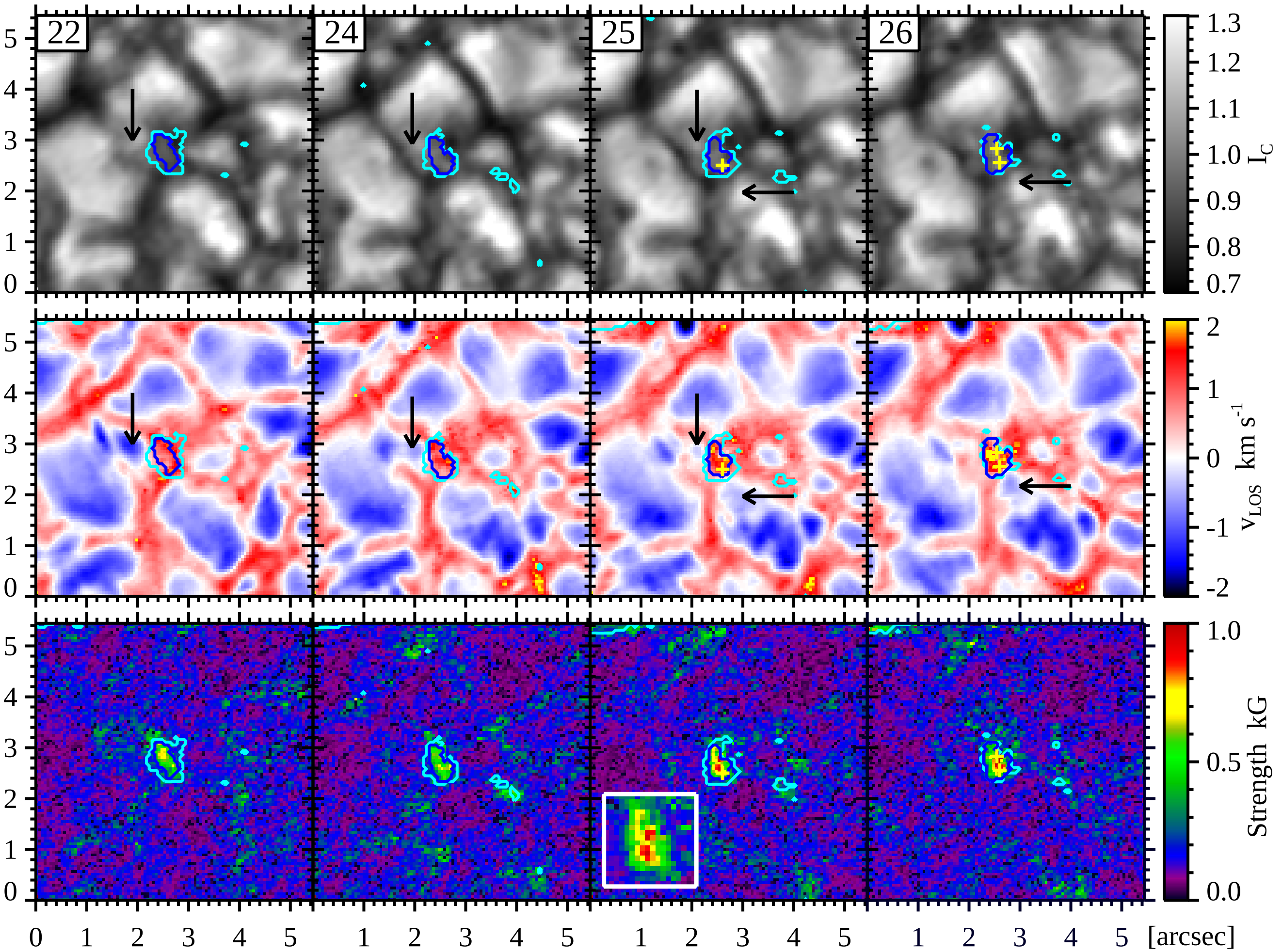
22
24
25
26
0
1
2
3
4
5
[arcsec]
1.3
1.2
1.1
1.0
0.9
0.8
0.7
I_C
2
1
0
-1
-2
v_{LOS} km s^{-1}
1.0
0.5
0.0
Strength kG

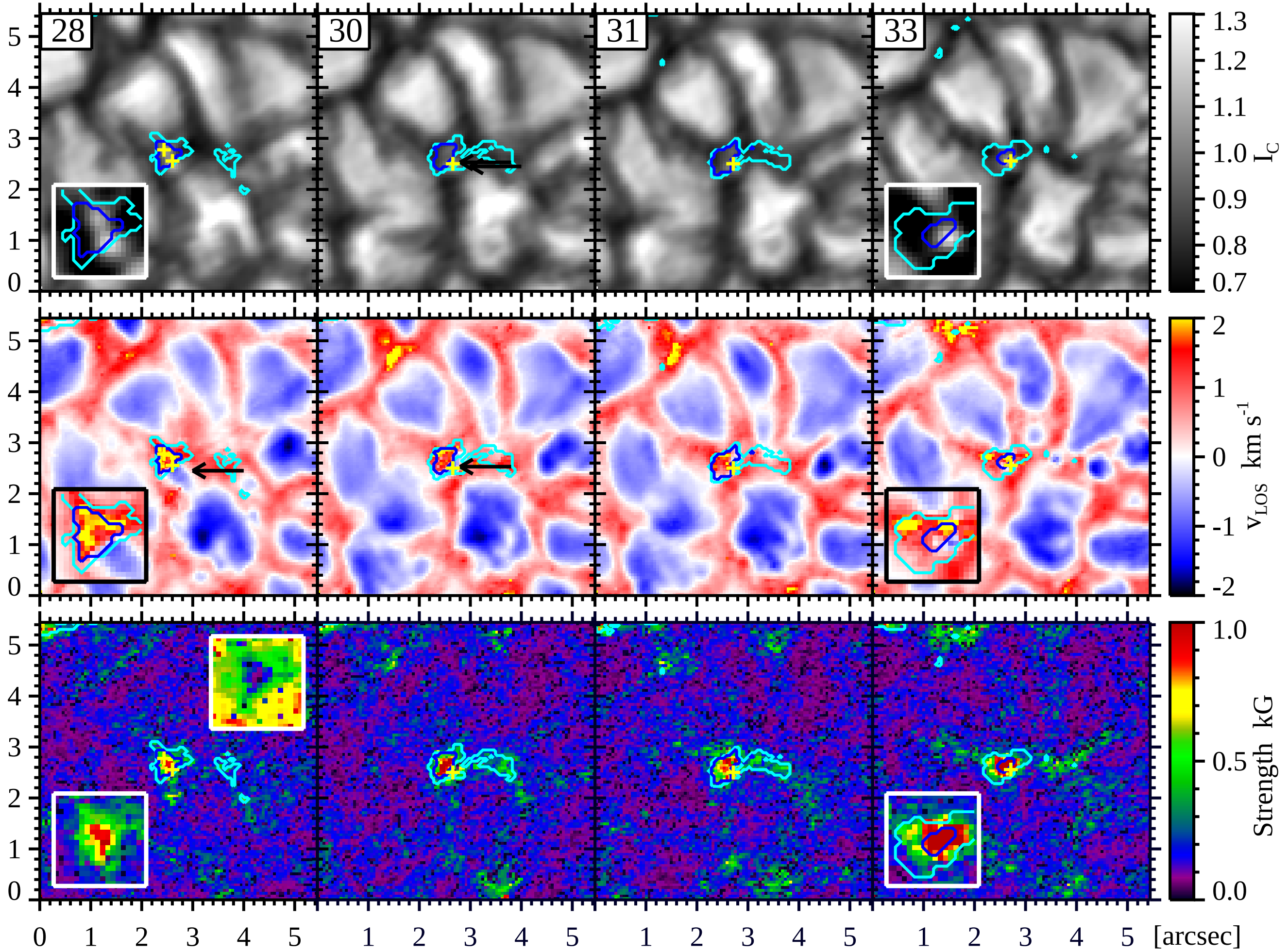
28
30
31
33
0
1
2
3
4
5
[arcsec]
I_C
1.3
1.2
1.1
1.0
0.9
0.8
0.7
v_{LOS} km s^{-1}
2
1
0
-1
-2
Strength kG
1.0
0.5
0.0

Figure 4.4: (Previous page.) Same as Figure 4.2, during the formation of a kiloGauss magnetic element phase. Note that here the bottom rows show field strength maps instead of circular polarization. Cyan line represents iso-magnetic flux density contours of 1×10^{15} Mx. Blue line delineates regions containing a time-constant magnetic flux of 3.5×10^{17} Mx. The yellow cross marks show the bright points location, and the arrows point to small-scale converging upflow features. White boxes display a zoom of the magnetic element for continuum intensity (saturated to [0.85,1.15] I_c), field strength and inclination (only in frame 28); the latter is saturated to [20,120] degrees. The black boxes display a zoom of the LOS velocity. This figure is also available within Animation 1 in the electronic edition of Requerey et al. (2014).

structure has field strengths of about 400 G with a maximum value up to roughly 600 G in its center. These strengths are of the order of the typical equipartition field strength (300-500 G) for granules. Note that only eight of the total twelve frames of this intensification phase are shown. From top to bottom, rows correspond to continuum intensity, LOS velocity, and magnetic field strength. Overplotted are contours defining the magnetic element. The innermost, blue one corresponds to a region of constant magnetic flux. The external, cyan contour marks regions with longitudinal field components stronger than 60 G. These two contours will be used until the end of the present study. Inserts display zooms of the magnetic structure near the centers of the frames. Two inserts are plotted for the magnetic field strength in frame 28: the bottom one shows a blow-up of the field strength while the top one displays a map of the magnetic inclination in order to illustrate that indeed the magnetic element resembles a fully resolved, canonical flux tube where and almost vertical ($\sim 20°$) inner core is surrounded by more inclined ($\sim 70°$), canopy-like magnetic fields. The outer, 60-G contour is mostly used to illustrate how very small magnetic patches, external to our main structure at the beginning of this phase, progressively increase in size and are advected by granules until they merge with our structure in frame 31.

Let us concentrate now on the constant-flux region enclosed by the inner contour. It encloses a magnetic flux of 3.5×10^{17} Mx during this evolution phase. As shown in the first frame, this magnetic patch is embedded in an intergranular lane. As time goes on, the area enclosed by this contour decreases sharply while downward motions and field strengths increase within it until kG fields are reached. To quantitatively analyze the evolution in detail, we select the magnetic core of the structure as the centroid of field strengths within the above-mentioned constant-flux contour. The upper panel of Figure 4.5 displays the LOS velocity (crosses and black line), the magnetic field strength (asterisks and red line), and the continuum intensity (diamonds and green line) of such a magnetic flux tube core and the area (triangles and blue line) of the constant flux region. To increase the S/N in the magnetic core physical parameters, we represent averages over the core itself and its eight surrounding pixels. Although not explicit in the axis legends, areas are measured in Mm^2 and multiplied

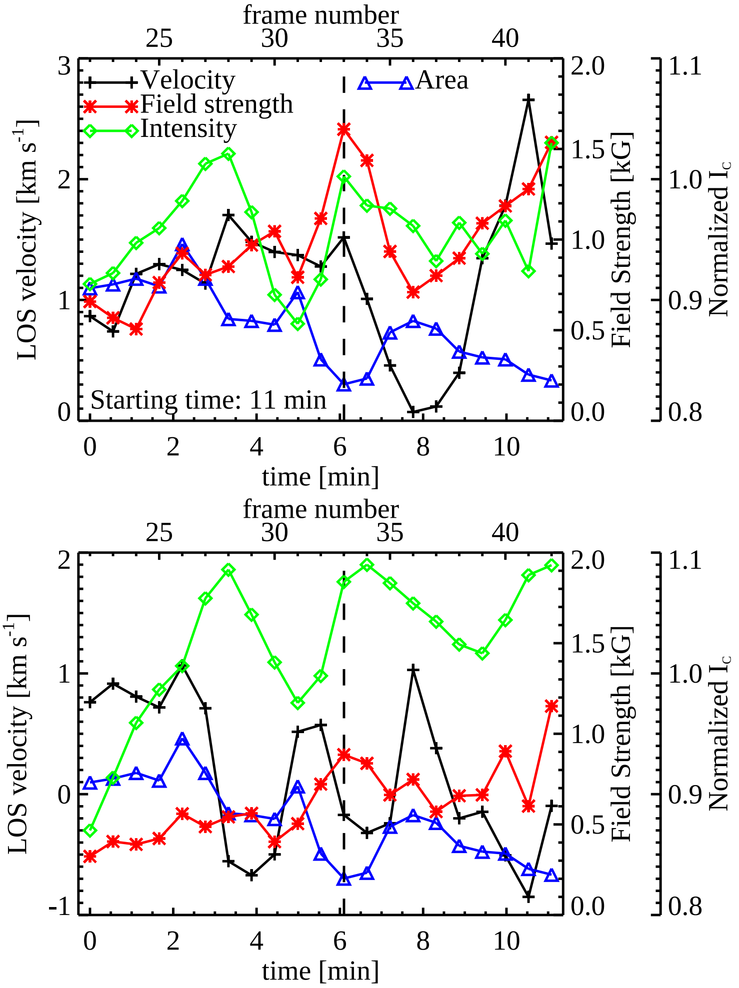

Figure 4.5: Evolution of LOS velocity (black line with plus symbols), field strength (red line with asterisks), and continuum intensity (green line with diamonds), of the flux tube core (Figure 4.5 (a)) and one of the bright points (Figure 4.5 (b)), for frames 22-42. The flux tube core is defined by the blue contour shown in Figures 4.4 and 4.6, which contains a constant magnetic flux of 3.5×10^{17} Mx. We display the evolution of the flux tube core area (blue line with triangles) in both a and b panels. The area is measured in Mm^2, and we use the same y-axis as the one for LOS velocity. Note that the area has been multiplied by a factor 10 for better visualization. In addition, a value of 1 is subtracted from it in panel b. The physical parameters are extracted by averaging over 9 pixels around the centroid of the magnetic core and bright point for the panels respectively. The dashed vertical line indicates the end of the first intensification and the beginning of an oscillation phase. Time 0 in the x-axis corresponds to 11 minutes after the observations started, as marked in the Figure. The upper x-axis at the top of each panels mark the frame numbers as shown in Figures 4.4 and 4.6.

by 10 so that they can be read with the same scale as LOS velocities. Labels in the upper horizontal axis corresponds to frame numbers. The vertical dashed line corresponds to the end of this phase, at frame 33, 6.1 minutes after its start. At this moment the magnetic field reaches strengths up to 1.6 kG, compared with the initial 600 G, while the downflow has grown from 0.9 $\mathrm{km\,s^{-1}}$ to 1.5 $\mathrm{km\,s^{-1}}$. To estimate the noise-induced uncertainty in the field strength and LOS velocity, we repeated the inversions with 100 different realizations of added noise to the observed Stokes profiles. Amplitudes of $10^{-3}\,I_\mathrm{c}$ were used. The standard deviation of the 100 results is 150 G and 150 $\mathrm{m\,s^{-1}}$. Note that the area of the whole magnetic structure runs in almost anti-phase to the strength of the magnetic core, decreasing from 0.11 to 0.03 $\mathrm{Mm^2}$. This indicates that magnetic flux is conserved and that the flux contribution of the canopy fields is not very significant, as expected.

In general, the continuum intensity also seems to gradually increase as the field strength intensifies. However, in this case, there is no clear correlation, i.e, the peak intensity is reached before the field strength has attained its maximum. The change in brightness will be studied in more detail in Section 4.4.2.

4.4.1 Converging granules and small-scale upflow features

From the LOS velocity maps in Figure 4.4, the presence of two small-scale upflows at the periphery of our magnetic element is evident. These upflows lie above the estimated uncertainties. We mark them using small arrows in the I_c and LOS velocity maps.

The first of those features is indicated by a downward arrow from frame 22 to 25. It is a small upflow fragment detached from a bigger granule. It cools down quickly as it converges towards the magnetic structure. It completely disappears before the strongest downward velocities can be observed in the interior of the flux concentration from frame 26 on.

The feature indicated by the left pointing arrow, in frames 25-30, begins as a typical granule-shaped upflow located close to the magnetic structure. As it evolves, it splits in two. The fragment closer to the magnetic element starts to converge towards the flux concentration, while the other half shrinks and brightens. The converging fragment breaks up as it "collides" against the magnetic flux tube. These fragments are also seen in continuum intensity maps. In neither case do we observe the penetration of the features into the magnetic element as they do in Sobotka et al. (1999) for pores. In addition to these fragmenting processes, the granules as a whole continue converging and dragging small magnetic patches towards the center of the map where the magnetic flux concentration is located. In frames 30 through 33, a small magnetic feature is observed to coalescence into our magnetic element as we commented on in Section 4.4.

Besides the above mentioned convergence, the shapes of the granules get perturbed by the presence of magnetic fields. In particular, they lengthen in the direction of the magnetic element and the new weak magnetic feature, thus adopting a "petal-like" appearance whose sharpest corner points towards the magnetic tube. All together, and surrounding the magnetic element, a characteristic "daisy-like" granular pattern (Muller et al. 1989; Muller & Roudier 1992) is observed at the end of the phase (frame 33 in Figure 4.4).

The sum of the above observations makes it seem as if the flux tube behaved as a sink, which attracted the surrounding convective upflows. This effect is clearly observed in Animation 1, included in the electronic edition of Requerey et al. (2014). There are two effects that may contribute to this seeming attraction. Firstly, magnetic elements provide a larger surface area through which radiation can escape and hence the surrounding gas be cooled (Spruit 1976). This leads to more vigorous convection (Deinzer et al. 1984). Secondly, this magnetic element is located at the intersection of a number of granules, where convective downflows are often particularly strong, so that horizontal flows tend to go towards them. Also, magnetic elements are often located near the centres of vortices that pull the nearby granules towards them (e.g., Bonet et al. 2008, 2010), which may also contribute.

4.4.2 Bright points inside the flux tube

On the continuum intensity maps in Figure 4.4, two small-scale BPs are glimpsed inside the magnetic flux tube. The BPs appear as the downflow and field strength increase in the interior of the magnetic element and they are indicated by two yellow plus symbols. They can best be discerned in the insert zoom of the continuum intensity map of frame 28, the scale ranges from 0.85 to 1.15 I_c in order to enhance their contrast. It is worth noting that these BPs are smaller than the magnetic element. Hence, unlike the usual assumption, neither one can be identified with a single flux tube.

The BPs are first located close to the core of the magnetic element (frame 26) and, consequently, can be associated with the flux tube's evacuation. Although not exactly coincident with the core of the magnetic element, the uppermost one is close enough for its brightness evolution to be responsible for most of the continuum intensity variation we see in Figure 4.5 (a). Until the BP disappears in frame 29, its brightness correlates fairly well with the magnetic field strength intensification. Note, however, that at this point in time the field is still comparatively weak. The disappearance is almost simultaneous to the merging of the main magnetic element considered here with smaller magnetic patches mentioned in the first paragraph of Section 4.4. The second BP (the one closer to the canopy) remains observable until the end of the time series. Thus, we can follow the evolution of its continuum intensity, LOS velocity, and magnetic field strength as calculated from an average of the nine-pixel box centered on the BP brightness centroid. Such an evolution is displayed in Figure 4.5 (b). Starting from frame 25, the BP gets closer and closer to the lower edge of the magnetic element as the granules and small granular fragments converge on the magnetic structure. The lowermost upflow feature described in Section 4.4.1 arrives at the same time to that edge, thus producing a reversal in LOS velocity. Simultaneously, the continuum intensity reaches its peak ($1.1\,I_c$; frame 28). Later, the intensity starts to decrease as the small upflow breaks up and the magnetic element merges with the neighboring weak magnetic feature (frames 31-33; see Figure 4.4). Following this, a downflow ($0.5\,\mathrm{km\,s^{-1}}$) is re-established, but not for long because a narrow, weak upflow plume appears at the location of the BP by the end of the intensification phase at frame 33 (see insert). We cannot say whether this upflow feature is actually a part of the magnetic element boundary or just a non-magnetic gas parcel below the tube canopy, but with its emergence, the continuum intensity increases sharply, reaching again values about $1.1\,I_c$. We speculate that the presence of hot (bright) gas next to the magnetic element leads to an intensification of the bright point near the edge of the magnetic feature, since this hot gas heats up and brightens the wall of the magnetic element.

4.5 Mature flux tube

Figure 4.6 shows the newly formed kG magnetic flux concentration. The evolution of the different parameters at the flux tube's core can be followed in Figure 4.5 (a) after the vertical dashed line.

Interestingly, rather than keeping a constant magnetic field strength, it drops below 1 kG where it stays for a number of frames before shooting up again. Oscillations of the strength of quiet-Sun magnetic fields have been observed for the first time by Martínez González et al. (2011) using the same IMaX data. They detected those oscillations by studying the changes with time of the area enclosed in a contour containing a constant magnetic flux. Here we have defined the area in the same way and, as expected, it varies in anti-phase with the field strength, whereas the LOS velocity is in phase with the field strength. First, it decreases to $0\,\mathrm{km\,s^{-1}}$ while the field strength drops to 700 G, and then it grows to $2.8\,\mathrm{km\,s^{-1}}$ as the field strength intensifies to 1500 G. Meanwhile, the continuum intensity remains almost constant in the interior of the magnetic core, around $1.0\,I_c$. However, the intensity of the second BP shows a related oscillatory-like behavior at the wall of the magnetic element (see Figure 4.5 (b) after the vertical dashed line), reaching large values at times when the field strength is also large.

We have already mentioned the emergence of a small upflow plume at the end of the first intensification phase (when the area is smallest). As shown in Figure 4.6, the following evolution of the BP is closely associated with that of the small upflow. Note that the upflow is observed exactly at the location where the BP is present. This fact can also be seen quantitatively in Figure 4.5 (b), after the vertical dashed line. As the upflow weakens, the gas cools down, the area increases and the intensity is reduced (time steps 34-36). Soon after that (time step 38) the area of the magnetic element starts to decrease again and a second upflow plume is detected followed by a rise in intensity.

The second upflow feature appears when the magnetic element is being compressed (area reduced) again by the converging surrounding granules. Similar to those described in Section 4.4.1, two small-scale upflow features are again detected moving towards the flux concentration (indicated by arrows in Figure 4.6, frames 40-42). From the corresponding I_c maps, it can be concluded that they are associated with the splitting of neighboring granules. In addition, the daisy-like appearance is again enhanced.

Furthermore, the emergence of the small upflow takes place while a strong downflow of up to $2.8\,\mathrm{km\,s^{-1}}$ develops in the interior of the flux tube. Correspondingly, an upward/downward velocity pattern is observed within the magnetic element (frames 40-42). Similar small-scale upflow features often surrounded by ring-shaped downflows have already been observed in active plage regions (Narayan & Scharmer 2010). They detect them in large structures rather than in isolated BPs, which mostly show downflows, and interpret them as part of a small-scale magnetoconvection in the interior of a strong plage solar magnetic field.

The anti-phase behavior of the velocity and brightness in the brightest point of the magnetic feature, suggests that at least some of the continuum brightness enhancements in the magnetic element are related to the presence of flows within it. We did not find any previous mention of such a relation between brightness and LOS velocity in BPs. This can be understood in terms of magnetoconvection, with upflows bringing hot gas from below to cool and radiate away at the solar surface. But equivalently, it could also be explained by (magneto-acoustic) waves. Indeed, upwardly propagating acoustic waves are ubiquitous in quiet-Sun magnetic bright points and 3D MuRAM simulations (Jess et al. 2012). Whatever the mechanism may be, the intensity at the core of the magnetic element stays almost constant, with values close to $1.0\,I_c$, while the BP brightness oscillates with an amplitude of $0.1\,I_c$ as the small upflow features evolve.

4.5.1 Downflow plumes

As soon as the mature kG magnetic element is formed, and in agreement with Steiner (1999), two strong downflow plumes start to be clearly visible at the edge of the magnetic element in Figure 4.6 (frames 34 and 35). As an example, the rightmost downflow has a mean

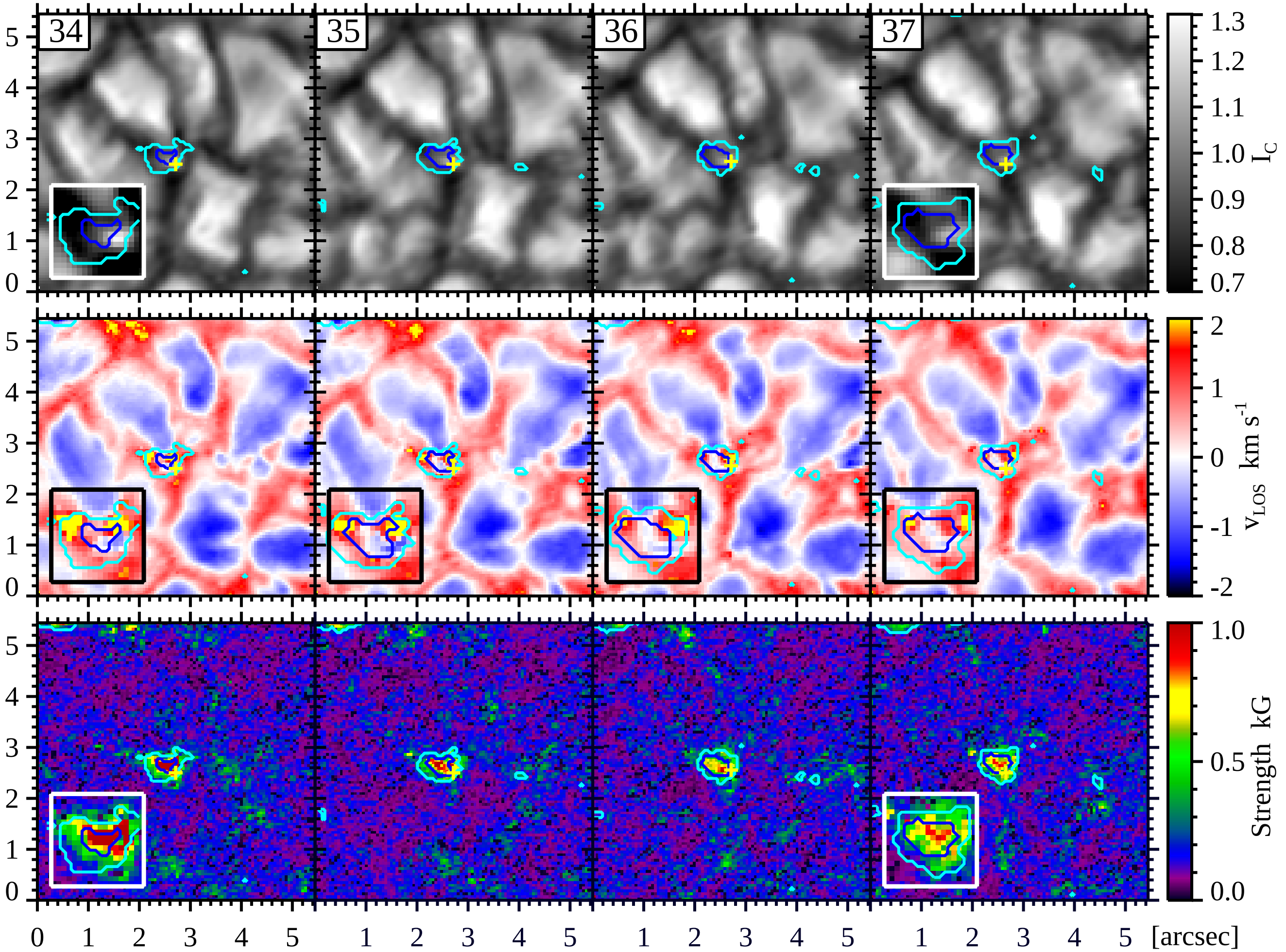
34
35
36
37
0 1 2 3 4 5
0 1 2 3 4 5 [arcsec]
1.3 1.2 1.1 1.0 0.9 0.8 0.7
I_C
2 1 0 -1 -2
v_{LOS} km s^{-1}
1.0 0.5 0.0
Strength kG

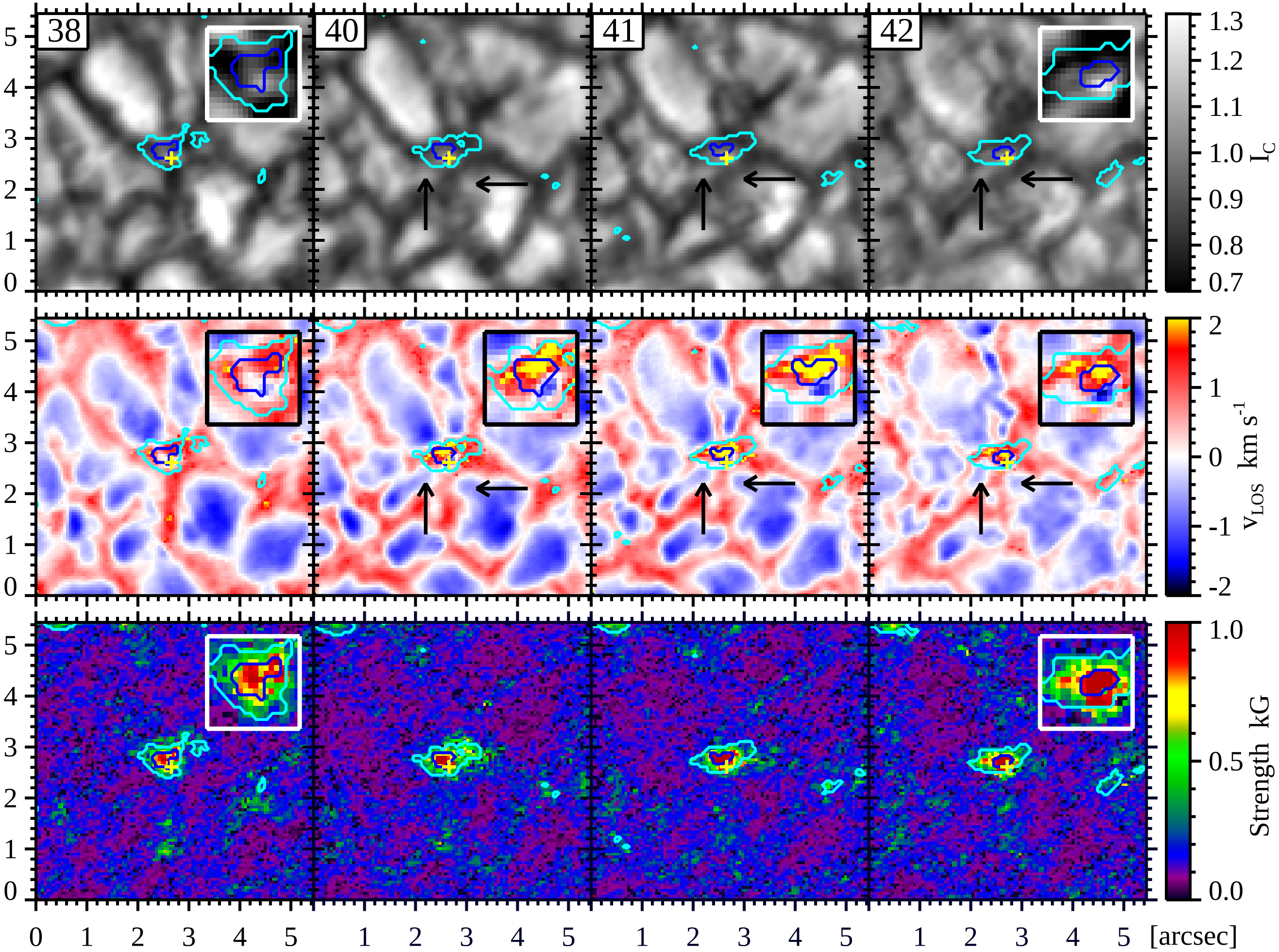
38
40
41
42
0
1
2
3
4
5
1.3
1.2
1.1
1.0
0.9
0.8
0.7
I_C
2
1
0
-1
-2
v_{LOS} km s^{-1}
1.0
0.5
0.0
Strength kG
[arcsec]

Figure 4.6: (Previous page.) Same as Figure 4.4, during the evolution of the mature flux tube. This figure is also available within Animation 1 in the electronic edition of Requerey et al. (2014).

value of 2 km s^{-1} with speeds roughly up to 6 km s^{-1} (hence, almost supersonic) during its evolution. These very high speed values have to be taken with caution because of the poor sampling of the spectral line in our data. Nevertheless, the Stokes profiles at these points display significant Doppler shifts although their quantitative value may be more uncertain than those for slower downflows. The downflows get weaker after two minutes, but they strengthen again around the same location at the end of the time sequence. Such strong downflows have been predicted by Steiner et al. (1998) in 2D models of magnetic flux sheets. In their 2D simulations, the downflows are fed by horizontal flows, and they evolve into "jets" as they become narrower and accelerate with depth. Here, the downflows appear in front of elongated converging granules. Accordingly, the gas required for producing such strong and narrow downdrafts is likely provided by these granules.

4.6 Averaged history

In order to provide a global picture of the flux tube's history, in Figure 4.7 we display the horizontal velocity maps averaged over the whole time series ($\sim$23 minutes, frames 1-42). Figure 4.7 is also complemented by an animation where we show movies of continuum intensity, LOS velocity, circular polarization, and field strength maps. Making use of the LCT horizontal velocities we track the advection of passive tracers (corks) initially spread out all over the FoV (Simon et al. 1988).

The horizontal velocity obtained from the continuum intensity and LOS velocity point toward the magnetic feature near the centre of the FOV in Figure 4.7. A sink is centered at or close to the magnetic element throughout the data set, as persistent flows pointing towards it can be seen after averaging for 20 minutes (several times the life time of a granule; see Verma et al. 2013). Note that the flows tracked by LCT mainly show the evolution of the granulation with time, so that the converging flows imply that granules and granular fragments converge toward the center of the map. On the other hand, the circular polarization shows the advection of the sub-arcsecond magnetic patches, as described by the flux concentration phase.

The cork movies shown in the Animation 1 are very interesting. As time goes by, the corks flow towards the structure. While the continuum intensity tracers penetrate the magnetic feature, the ones for the LOS velocity end up at its border. The continuum intensity corks concentrate at two different inner borders of the structure. The location of the BPs

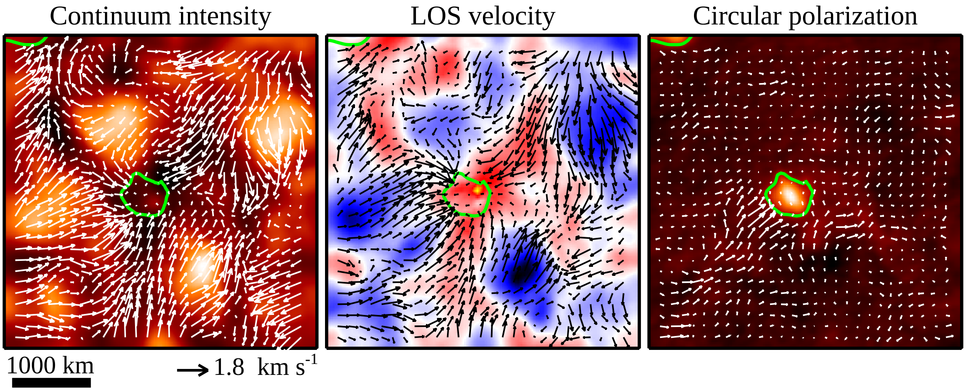

Figure 4.7: Same as Figure 4.3, but averaged over the whole data set (∼23 minutes, frames 1-42). This figure is also available within Animation 1 in the electronic edition of Requerey et al. (2014).

described in Section 4.4.2 match very well with those two concentrations. Furthermore, the LOS velocity corks show two accumulation points at two opposite edges of the structure. The downflow plumes described in Section 4.5.1 are observed close to if not within these accumulation points.

4.7 Summary and Conclusions

We have presented high resolution observations of the formation and evolution of an isolated quiet-Sun magnetic element and its interaction with the neighbouring convection. We have analyzed the polarization maps and used the SIR inversion code to retrieve LOS velocities and the vector magnetic field.

The history of our magnetic element starts with a small-scale magnetic Ω loop emerging in a granular upflow. The footpoints are dragged out into nearby intergranular lanes where some pre-existing, sub-arcsecond, positive circular polarity patches are already present. The linear polarity feature disappears at the same time as the negative footpoint cancels with one of those positive polarity patches. This cancellation is associated with a supersonic magnetic upflow detected by Borrero et al. (2010), which is probably a signature of magnetic reconnection between the cancelling opposite polarity magnetic features. The positive polarity footpoint and the pre-existing flux patches are swept along the lanes by converging granules and concentrated roughly up to (and possibly even beyond) the equipartition field strength (300-500 G).

This process is unable to concentrate the magnetic field significantly above equipartition values. Further intensification is achieved when downdrafts inside the magnetic field concentration are enhanced. According to the canonical convective collapse picture, at this point the tube is evacuated and the flux is compressed by the excess pressure of the surrounding gas. This compression leads to a reduction in the area of the flux concentration and an enhancement of its field strength. This phase of convective collapse is qualitatively consistent with the results of 3D MuRAM (Vögler et al. 2005) simulations and their comparison with *Hinode*/SP observations by Danilovic et al. (2010a). During this process, and due to the formation of a Wilson depression (Spruit 1976), the nearby gas cools and hence has a reduced pressure, creating a horizontal pressure gradient with respect to the gas that is located further away. Driven by the pressure gradient, gas then flows towards the magnetic feature. The traces of this inflow can be seen in Figure 4.7. The field lines act as a stiff hindrance to granular convection, so that a characteristic daisy-like granular pattern forms, in agreement with the observations of Muller et al. (1989) and Muller & Roudier (1992).

As the flux tube gets cooler than its surrounding at a given geometrical height, it is irradiated laterally from the gas in its immediate surroundings, which is fed by the converging granules and granular fragments. We observe the formation of two BPs within a seemingly single magnetic element.[2] Both are located at or close to the boundary of the kG feature. We trace the bright point located at the lower edge of the magnetic element using the same approach as Nagata et al. (2008) and find that at the end of the convective collapse phase it displays an upflow. A similar upflow has also been seen by Bellot Rubio et al. (2001). They interpret it as a “rebound” arising when the internal downflows turn into upflows, and associate them with the destruction of the flux tube. However, in our study, the small-scale upflow feature does not destroy the magnetic flux tube and rather a large-amplitude variation in area and field strength is observed which may be part of an oscillatory pattern (only a single period is seen, due to the limited length of the observation).

We find that the field strength varies in anti-phase with the area enclosed by a contour of constant magnetic flux, supporting the conclusion drawn by Martínez González et al. (2011) that oscillations in this area are proportional to oscillations in field strength. In the tube core, LOS velocity also changes in anti-phase with area. In the BP case however, brightness also varies in anti-phase with area while LOS velocity does it in phase. The BP follows the evolution of an emerging upflow plume. The upflow dissolves as the area increases in size, and a second upflow appears while the area recovers its initial value. Through this evolution the BP oscillates with an amplitude peak of $0.1\,I_\mathrm{c}$ above the almost constant brightness intensity at the tube core of about $1\,I_\mathrm{c}$.

---

[2] Notice that in frame 25 of Figure 4.4 the magnetic element displays two close cores with strengths above 1 kG that subsequently merge in frame 26. This is a phenomenon that can be better seen in other magnetic structures of the same data set and whose study and discussion is deferred to Chapter 5.

Unfortunately, the data-set limited time span does not allow us to know whether an oscillations will continue or not. However, the magnetic field oscillations detected by Martínez González et al. (2011), as well as observations of BPs experiencing several brightness enhancements during their life (Muller & Roudier 1992), suggest that the magnetic element could undergo more oscillations.

Once the mature flux tube has been formed, we also find narrow, strong downflows at it edges. Two-dimensional models by Steiner et al. (1998) predict flux sheets bordered by narrow downflows. The classical picture for the creation of asymmetries in the presence of canopies (Grossmann-Doerth et al. 1988; Solanki 1993) predicts the appearance of such downflows. Bellot Rubio et al. (1997, 2000) already detected them in unresolved magnetic flux tubes. Here, we do not find rings of downflows bordering the magnetic structure, but rather downflow plumes at the edge's of the flux concentration, similar to those observed by Rimmele (2004) in active region flux tubes. These downflows are accompanied by small-scale upflow features that appear at the external border of the magnetic element core. Our high spatial resolution findings agree very well with those obtained by Martínez González et al. (2012b), also based on IMaX data.

Our new observation of a strong anti-phase correlation between the continuum intensity and the LOS velocity within the BP deserves a small discussion. A first suggestion can be drawn out of it: at least part of the continuum brightness of the magnetic feature is related to the presence of flows within it. Most notably, the brightness enhancement and the anti-phase velocity are not seen in the central, strongest core of the magnetic element. Rather they appear at well-localized, small-scale places of its external part. Whether this phenomenon is common to this type of elements or not cannot be ascertained from our present data. Further studies focused on this topic promise to offer new insight into the physics of quiet-Sun magnetic flux tubes.

Several mechanisms can be invoked to explain the possible oscillatory behavior. Overturning magnetoconvection could be one such mechanism as the detailed studies by, e.g., Weiss et al. (1996) suggest. Another possible scenario is provided by overstable oscillations (Spruit 1979; Hasan 1985) that can start as soon as the collapse has stopped. If the pattern we observe is not of a convective origin, we then have a third possibility: we might be witnessing the upward propagation of acoustic waves (Jess et al. 2012). If so, waves could be excited through magnetic pumping (Kato et al. 2011). Indeed, transient downflows in the immediate surroundings of a magnetic element, downdraft and upflows within the flux tube, and constant magnetic flux area oscillations are signatures of such a mechanism. Alternatively, the fourth option can be found in "sausage" modes (Edwin & Roberts 1983) excited through compression by granules. The very large amplitude of the oscillation in basically all variables, in particular in the magnetic field strength may also be a sign that it is not a true oscillation at all, but rather multiple episodes of convective collapse, with a loss of equilibrium in between. What is causing the flux tube field to be so unstable has not become entirely clear from this study. However, the absence of a strong upflow during the decay phase of the field strength suggests that this phase is not initiated by a strong upflow (rebound shock) such as that found by Grossmann-Doerth et al. (1998). Since we are only looking at a photospheric height, the present observations do not allow us to distinguish between the different mechanisms. In order to study the chromospheric response, we plan to supplement IMaX observations with the simultaneous Ca II H filtergrams from the Sunrise Filter Imager (SuFI; Gandorfer et al. 2011).

It is evident that the formation and the subsequent evolution of a solar magnetic element is a complicated problem, where many phenomena take place, namely, emergence of a magnetic Ω loop, expulsion of its footpoints from a granule, merging of flux patches in a long-lived inflow, formation of a kG magnetic element by convective collapse and granular compression, a subsequent weakening of the field strength to further increase again to kG values either through an oscillation or a second collapse. For the first time, we have been able to observe and relate all these phenomena in a single example.

5

DYNAMICS OF MULTI-CORED MAGNETIC STRUCTURES IN THE QUIET SUN

We report on the dynamical interaction of quiet-Sun magnetic fields and granular convection in the solar photosphere as seen by SUNRISE. We use high spatial resolution ($0\farcs15$–$0\farcs18$) and temporal cadence (33 s) spectropolarimetric Imaging Magnetograph eXperiment data, together with simultaneous CN and Ca II H filtergrams from SUNRISE Filter Imager. We apply the SIR inversion code to the polarimetric data in order to infer the line of sight velocity and vector magnetic field in the photosphere. The analysis reveals bundles of individual flux tubes evolving as a single entity during the entire 23 minute data set. The group shares a common canopy in the upper photospheric layers, while the individual tubes continually intensify, fragment and merge in the same way that chains of bright points in photometric observations have been reported to do. The evolution of the tube cores are driven by the local granular convection flows. They intensify when they are "compressed" by surrounding granules and split when they are "squeezed" between two moving granules. The resulting fragments are usually later regrouped in intergranular lanes by the granular flows. The continual intensification, fragmentation and coalescence of flux results in magnetic field oscillations of the global entity. From the observations we conclude that the magnetic field oscillations first reported by Martínez González et al. correspond to the forcing by granular motions and not to characteristic oscillatory modes of thin flux tubes.

5.1 Introduction

Most of our empirical knowledge of the structure and dynamics of quiet-Sun magnetism derives from observations of the solar photosphere. In this thin layer, magnetic energy is in many places of the same order as the kinetic energy. Therefore, the interaction between the magnetic field and convection at the solar surface is an efficient way of converting kinetic energy into a form that can be transported to the upper layers of the solar atmosphere by the magnetic field.

The most direct method of detecting the solar magnetic field is by measuring polarized light generated via the Zeeman effect. Unfortunately, in the quiet Sun, the Zeeman effect produces only a weak polarization signal, whose measurement requires both, high spatial resolution and accurate polarimetric sensitivity. Such measurements have only recently been achieved by the *Hinode* Spectro-Polarimeter (Lites et al. 2013) and the Imaging Magnetograph eXperiment (Martínez Pillet et al. 2011a) aboard the SUNRISE balloon-borne solar observatory (Solanki et al. 2010; Barthol et al. 2011; Berkefeld et al. 2011; Gandorfer et al. 2011).

Before the era of space-borne spectropolarimeters, polarimetric observations have been limited by the need for stable seeing conditions to achieve a high spatial resolution. Instead, to maximize spatial and temporal resolution, indirect signatures, or proxies of magnetic structures have been used. In particular, magnetic elements, usually described in terms of flux tubes, have been tentatively identified with bright points (BPs) in photometric observations. Based on a recent comparison between SUNRISE observations and MHD simulations, Riethmüller et al. (2014) deduce that all magnetic BPs are associated with kG magnetic flux concentrations.

White-light observations obtained at the Pic du Midi Observatory in the French Pyrénées, revealed a mean lifetime of 18 minute for facular (Muller 1983) and network (Muller & Roudier 1992) BPs. Many BPs become elongated when they are squeezed between two moving or expanding granules (Roudier et al. 1994). 70% of these elongation processes end with the fragmentation of the bright structures.

Muller & Roudier (1984) were the first to observe bright points in the Fraunhofer G band, a CH molecular band-head around 430.5 nm. At these wavelengths BPs exhibit higher contrast than the one they display in the continuum. Berger & Title (1996) studied the dynamics of G-band bright points observed with the 50 cm Swedish Vacuum Solar Telescope (Scharmer et al. 1985) on the island of La Palma, Spain. Driven by the evolution of the local granular convection flows, fragmentation and coalescence are two important processes that govern the evolution of BPs. BPs also appear to rotate and fold in chains or groups. Periodically, they split into smaller fragments, merge with other BPs, and sometimes fade until they are no longer distinguishable from their surroundings. Nonetheless, Berger et al. (1998) found some BP groups to persist during the entire 70 minute data set. However, the different members of these chains cannot be identified as individual entities for longer than a granule lifetime, i.e., 6-8 minutes. Consistent with this view, Berger & Title (1996) concluded that the canonical picture of stable, isolated flux tube does not agree with observations.

Simultaneous filtegram and magnetogram observations revealed that continuum and line-core BPs (Keller 1992; Title et al. 1992; Yi & Engvold 1993) and G-band BPs (Berger & Title 1996, 2001) appear associated with a magnetic feature. While isolated BPs have nearly the same size as the associated magnetic element, BP groups appear inside a large magnetic structure that extends beyond the group. For the largest magnetic structures, Muller et al. (2000) found several magnetic signal maxima at the location of individual BPs.

If we assume that BPs are the counterparts of magnetic flux tubes, their fragmentation by the perturbation of surrounding granules might indicate that magnetic elements are liable to the interchange, or fluting, instability (e.g., Krall & Trivelpiece 1973, Chap. 5). Parker (1975) and Piddington (1975) noticed that the interchange instability is indeed an intrinsic property of flux tubes. However, due to the reduced density of the magnetic plasma, Meyer et al. (1977) showed that flux tubes with fluxes greater than about 10^{19} Mx, such as sunspots and pores, can be stabilized by buoyancy thanks to the rapid expansion with height of their field. Small quiet-Sun magnetic structures with fluxes in the range of 10^{16}–10^{18} Mx (e.g. Wang et al. 1995a) obviously do not fulfill this criterion. Schüssler (1984) proposed that such features could be stabilized as well if they are surrounded by whirl flows, with a whirl velocity around magnetic features between 2 and 4 km s^{-1} (Bünte et al. 1993). Observations of whirl flows were first reported by Bonet et al. (2008). However, their lifetimes are only about 5 minute, on average, as they often do not survive neighboring granules, which have a similar lifetime (Bonet et al. 2010).

Stabilization of magnetic elements by means of the whirl flow mechanism is restricted to cylindrical flux tube geometry. Bünte (1993) showed that elongated magnetic slabs, or flux sheets, are also flute unstable. He demonstrated that the slabs are most strongly liable to the instability in a layer close to $\tau_c = 1$, where fragmentation into single tube-filaments takes place. These filaments, however, lose their identity at lower and upper layers as they merge into a single, stable magnetic slab. Of course, the validity of such idealized computations in the real, highly dynamic, turbulent solar photosphere remains an open question.

In order to shed new light on the physical mechanism behind the dynamic nature of quiet-Sun magnetism, high spatial and temporal resolution is required over a sufficiently long time series, along with accurate polarimetry. Such high-quality observations have only recently been achieved with SUNRISE/IMaX. The unprecedented spatial resolution of $0''.15$–$0''.18$, allowed for the first time photospheric magnetic elements to be spatially resolved even in the quiet Sun internetwork without requiring an ad-hoc filling factor, that specifies the fraction of the pixel filled with magnetic field (Lagg et al. 2010). This represents a considerable advance compared to previous works that studied magnetic structures via their indirect signatures, e.g., BPs, or without resolving the magnetic fields.

In Chapter 4, we reported on the first direct observation of the formation of an individual photospheric magnetic element as seen by Sunrise/IMaX. Here, we complement that work by investigating the dynamical interaction of quiet-Sun magnetic structures with the convective flows.

5.2 Observations and data reduction

The spectropolarimetric observational data were obtained with Sunrise/IMaX on 2009 June 9 from 00:36:03 UT to 00:58:46 UT, in a quiet-Sun region close to disk center. The data set of $\sim$23 minutes length has a temporal cadence of 33 s, with a pixel size of $0.^{\prime\prime}055$. Throughout the observing cycle, the full Stokes vector was sampled at five wavelength positions across the Fe I 525.02 nm line (Landé factor g = 3) at λ = -8, -4, +4, +8, and +22.7 pm from the line center (V5-6 mode of IMaX; see Martínez Pillet et al. 2011a, for details). For the polarization analysis, the incoming light is modulated by two liquid crystal variable retarders (LCVRs) and analyzed by a beam splitter. The spectral analysis is performed by a Fabry–Pérot interferometer based on a double-pass $LiNbO_3$ etalon.

IMaX data reduction and instrument calibrations are described by Martínez Pillet et al. (2011a). Several procedures were used for dark-current subtraction, flat-field correction, and polarization cross-talk removal. The calibration set consisted of 30 in-focus and out-of-focus image pairs that, through phase diversity (Gonsalves 1982; Paxman et al. 1996), were used for post-facto point-spread function (PSF) retrieval. The science images were reconstructed by deconvolving this PSF from the originally recorded images. The process requires an apodization that effectively reduces the IMaX field of view (FOV) down to about $43'' \times 43''$. The blueshift over the FOV produced by the Fabry–Pérot interferometer is corrected in the inferred velocity values. The instrument achieved a spectral resolution of 8.5 pm and the spatial resolution has been estimated to be $0.^{\prime\prime}15$–$0.^{\prime\prime}18$ after reconstruction. The noise level in each Stokes parameter is about 3×10^{-3} in units of the continuum intensity, and the rms contrast of the quiet-Sun granulation obtained from continuum data is about 13.5% (Solanki et al. 2010), which testifies to the outstanding quality of IMaX images. We determine the line-core intensity by fitting the observed IMaX Stokes I profiles at the sampled spectral positions by a Gaussian.

In addition to the IMaX Fe I 525.02 nm images, several nearly simultaneous CN (centered at 388 nm with FWHM $\approx$ 0.8 nm) and Ca II H (centered at 396.8 nm with FWHM $\approx$

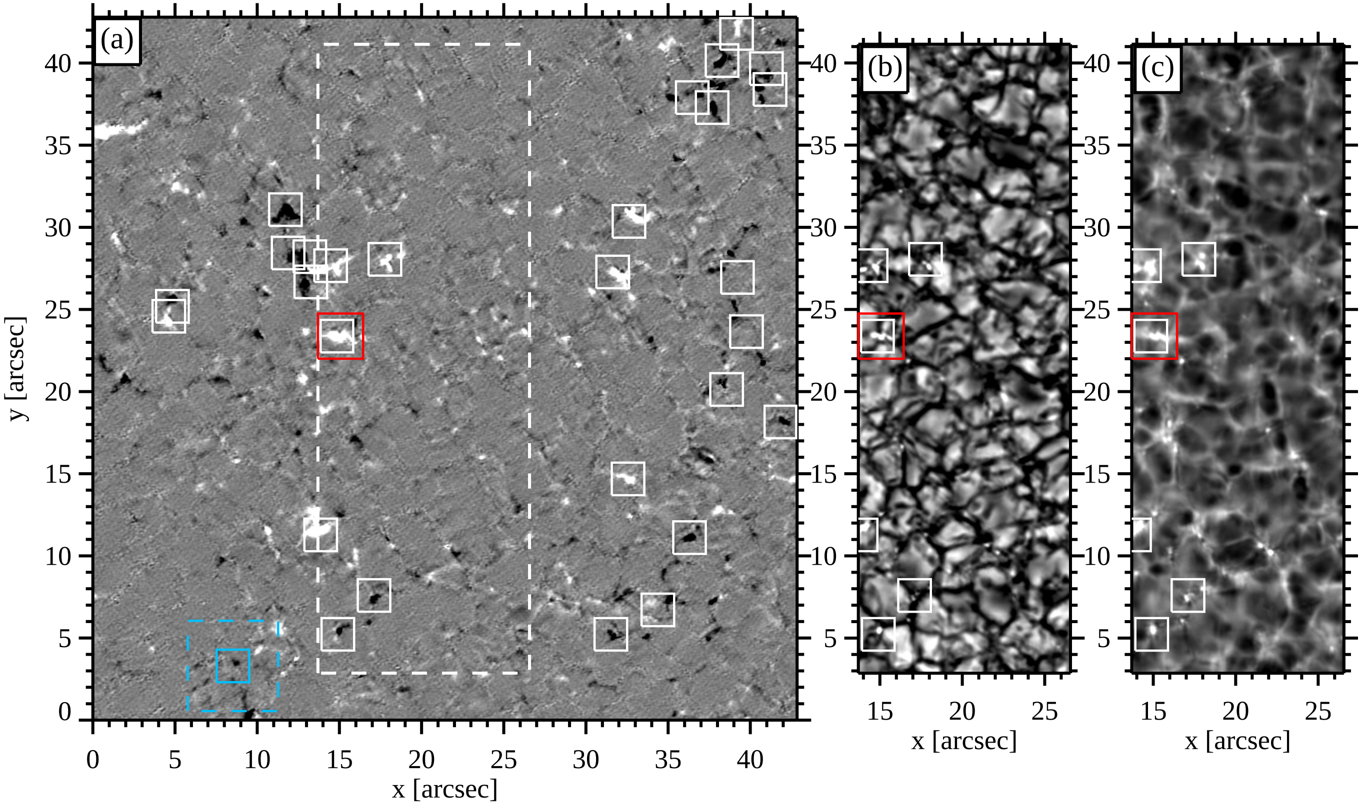

Figure 5.1: Examples of co-spatial images from both, the IMaX and SuFI instruments. (a) IMaX Fe I 525.02 nm longitudinal magnetic field covering the full FOV of about $43'' \times 43''$. The longitudinal component of the magnetic field, $B \cos\gamma$, is linearly scaled from -100 to 100 G. The white dashed-line rectangle, with a FOV of $13'' \times 38''$, illustrates the co-aligned area in common with the SuFI CN and Ca II H images. The white boxes enclose locations where multi-cored magnetic structures are observed. The red and blue boxes highlight features that are examined in detail in Section 5.4 and Figure 5.7, respectively . (b) SuFI CN image. (c) SuFI Ca II H image.

0.18 nm) filtergrams obtained with the SUNRISE Filter Imager (SuFI; Gandorfer et al. 2011) are used in the present Chapter. The time series has a cadence of 12 s, with a pixel size of $0\farcs0207$, and a FOV of about $13'' \times 38''$. The CN and Ca II H bandpass images have been phase diversity reconstructed (Hirzberger et al. 2011).

Since SuFI and IMaX data have different cadences, we select those CN and Ca II H images whose observing times are closest to the IMaX observations. Note that the pixel size is also different. Thus, we increase the size of the SuFI image pixels by neighborhood averaging to a common scale with IMaX. Furthermore, we properly align the images by applying a cross-correlation technique on all simultaneous frames of Ca II H and the IMaX line-core intensity, i.e., the data products having the closest BP contrast.

5.3 Data analysis

To determine the vector magnetic field and the LOS velocity, inversions of the full Stokes vector are carried out with the SIR code (Ruiz Cobo & Del Toro Iniesta 1992) for all time steps in our series. This code numerically solves the radiative transfer equation along the LOS under the assumption of local thermodynamic equilibrium, and minimizes the difference between the measured and the computed synthetic Stokes profiles using response functions.

Starting from the Harvard–Smithsonian Reference Atmosphere (Gingerich et al. 1971) as initial guess (with added magnetic and velocity parameter values), the temperature T, is modified with two nodes.[1] The magnetic field strength B, the inclination and the azimuth angles γ and φ, the LOS velocity $v_{\rm LOS}$, and the microturbulent velocity $v_{\rm mic}$ are assumed to be constant with height. The magnetic filling factor f is assumed to be unity and the macroturbulent velocity $v_{\rm mac}$ is set to zero due to the high spatial resolution of the data. From B and γ we also derive the longitudinal component of the magnetic field $B_{\rm long} = B\cos\gamma$. At each iteration step the synthetic profiles are convolved with the spectral PSF of IMaX, which was measured in the laboratory before the launch of SUNRISE (Riethmüller et al. 2014). To estimate the noise-induced uncertainty in the field strength and LOS velocity, we repeat the inversions with 100 different realizations of added noise to the observed Stokes pro-

---

[1] As usual in SIR, the whole atmosphere is perturbed regardless of the number of nodes. *Equivalent* response functions are calculated at these nodes that include the sensitivity of **all** depth grid points (see Ruiz Cobo & Del Toro Iniesta (1994) and Del Toro Iniesta (2003)). The number of nodes basically indicates the degree in the polynomial spline interpolation that is assumed to apply to the perturbations (not to the final stratification). In the specific case of two nodes, they are put at the first and last point of the grid ($\log\tau_{\rm c} = 1.4$ and -4.0) but such positions are irrelevant: the same linear perturbation is applied independently of the node positions. However, it is worth noting that with only five wavelenght points, the temperature is not well constrained in layers above $\log\tau_{\rm c} = -2$ or below $\log\tau_{\rm c} = 0.5 - 0$.

files. Amplitudes of 3×10^{-3} in units of the continuum intensity were used. The standard deviation of the 100 results is 150 G and 150 $\mathrm{m\,s^{-1}}$ respectively.

Finally, we apply a p-mode subsonic filter (Title et al. 1989) to the continuum intensity, line-core intensity, LOS velocity, CN and Ca II H images, and compute the horizontal velocity maps of the continuum intensity by means of a local correlation tracking (LCT) technique (November 1986; November & Simon 1988) as implemented by Molowny-Horas & Yi (1994). Figure 5.1 displays example frames of an IMaX longitudinal magnetic field (left), a SuFI CN (center) and a Ca II H (right) image after co-alignment.

5.4 Multi-cored magnetic structures

The high spatial and temporal resolution observations allow us to study the dynamics of resolved small-scale magnetic structures. This implies that we are able to track magnetic elements themselves rather than just their proxies, i.e., BPs. We use time series of B_{long} as context data to follow the evolution of magnetic elements. After visual inspection of each maps frame, we identify 28 groups of flux tubes evolving as single entities while the individual tubes undergo different coalescence and fragmentation processes. The locations where such magnetic structures are detected are highlighted by white boxes in Figure 5.1.

Figure 5.2 shows enlarged views of these structures. The longitudinal magnetic field maps (Figure 5.2(a)) illustrate "multi-cored" magnetic structures that are resolvable into a series of more elemental structures, each of which might be described by a flux tube. In general, the magnetic structures are seen in the longitudinal magnetic field maps to have at least two inner cores surrounded by a common and weaker envelope. In most cases, the line core intensity maps display a BP associated with each magnetic core (see Figure 5.2(b)). Thus, the multi-cored magnetic structures are generally characterized by groups of resolved BPs. Similar quiet-Sun bright structures have been previously observed by e.g., Berger & Title (1996); Berger et al. (1998, 2004); Rouppe van der Voort et al. (2005) and Goode et al. (2010). Here we have been able to relate each BP group with a magnetic core group that belongs to a common underlying magnetic structure.

The red box in Figure 5.1 highlights a region of interest containing a representative example of a multi-cored magnetic structure whose dynamics we have followed. We focused on this region because it shows, in a single example, many of the processes involved in the evolution of these magnetic features. In addition, it is one of the comparatively few cases for which we have also information from SuFI. We describe it in some detail in what follows.

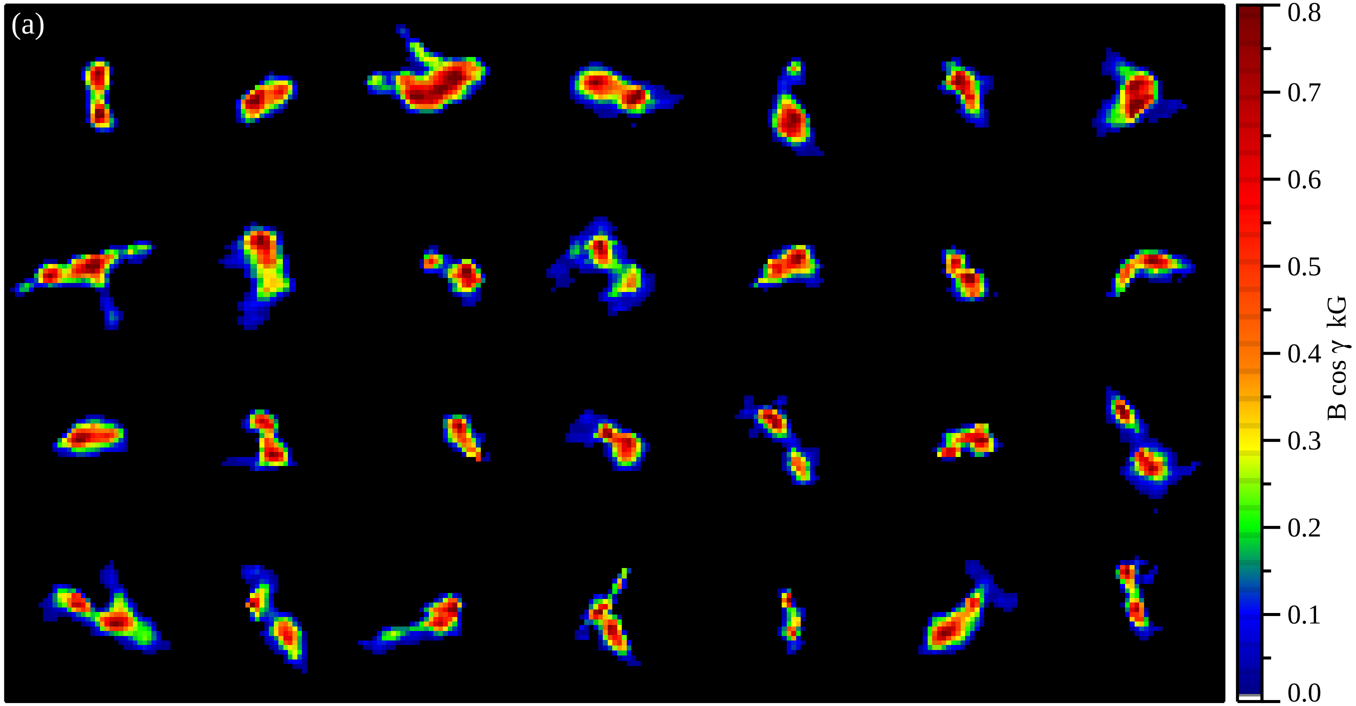
(a)
0.8
0.7
0.6
0.5
0.4
0.3
0.2
0.1
0.0
B cos γ kG

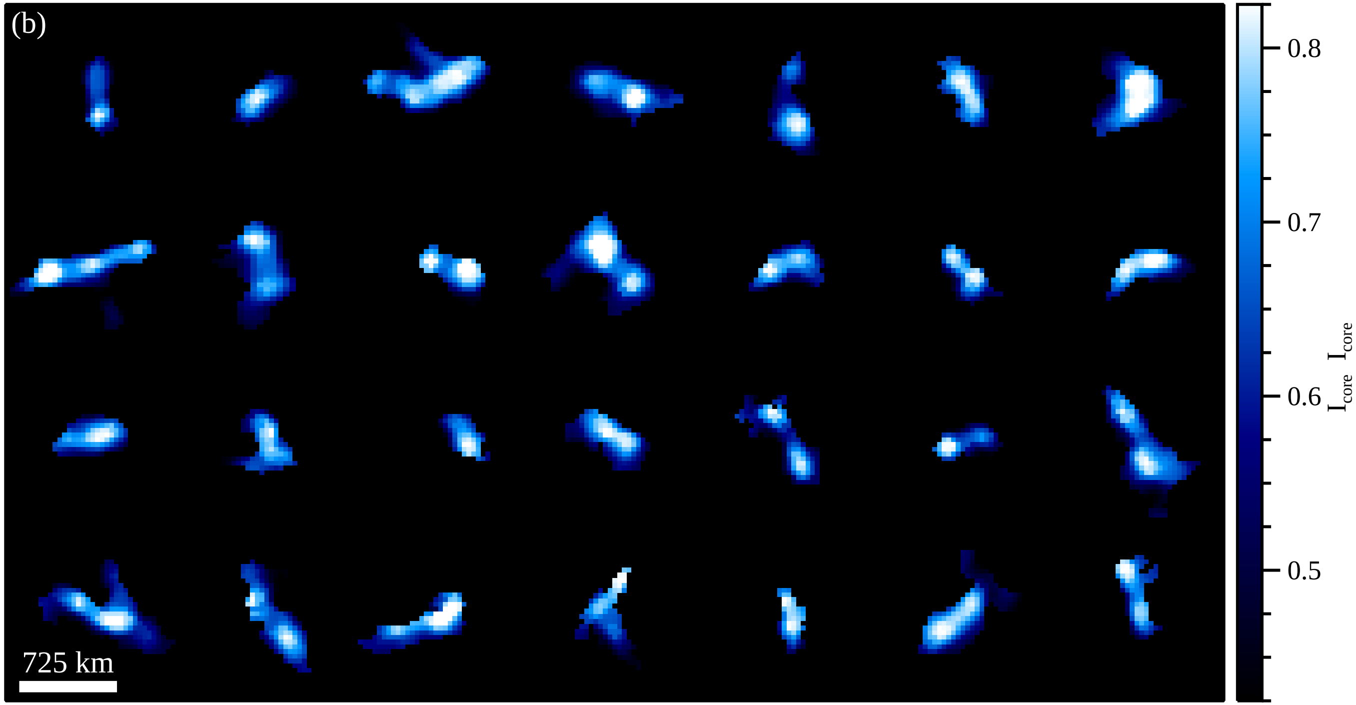

Figure 5.2: Enlarged views of the white boxes in Figure 5.1. Each structure corresponds to a different box and is not co-temporal with the others. (a) Longitudinal component of the magnetic field. (b) Line-core intensity in units of the continuum intensity. For clarity, the plotted line-core intensity has been set to zero outside the magnetic features.

5.5 Evolution of magnetic elements

Figure 5.3 illustrates the temporal evolution of a multi-cored magnetic structure (red box in Figure 5.1) based on five selected B_{long} maps (first row), magnetic field strength and inclination maps (second and third rows), and co-aligned CN maps (fourth row). The blue contour in the last row marks the periphery of the multi-cored magnetic structure. This has been selected by visual inspection in such a way that all the magnetic cores are kept within the global structure. In all frames it delineates longitudinal magnetic field iso-contours of approximately 250 G, and it encloses a magnetic flux of $(5.4 \pm 1.3) \times 10^{17}$ Mx, where ± 1.3 is the amount by which it changes over time. This contour will be used until the end of Section 5.6.

In frame number 13, an elongated CN bright structure, with two seemingly brighter concentrations, is observed. (The existence of two BPs can be confirmed through their evolution as seen in Animation 2.) The co-temporal longitudinal magnetic field map identifies the two brighter concentrations (BPs) with two associated magnetic cores embedded in a more diffuse magnetic structure. These cores are also clearly observed in the field strength and inclination images. The structure is formed by two strong (~ 1000 G) and almost vertical ($\sim 20°$) inner cores surrounded by a common, weaker (~ 400 G) and more inclined ($\sim 70°$), canopy-like ring. Evidence that such rings are associated with canopies in single-cored magnetic structures has been provided by, e.g., Rezaei et al. (2007), Martínez González et al. (2012b) and Buehler et al. (2015). Our highly inclined fields of the rings are fairly consistent without a-priori assumptions with the conventional picture of a canopy. However, their quantitative values may be more uncertain than those from the cores, because the polarimetric signal is weaker over the rings than over the cores. Martínez González et al. (2012b), for instance, found smaller tube expansions with higher spectral resolution from SUNRISE/IMaX, but no linear polarization was studied since only Stokes I and V were available in their case.

The magnetic morphology suggests that the dual-core feature is formed by two magnetic elements (flux tubes) that lose their individual identity as they expand with height and merge together. Canopy merging has been observed by Buehler et al. (2015) in a fairly different scenario: they report on individual magnetic flux concentrations whose canopies blend with those from neighbor concentrations.

The subsequent evolution shows[2] that the rightmost magnetic core splits into two (frame 20). Then the three of them merge and form an isolated magnetic element (frame 32). Soon afterwards, however, it fragments into two apparently identical cores (frame 37) that subsequently start to fuse again into a single magnetic concentration (frame 41). Two small

---

[2] Better seen in Animation 2. We suggest the reader to manually play back and forth the individual frames of the movie.

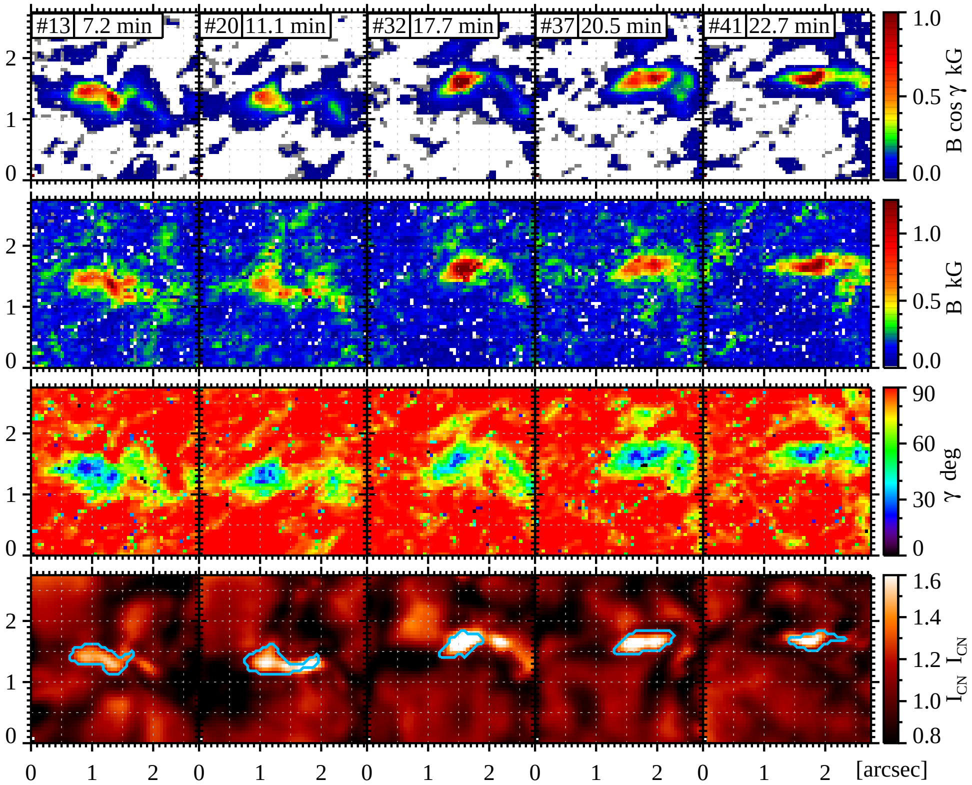

Figure 5.3: Evolution of a multi-cored magnetic structure (red box in Figure 5.1). First row: longitudinal magnetic field component, $B \cos \gamma$. Second row: magnetic field strength, B. Third row: magnetic field inclination, γ. Fourth row: CN band images. Frame numbers and elapsed time are given in the upper left corner of each top frame. Both axes are in arcsec.

remnants appear to leave the main merged core during the merging process itself. They follow an independent evolution (best seen in the CN maps) until the end of the time series through which both merge into a different (weaker) magnetic structure. Despite these recurrent fragmentation and coalescence processes, the magnetic cores keep sharing the same canopy over the whole time. These processes are analyzed in more detail in the following Section.

Since we have observed that CN BPs are good proxies of magnetic cores and this is also true for those seen in the G band (Kiselman et al. 2001), the above-described evolutionary behavior is consistent with the photometric observations of, e.g., Berger & Title (1996). In the light of our co-aligned spectropolarimetric observations we are in a position to assert that such BP groups, that keep together for periods much longer than a granule lifetime (up to 70 minute in Berger et al. 1998), can be members of the same magnetic structures.

5.6 Interaction with granular convection

Figure 5.4 indicates the different processes that take place during the evolution of the multi-cored magnetic structure due to its interaction with the local granular convection flows. From top to bottom, the rows show longitudinal magnetic field maps, CN intensity, LOS velocity, and continuum intensity maps. This figure is complemented by Animation 2, which is included in the electronic edition of Requerey et al. (2015). In the animation we also display the Ca II H intensity maps. As in Figure 5.3, the blue contours mark the periphery of the multi-cored magnetic structure. The new black contours have been created to follow the evolution of the individual magnetic cores and delineate a set of regions whose summed magnetic flux is constantly equal to 2.9×10^{17} Mx throughout the period of observation. These flux contours are constructed by starting from the most intense pixels in the longitudinal magnetic field map and then gradually expanding the contour by lowering the $B_{\rm long}$ for pixels included inside it. The black contours thus outline the magnetic cores. Finally, blue arrows show the horizontal velocity maps inferred through the LCT technique by correlating the displayed frames with the previous ones.

In Figure 5.5 we quantitatively analyze the evolution of the multi-cored magnetic structure shown in Figure 5.4. For this purpose, we manually track the magnetic cores in the longitudinal magnetic field maps. Figure 5.5 (a) displays the evolution of the area enclosed by our constant-flux region of 2.9×10^{17} Mx. This area is delimited by black contours in Figure 5.4. The other panels show the evolution of the LOS velocity (b), field strength (c), and CN intensity (d) for each of the magnetic cores. To increase the signal-to-noise ratio in the magnetic core physical parameters, we represent averages over 9 pixels around their $B_{\rm long}$ centroid. The red and green lines correspond to the leftmost and rightmost cores respectively, while a black line is drawn when the two cores merge into one. The vertical dotted lines corresponds to the end of the different phases described in the following Sections.

5.6.1 Intensification by granule compression

From frame 12 to 16, the leftmost magnetic core (red lines in Figure 5.5) stays at rest whereas the rightmost magnetic core is compressed between two granules (Figure 5.4 and Animation 2) . The upper granule (at coordinates [$1\farcs75$,$2''$] in frame 12) moves toward the magnetic core, while the lower granule (at coordinates [$1\farcs25$,$0\farcs25$]) expands. This compression process results in the intensification of the magnetic core. The field strength

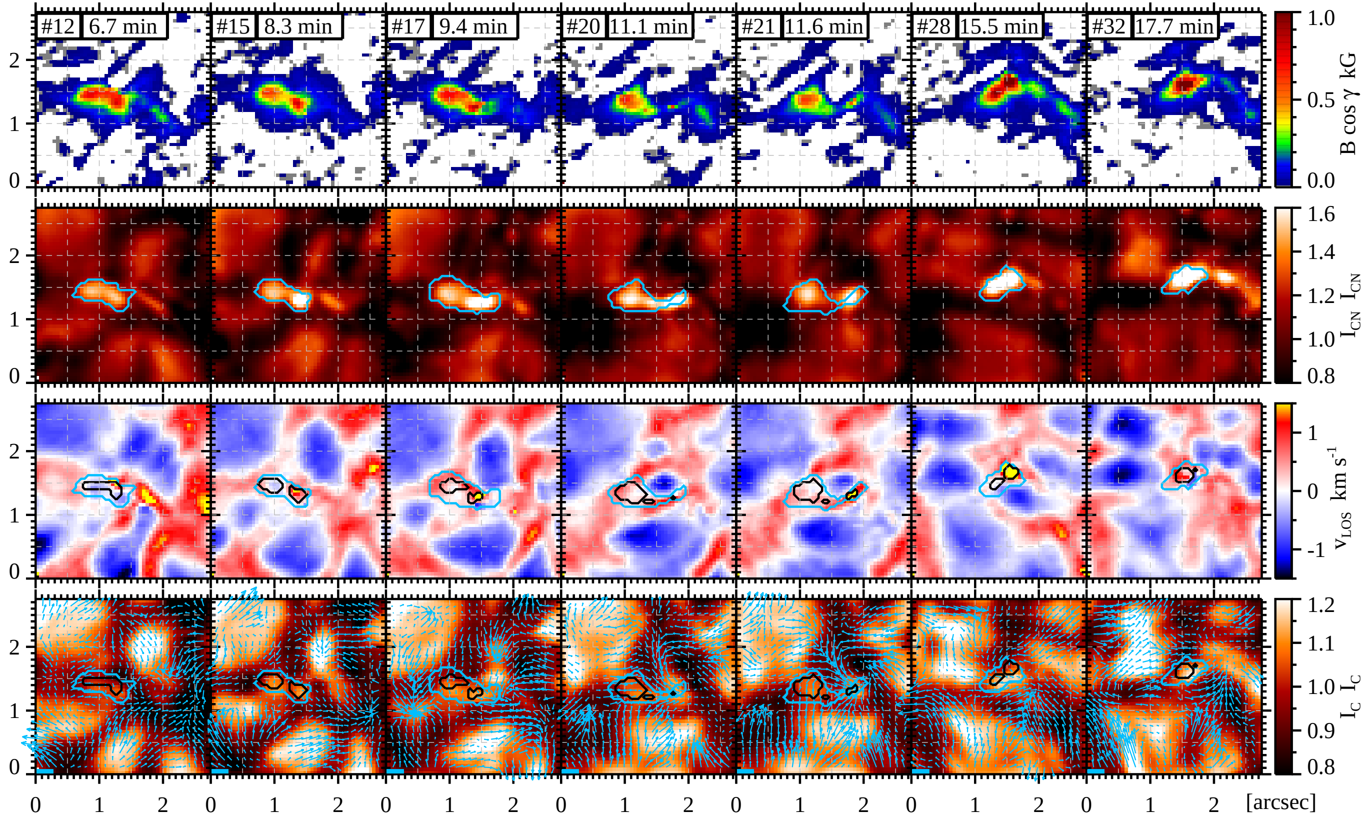
#12 6.7 min
#15 8.3 min
#17 9.4 min
#20 11.1 min
#21 11.6 min
#28 15.5 min
#32 17.7 min
B cos γ kG
1.0
0.5
0.0
I_{CN}
1.6
1.4
1.2
1.0
0.8
v_{LOS} km s^{-1}
1
0
-1
I_C
1.2
1.1
1.0
0.9
0.8
0
1
2
[arcsec]

Figure 5.4: (Previous page.) Closeup of the first three frames in Figure 5.3 with greater temporal resolution. First row: longitudinal magnetic field component, $B \cos \gamma$. Second row: CN images. Third row: LOS velocity v_{LOS}. Fourth row: continuum intensity. The total magnetic flux within all the black contours in a given image is constantly equal to 2.9×10^{17} Mx. Overplotted blue arrows in the bottom panels outline the horizontal flow field derived through the LCT technique by correlating the displayed frames with the previous ones. The length of the blue bar at coordinates $[0.''0,\ 0.''0]$ corresponds to $1.8\,\mathrm{km\,s^{-1}}$. Blue contours are the same as in Figure 5.3. This figure is also available within Animation 2 in the electronic edition of Requerey et al. (2015).

increases from about 800 G to about 1100 G (green line in Figure 5.5 (c)) as the CN intensity also rises. Meanwhile, the LOS velocity grows from nearly 0 to $1.1\,\mathrm{km\,s^{-1}}$ (average) with a peak velocity of up to $3\,\mathrm{km\,s^{-1}}$. This maximum downflow is reached at frame 16 within the rightmost core close to a small upflow feature that emerges at the edge of the magnetic structure. As soon as this small-scale downflow/upflow feature appears, a co-spatial BP is detected in the Ca II H images (see Animation 2).

Such a nearly simultaneous small-scale downward/upward velocity pattern was first observed within a magnetic element (Chapter 4) and, later, close to many BPs visible in the line core of Fe I 525.02 nm (Utz et al. 2014). In Chapter 4, this pattern was detected at the end of two consecutive magnetic field intensification processes. The isolated magnetic element was compressed by all surrounding granules, and both intensification processes led to a reduction in the area of the flux concentration and an enhancement of its field strength. In our new observations, however, this phase dose not contribute much to decreasing the area of the global magnetic structure (Figure 5.5 (a)). This is mainly due to the small size of the rightmost magnetic core compared to the entire area covered by magnetic flux.

5.6.2 Fragmentation

After the intensification phase the rightmost magnetic core and its related CN BP get elongated (frame 17 in Figure 5.4) as a consequence of the compression. The “squeezing” ends by fragmenting the magnetic core in two (frames 17-21). The squeezing is also well illustrated by the horizontal velocity arrows in the bottom panels of Figure 5.4. For simplicity, in Figure 5.5 we only show the evolution of the rightmost fragment, whose field strength and CN intensity drops abruptly (green line up to frame 23). The decrease of the field strength in the resulting fragments leads to the increase of the area enclosed in the contour of constant magnetic flux (5.5 (a)). Small variations in the average LOS velocity accompany this process.

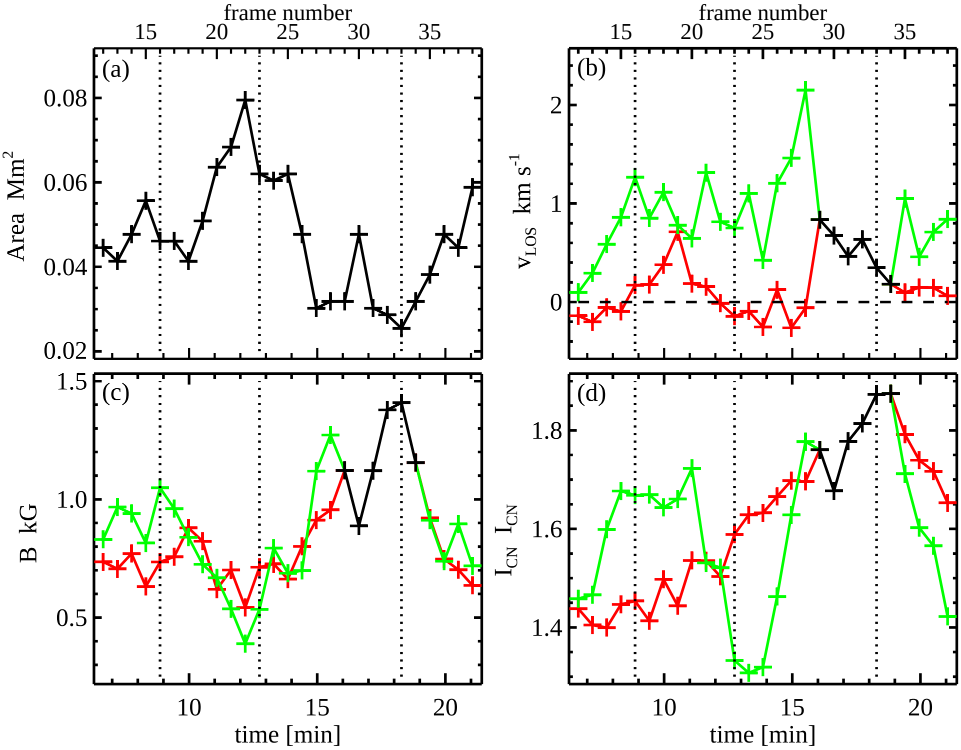

Figure 5.5: Evolution of relevant quantities with full temporal resolution, for frames 11-38. (a) The area within the black contour (enclosing a time-independent magnetic flux of 2.9×10^{17} Mx). The x-axis at the top of the panel marks the frame numbers. (b) LOS velocity. (c) Magnetic field strength. (d) CN intensity. The plots display values of the corresponding quantities averaged over nine pixels centered around the centroid of the magnetic cores in the longitudinal magnetic field maps. Red (green) lines stand for the leftmost (rightmost) magnetic core and the black line is used when a single magnetic core is observed.

5.6.3 Coalescence and further fragmentation

At the end of the fragmentation phase the upper granule fades away and the surrounding granules start to fill the "empty" space (see frame 21 to 32 in Animation 2) soon afterwards. In this way, the three magnetic cores are advected to the wide space left by the fading granule, and compressed by the surrounding granules until they merge into a single magnetic element (frame 32 in Figure 5.4). The advection of magnetic cores by the proper motions of the neighboring granules is also well illustrated by the horizontal velocity flow field. During this compression phase a strong downflow is detected within the rightmost magnetic core (frame 28) and a small upflow in its surroundings (frame 32). As soon as the downflow appears, a new co-spatial bright feature is detected in the Ca II H image (Animation 2). The almost co-temporal upflow that emerges at the periphery of the magnetic structure also appears co-spatial to the Ca II H BP.

The coalescence process takes place from frame 23 to 33 (Figure 5.5). Within these 5 minutes, the magnetic fields are concentrated and, because the flux is conserved, the area decreases while the field strength increases. The magnetic field reaches a strength of up to 1.4 kG, compared with the initial ∼600 G of each magnetic core. Simultaneously, the CN intensity is also enhanced nearly in phase with the field strength. The plasma within the leftmost core is approximately at rest on average while the LOS velocity increases from 1 to 2 km s^{-1} within the rightmost core. Note, however, that our 9-pixel average LOS velocity can be misleading. The apparent decrease in $v_{\rm LOS}$ for the coalesced structure results from the simultaneous presence of a downflow (in the inner core) and an upflow (at its periphery).

The evolution continues with a new fragmentation process. In a time interval of about 3 minutes, the magnetic element splits in two (see frame 37 in Figure 5.3 or Animation 2) and the different physical quantities are almost restored to their values prior to the coalescence phase (Figure 5.5).

5.7 Magnetic field oscillations

Driven by the local granular convective flows, the sequence of intensification, fragmentation and coalescence events described above occur all along the evolution of the multi-cored magnetic structure. This evolutionary behavior results in oscillations of its constant magnetic flux area (Figure 5.5 (a)). Similar magnetic field oscillations where first detected in four quiet-Sun magnetic patches by Martínez González et al. (2011) within IMaX data. They argued that the periods associated with this oscillatory pattern could be related with characteristic oscillation modes of flux tubes or, might correspond to the forcing by granular motions. Due to their compatibility with the granular lifetime and the fact that the oscillations can be strongly damped or amplified and their period abruptly modified, they favor the latter scenario.

Here, we wonder if the oscillations found by Martínez González et al. (2011) have also something to do with the evolution of our multi-cored magnetic structures. With the purpose of answering this question, in Figure 5.6 we display the time evolution of the longitudinal magnetic field for the four magnetic patches analyzed by them. We find that at least three of them (if not all four) are indeed multi-cored magnetic structures. The one displayed in the top row also shows hints that at some point it may be composed of at least two magnetic cores (see panels at 11.1 and 17.7 minute). However, this is not that evident as in the other three cases.

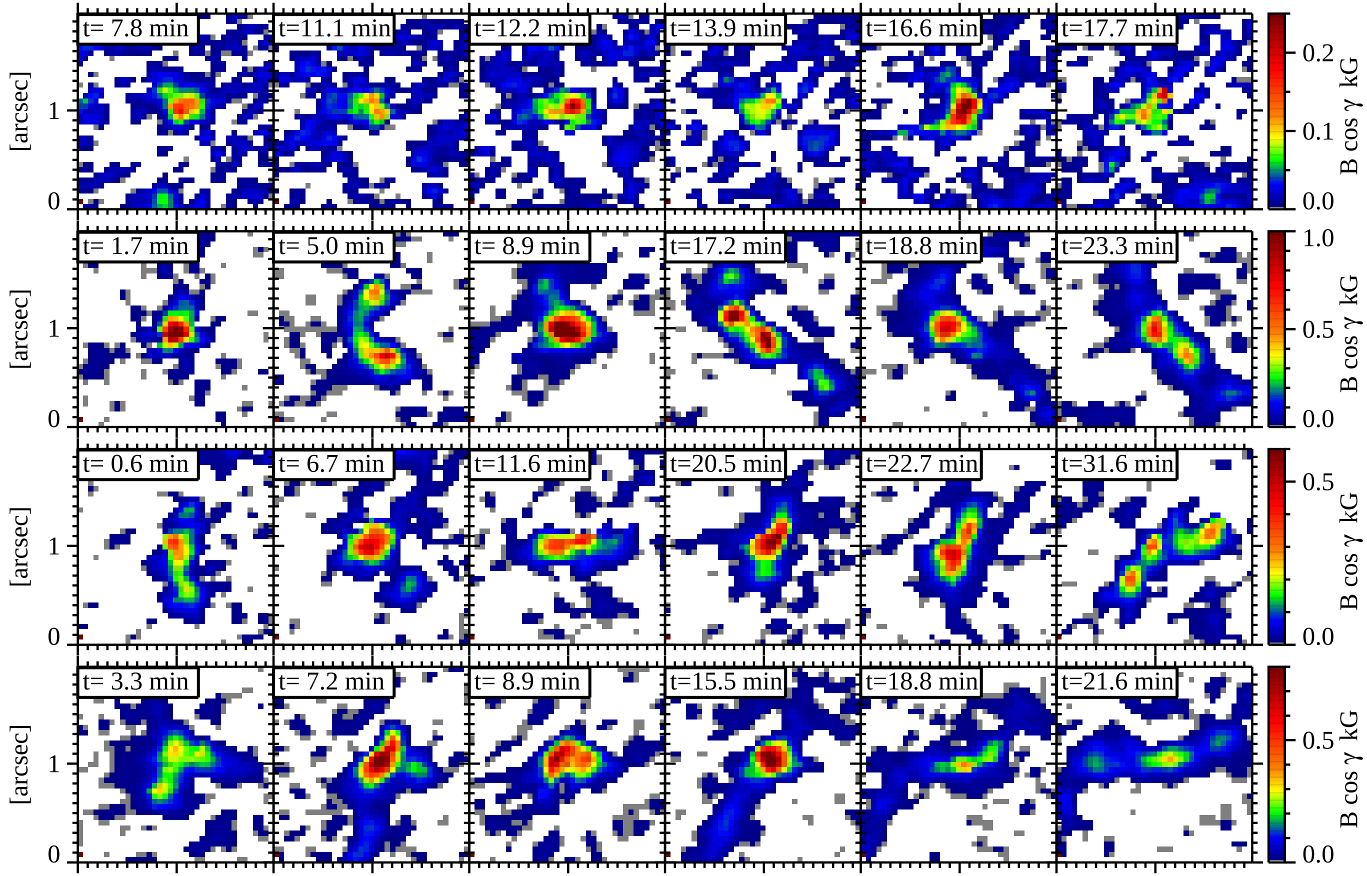

Figure 5.6: Evolution of the longitudinal magnetic field of the four magnetic structures analyzed by Martínez González et al. (2011). The structure at the top row is located within the blue solid square in Figure 5.1. The other tree features corresponds to other IMaX time series and consequently their location is not shown in Figure 5.1.

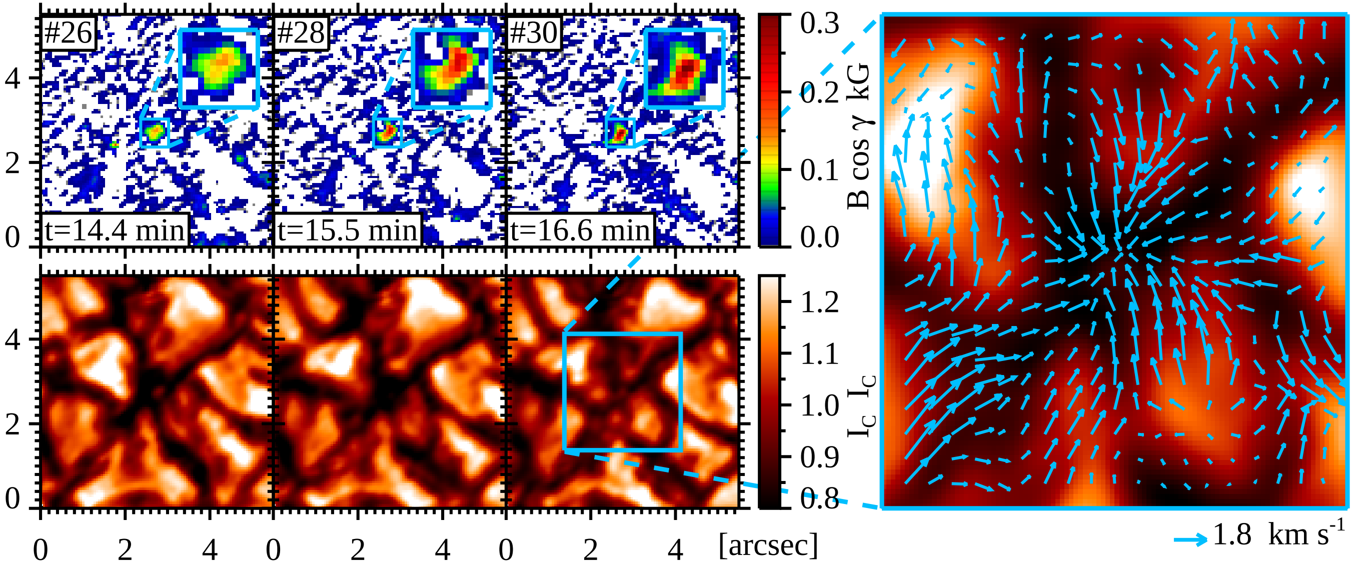

Figure 5.7: Closeup of one of the intensification phases of the magnetic structure in the top row of Figure 5.6. The structure is located within the blue dashed square in Figure 5.1. First row: longitudinal magnetic field. Second row: continuum intensity. The rightmost panel shows the horizontal velocity maps derived through the LCT technique averaged over the intensification phase. The length of the blue arrow at the lower right corner of the figure corresponds to 1.8 km s^{-1}.

According to our new analysis, the oscillations of the three multi-cored magnetic structures can be explained through the intensification, coalescence and fragmentation processes that their inner cores suffer when they are continuously buffeted by granular flows. The damping and amplification phenomenon of oscillations and the strong changes in their periods might be caused by the changes in the number of magnetic cores contained within the structure, and by the fact that some of the fragments fade into a more diffuse magnetic field below our observational threshold (see e.g., the evolution of the magnetic feature in the second row).

It seems evident that the oscillations in at least three of the four magnetic structures are compatible with the forcing by granular motions. However, it may still be possible that oscillatory modes are present in the evolution of the magnetic structure in the first row of Figure 5.6. In order to dispel these doubts we analyze the interaction of this feature with convection. With this purpose in mind we show one of the intensification events undergone by this feature in Figure 5.7. In the first panel, the magnetic element is located in a wide space left by granules. The magnetic structure become stronger as it is compressed between the granules. During this process the surrounding granules elongate in the direction of the magnetic feature, thus forming a characteristic daisy-like pattern first described by Muller et al. (1989). The compression process is well characterized by the horizontal velocity flows (rightmost panel in Figure 5.7), which point toward the magnetic feature near the center of the FOV. This shows that the oscillations correspond also in this case to the forcing by granular motions, as the magnetic feature is intensified at each of the recurrent granule compression phases.

5.8 Discussion and conclusions

We have presented direct observations of small-scale magnetic field dynamics in the quiet-Sun. This has been done with the accurate polarimetric measurements and high spatial resolution images obtained with the IMaX and SuFI instruments aboard the SUNRISE balloon-borne stratospheric mission.

The results reported about several vertical magnetic cores surrounded by a common, more horizontal magnetic structure suggest that we are witnessing a collection of flux concentrations in the lower photosphere that share a common canopy in the upper photospheric layers. In the photosphere, intensification, fragmentation and coalescence processes play an important role in the evolution of the individual magnetic elements. This evolution is consistent with that of their photometric counterparts (BPs) as described by Muller & Roudier (1992), Roudier et al. (1994) and Berger & Title (1996).

The fragmentation and merging episodes appear to be governed by the evolution of the local granular convection flows. Magnetic cores have been observed to fragment when they are "squeezed" or "compressed" by converging or expanding granules. The fragmentation of magnetic cores through the perturbation of surrounding granules may be evidence for the action of the interchange, or fluting, instability in magnetic elements. The susceptibility to the interchange instability is indeed an inherent property of flux tubes as first noticed by Parker (1975) and Piddington (1975). The fact that the magnetic fragments share a common canopy strongly supports the theoretical predictions of Bünte (1993). His idealized model contended that magnetic slabs are liable to fluting in a limited height range around $\tau_c = 1$, i.e., around the solar surface. Thus, a sheet-like magnetic structure fragments into tube-like filaments. Higher up in the atmosphere, however, the single magnetic tubes lose their individual identity as they expand with height and merge into a single, stable magnetic canopy. He also conjectured that the continuous advection of the tubes back to intergranular lanes by converging granular motions might prevent further dispersion through hydrodynamic drag.

We have also observed that soon after the splitting takes place, the resulting fragments are quickly regrouped again in intergranular lanes by the converging surrounding granules. Since the flux concentration cools the surrounding gas, it enhances the granular flows towards it (Deinzer et al. 1984). This effect keeps the multi-cored magnetic structure together during the entire 23 minute dataset. In the light of this spectropolarimetic picture, it is understandable that groups of BPs can persist for long times (up to 70 minute according to Berger et al. 1998) while being constantly buffeted by granules.

The quantitative analysis shows that the total magnetic flux of a typical multi-cored magnetic structure remains roughly constant during its evolution. We obtain this result as we are able to spatially resolve (at least partially) this magnetic structure. We are then enabled to relate the enhancement (decrease) of the CN BP brightness during the intensification and coalescence (fragmentation) phases with the increase (decrease) of the magnetic field strength and not with changes in the local filling factor as proposed by Viticchié et al. (2009). It is worth noting that in contrast to them, with the spatial resolution of the SUNRISE/IMaX data ($\sim 0.''15$), we can get rid of the filling factor (Lagg et al. 2010). This correlation between the brightness and the field strength supports the classical picture of magnetic element radiance by the hot-wall mechanism. Accordingly, the reduced gas pressure within the flux tubes locally depresses the optical depth unity level. The less opaque magnetic flux-tube interior then causes an excess of lateral inflow of radiation into their evacuated interiors (Spruit 1976; Deinzer et al. 1984), and as a consequence the magnetic elements appear brighter than their surroundings.

In addition, as a consequence of the flux conservation, the continuous intensification, coalescence and fragmentation of magnetic cores results in oscillations of the magnetic field strength and cross-section area of the entire magnetic feature. Such oscillations were first detected in four quiet-Sun magnetic patches by Martínez González et al. (2011). We have found that three of them are indeed multi-cored structures, while the fourth one may have sub-resolution structure. In all these features (and in other multi-cored magnetic structures) the compression by surrounding granules plays an important role in the intensification of the magnetic field. In Chapter 4 we already observed a large-amplitude variation in area and field strength within a magnetic element related to similar granule compression processes. However, due to the limited length of the observation only a single period was seen, and therefore we could not confirm that these variations were part of an oscillatory pattern.

The excitation of the oscillations is consistent with the forcing by granular motions. The pattern we observe corresponds to the evolution of magnetic flux concentrations, whose internal structure change as they are perturbed by granular flows. Through this interaction the magnetic structures are continuously being compressed, fragmented, or their different components regrouped and hence the magnetic fields are constantly being strengthened or weakened.

These magnetic field variations could explain the fact that brightness enhancements are observed at BPs when compressed by converging granules (Muller & Roudier 1992). They could also be the cause for the broad range of field strengths found at BPs by Beck et al. (2007b), p.165.

When the magnetic structure is compressed, kG field strengths are sometimes reached at the same time that strong photospheric downward motions are found within the magnetic cores. Such a correlation has been interpreted as a convective collapse by different authors (e.g., Nagata et al. 2008; Danilovic et al. 2010a). Our findings, then, suggest that convective collapse could be triggered by granular perturbations.

The highly dynamic nature of small-scale magnetic fields found here suggests the generation of waves that could propagate up through the solar atmosphere. This is supported by the chromospheric activity that we have detected during the intensification, coalescence and fragmentation processes related with photospheric downward and upward motions. Correlation between photospheric downflows and Ca II H brightenings has been explained in terms of the convective collapse process (Shimizu et al. 2008; Fischer et al. 2009), and as disk-center photospheric traces of type II spicules (Quintero Noda et al. 2014). We did not find, however, any previous mention in the literature of a relationship between Ca II H brightness and photospheric upflows as found here. In the chromosphere, high plasma velocities in the blue wing of Ca II IR line have been first found by Langangen et al. (2008) as the disk counterpart of type II spicules. Could the photospheric upflows that we observe here have something to do with those seen in the chromosphere? Further investigations using time series observations of comparable spatial resolution and polarimetric sensitivity at the photosphere, together with simultaneous spectroscopic information on the chromosphere, are to shed new light on these issues.

6

CONVECTIVELY DRIVEN SINKS AND MAGNETIC FIELDS IN THE QUIET SUN

We study the relation between mesogranular flows, convectively driven sinks and magnetic fields using high spatial resolution spectropolarimetric data acquired with the Imaging Magnetograph eXperiment on board SUNRISE. We obtain the horizontal velocity flow fields of two quiet-Sun regions ($31.2 \times 31.2\,\mathrm{Mm}^2$) via local correlation tracking. Mesogranular lanes and the central position of sinks are identified using using Lagrange tracers. We find 6.7×10^{-2} sinks per Mm^2 in the two observed regions. The sinks are located at the mesogranular vertices and turn out to be associated with (1) horizontal velocity flows converging to a central point and (2) long-lived downdrafts. The spatial distribution of magnetic fields in the quiet Sun is also examined. The strongest magnetic fields are preferentially located at sinks. We find that 40 % of the pixels with longitudinal component of the magnetic field higher than 500 G are located in the close neighborhood of sinks. In contrast, the small-scale magnetic loops detected by Martínez González et al. in the same two observed areas do not show any preferential distribution at mesogranular scales. The study of individual examples reveals that sinks can play an important role in the evolution of quiet-Sun magnetic features.

6.1 Introduction

Most quiet-Sun magnetic fields evolve on the solar surface driven by convective motions. The largest magnetic structures outline the boundaries of supergranular cells —the magnetic *network*. Inside the supergranular cells smaller magnetic flux concentrations of both polarities permeate the solar *internetwork*. They tend to concentrate in mesogranular lanes (Yelles

Chaouche et al. 2011) and a significant fraction of the magnetic flux emerges to the surface co-spatially with granules in the form of small-scale magnetic loops (Martínez González et al. 2007; Centeno et al. 2007; Martínez González & Bellot Rubio 2009; Martínez González et al. 2010; Danilovic et al. 2010b; Martínez González et al. 2012a).

Convection displays highly localized downdrafts where cold plasma returns to the solar interior (Spruit et al. 1990; Stein & Nordlund 1998; Nordlund et al. 2009). Due to conservation of the angular momentum, a vortex can be formed as the plasma approaches the downdraft (the *bathtub* effect, Nordlund 1985). In fact, small-scale vortex flows are ubiquitous in simulations of solar surface convection (e.g., Kitiashvili et al. 2011; Shelyag et al. 2011; Moll et al. 2011; Steiner & Rezaei 2012). The plasma can also drag magnetic fields toward the draining point, where they can be intensified up to kG values (Danilovic et al. 2010a; Kitiashvili et al. 2010). As a consequence, a large amount of vorticity can be generated through the interaction of plasma and magnetic fields in the intergranular juctions (Shelyag et al. 2011). Vertical vorticity is known to concentrate preferentially in negative divergence areas, i.e., downflow regions (Wang et al. 1995b; Pötzi & Brandt 2005, 2007). Vortex flows are observed at large scales (up to 20 Mm, Brandt et al. 1988; Attie et al. 2009) in supergranular junctions and at smaller scales ($\lesssim$0.5 Mm, Bonet et al. 2008, 2010; Vargas Domínguez et al. 2011) in granular ones. Small-scale whirlpools are also visible in the chromosphere (Wedemeyer-Böhm & Rouppe van der Voort 2009; Park et al. 2016) and their imprints have been identified in the transition region and low corona (Wedemeyer-Böhm et al. 2012). .

Vortex flows which harbor magnetic fields are rather abundant (Bonet et al. 2010). In particular, Balmaceda et al. (2010) showed evidence of small-scale magnetic concentrations being dragged toward the center of a convergence flow point. The same event was further studied by Vargas Domínguez et al. (2015), who found sudden downflows and intensification processes of the magnetic concentrations. Magnetic field enhancements preceded by strong downdrafts are generally understood in the context of *convective collapse* (Parker 1978; Webb & Roberts 1978; Spruit 1979). Manso Sainz et al. (2011) found that the trajectories of some small-scale loop footpoints describe a vortical motion suggesting that they may be engulfed by a downdraft. Finally, we observed in Chapter 4 a loop footpoint being advected and concentrated in a point-like sink together with other same-polarity weak magnetic patches. All these papers, and the previous knowledge that intergranular magnetic fields tend to concentrate near the intersections of multiple granules, strengthen the idea that localized downdrafts[1] are places where the concentration of magnetic fields is favored. In order to confirm such a relation, quantitative and statistical information is still required.

---

[1] We shall use the term sink throughout the Chapter as a synonym of these localized downdrafts.

The aim of this Chapter is to provide a quantitative basis for the association between convectively driven point-like sinks and small-scale magnetic fields in the quiet Sun. We use spectropolarimetric observations from the Imaging Magnetograph eXperiment (IMaX; Martínez Pillet et al. 2011a) on board the SUNRISE balloon-borne solar observatory (Solanki et al. 2010; Barthol et al. 2011; Berkefeld et al. 2011; Gandorfer et al. 2011). IMaX provides stable time series of both intensity and polarization filtergrams at high spatial resolution (~ 100 km), which makes it the most suitable data for our study. Using the same SUNRISE/IMaX data, Yelles Chaouche et al. (2011) clearly demonstrated that magnetic elements are preferentially located in mesogranular lanes and Bonet et al. (2010) observed a large number of magnetic features swirling in convectively driven vortex flows. In the latter work, they detected vortices from the horizontal velocities obtained through local correlation tracking (LCT) of magnetograms and other IMaX images. They found a mean duration of such vortices of about 8 minutes and several events appearing at the same location in the course of the time series. The recurrent events were also observed in the flow field maps when averaged over the entire data set. In the present Chapter we find that such long-lived sinks are located in mesogranular junctions and that they are places where the strongest magnetic fields tend to concentrate.

6.2 Observations

We use high-quality spectropolarimetric data obtained with IMaX on board the SUNRISE balloon-borne solar observatory. IMaX is a dual-beam imaging spectropolarimeter with full Stokes vector capabilities in the Fe I line at 525.02 nm (Landé factor $g = 3$). The line is sampled by a Fabry–Pérot interferometer at five wavelength positions taken at $\lambda = -8$, -4, $+4$, $+8$, and $+22.7$ pm from the line center. The polarization analysis is performed by two liquid crystal variable retarders and a beam splitter. The image sequences were recorded close to a disk center, quiet-Sun area on 2009, June 9. We analyze two different time series, namely, S_1, from 00:36:03 to 00:58:46 UT (22.7 minutes in length) and S_2, from 01:30:54 to 02:02:29 UT (32.1 minutes), with a cadence of 33.25 s, and a spatial sampling of 39.9 km.

The science images were reconstructed using phase diversity measurements (Gonsalves 1982; Paxman et al. 1996) as described by Martínez Pillet et al. (2011a). This procedure effectively reduces the IMaX field of view (FOV) down to about $43'' \times 43''$ (31.2×31.2 Mm^2). After reconstruction, the spatial resolution has been estimated to be $0.''15$–$0.''18$ and the noise level in each Stokes parameter is about $3 \times 10^{-3} I_c$ (I_c being the continuum intensity). We recover information of the vector magnetic field and line-of-sight (LOS) velocities through inversions of the full Stokes vector using the SIR code (Ruiz Cobo & Del Toro Iniesta 1992) as described in Section 3.2. Height independent values for the three components of the

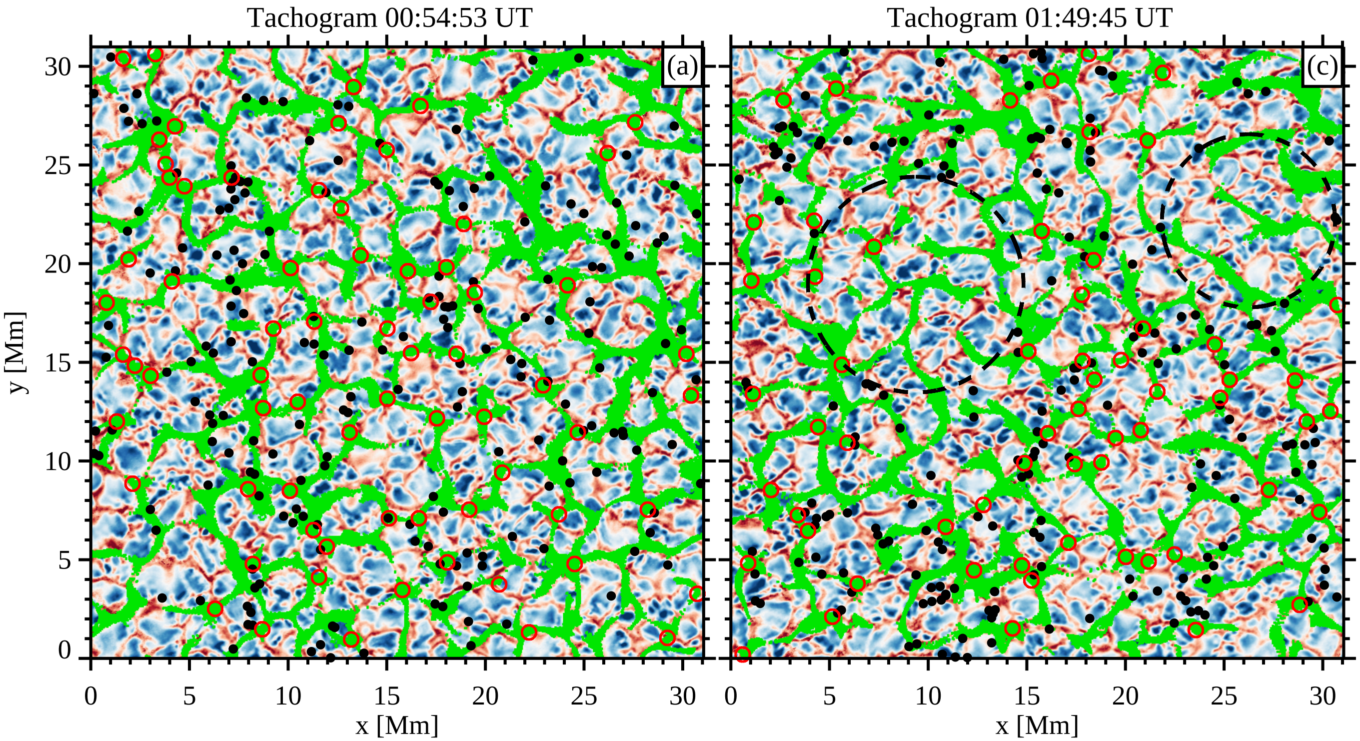
Tachogram 00:54:53 UT
Tachogram 01:49:45 UT
(a)
(c)
y [Mm]
x [Mm]
x [Mm]
0
5
10
15
20
25
30

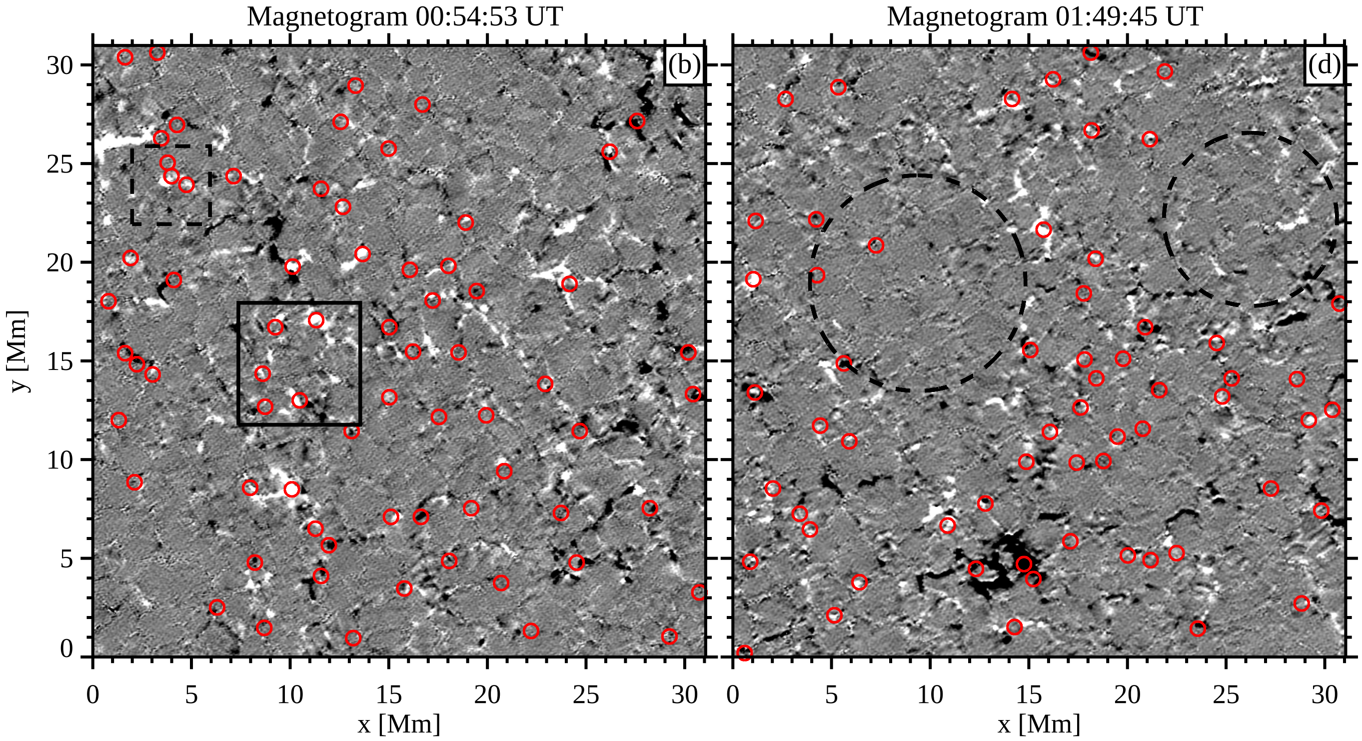
Magnetogram 00:54:53 UT
Magnetogram 01:49:45 UT
(b)
(d)
y [Mm]
x [Mm]
x [Mm]
0
5
10
15
20
25
30

Figure 6.1: (Previous page.) Top panels: green pixels represent locations with more than 2 corks pixel^{-1} at $t = 21.6$ minutes and its 1 pixel neighborhoods for time series S_1 (a) and S_2 (c), respectively. The background image is the LOS velocity at $t = 18.3$ minutes (saturated at $\pm 1.5\,\mathrm{km\,s^{-1}}$), where red and blue regions correspond to downflow and upflow areas, respectively. Black filled circles show the average position (between both footpoints) of the small-scale loops detected by Martínez González et al. (2012a). Bottom panels: the longitudinal component of the magnetic field, $B\cos\gamma$, at $t = 18.3$ minutes (saturated at ± 50 G) for the time series S_1 (b) and S_2 (d), respectively. Red circles (with a radius of 9 pixel ~ 360 km) represent the positions of the 131 sinks. The two areas delineated by the dashed circles mark two *dead calm* regions found by Martínez González et al. (2012a). The black dashed box represents the region analyzed in Chapter 4. The black solid rectangle, with a FOV of $6.2 \times 6.2\,\mathrm{Mm}^2$, illustrates the area used in Figure 6.5.

magnetic field and LOS velocity are assumed. From the magnetic field strength B and the inclination γ we derive the longitudinal component of the magnetic field (hereafter referred to as the longitudinal magnetogram) $B_{\mathrm{long}} = B\cos\gamma$.

6.3 Convectively driven sinks

6.3.1 Identification of mesolanes

Mesogranulation is a horizontal cellular flow pattern revealed through the LCT technique when applied to intensity images of the solar granulation (November et al. 1981; Simon et al. 1988; Title et al. 1989; Brandt et al. 1991; Muller et al. 1992; Roudier et al. 1998; Yelles Chaouche et al. 2011). Here we search for this pattern in the continuum intensity filtergrams of the two data sets. We use a common time coverage for both time series, namely, the total duration of series S_1 (the shortest one), so that we analyze only the first 42 snapshots of series S_2. This criterion will allow us to equally define inter-mesogranular lanes (called here mesolanes for short) in both time series. We apply a p-mode subsonic filter (Title et al. 1989) to remove the 5-min solar oscillations. This process degrades the first and the last frames, which are removed from our time series. The final data sets last, therefore, 21.6 minutes. We employ the LCT technique (November & Simon 1988) as implemented by Molowny-Horas & Yi (1994) to obtain the mean horizontal velocity field averaged over the duration of the data sets. This technique correlates small local windows in consecutive images to find the best-match displacement. The tracking window is defined by a Gaussian function with a FWHM = 600 km. After measuring the horizontal velocity vector $\mathbf{v} = \boldsymbol{v}_x + \boldsymbol{v}_y$, we also compute the flow divergence $\nabla \boldsymbol{v} = \frac{\partial v_x}{\partial x} + \frac{\partial v_y}{\partial y}$ and vertical vorticity $(\nabla \times \boldsymbol{v})_z = \frac{\partial v_y}{\partial x} - \frac{\partial v_x}{\partial y}$.

We outline the location of mesolanes by using Lagrange tracers (*corks*). Employing the mean horizontal velocity field, we track the evolution of each individual cork as described in

Yi (1992). Initially, a cork is located at each pixel of the image. Then the nearest neighbor velocity vector is used to "move" the corks. The trajectories are integrated in time assuming a time step of 33.25 s. For convenience, this value has been chosen to be the same as the cadence of the time series, but any other value could also be chosen. With this choice the mesogranular pattern is clearly visible after 21.6 minutes (i.e., 39 time steps), when most of the corks have already converged to mesolanes. The thickness and number of mesolanes depends significantly on the length of time that the corks are allowed to collect. After 21.6 minutes we find a good compromise between the smallest thickness and maximum number of mesolanes. At that time step we count the number of corks at each pixel to obtain the cork density function, ρ_{cork} (Yelles Chaouche et al. 2011), and we define the mesolanes as those locations where $\rho_{cork} \geq 2$ plus 1-pixel wide neighborhoods. These areas are marked in Figure 6.1 (a) and (c) through green pixels overlaid over the LOS velocity maps (tachograms) at $t = 18.3$ minutes for time series S_1 and S_2, respectively. These green regions clearly delineate a fully developed network of mesogranular cells with a size of 5-10 Mm (November et al. 1981).

6.3.2 Identification of converging flows

The mesogranular pattern is visible after only 21.6 minutes. However, if the corks are tracked for even longer, they finally end up (after some 5 hours[2]) in well localized points, in places where the horizontal velocity vectors converge on a central point. We obtain therefore the central positions of persistent *converging flows*, which appear in the mean flow corresponding to the full time series. We identify a total of 131 converging horizontal flows in the two observed regions. Taking into account the spatial area covered by each FOV, we get a density of 6.7×10^{-2} converging flows per Mm^2.

6.3.3 Classification of converging flows

In previous studies, small whirlpools were first detected as swirling motions of bright points (Bonet et al. 2008). Later they were identified from LCT horizontal velocities of magnetograms (Bonet et al. 2010) and G-band filtergrams (Vargas Domínguez et al. 2011). In the same way as done here, Vargas Domínguez et al. (2011) applied LCT to the whole FOV and duration of two G-band time series (20 minutes each) acquired with the Swedish 1-m solar telescope. By visual inspection of the horizontal flow-field maps, they identified individual vortices as those locations where the horizontal velocity vectors converge to a central point

---

[2] Notice that the extension of the cork movie has nothing to do with the length of the observations. The former has been computed by tracking cork trajectories through the mean horizontal velocity field as described in Section 6.3.1.

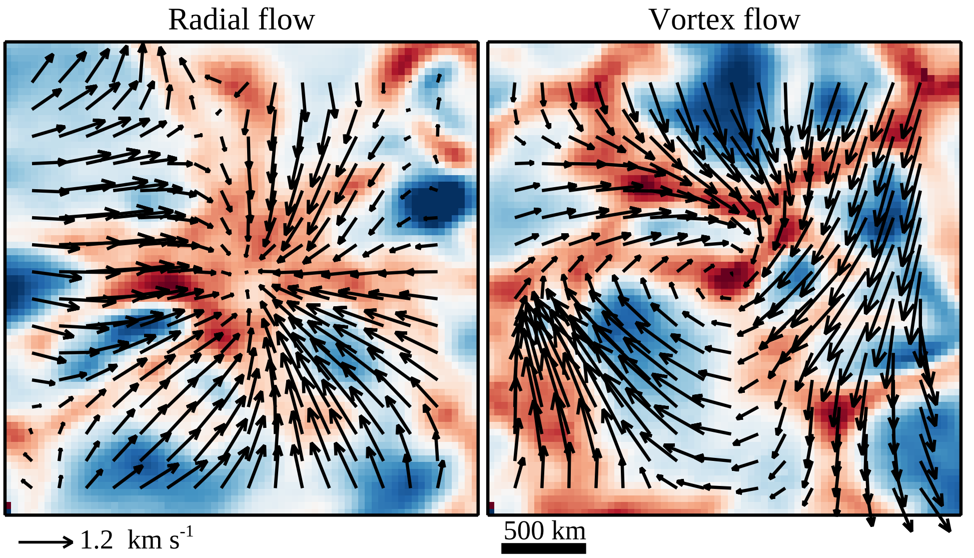

Figure 6.2: Two examples of converging flows detected in the IMaX data. The background images represent the LOS velocity at $t = 18.3$ minutes (saturated at $\pm 1.8\,\mathrm{km\,s^{-1}}$). Red and blue regions corresponds to downflow and upflow areas, respectively. The black arrows represent the horizontal velocity vectors obtained from LCT. The left panel shows an example of what we name a *radial flow* where velocity vectors point radially towards the center of the image. The right panel displays a *vortex flow* where the velocity vectors exhibit a swirling motion with a clockwise sense of rotation.

and form a swirl. They found these regions to be coincident with the final destination of corks. However they detected many other places where the corks got accumulated without any apparent swirling motion.

Here we inspect both the horizontal flow maps and the cork movies to analyze all the detected convergence centers. We realize that the corks follow different trajectories on their way to being engulfed by the converging flows. Some converge radially while other trace a spiral path as they fall into the inflow centers. In Figure 6.2 black arrows display the distribution of horizontal velocities for examples of two types of converging flows. In the left panel, the vectors point radially towards the center of the image, while in the right panel, they display a swirl. We shall hereafter refer to them as *radial flows* and *vortex flows*, respectively. We classify all the converging flows into these two categories by visual inspection. They are labeled as vortex flows when a sense of rotation can be ascribed to them from both cork movies and horizontal flow maps. On the contrary, they are designated as radial flows.

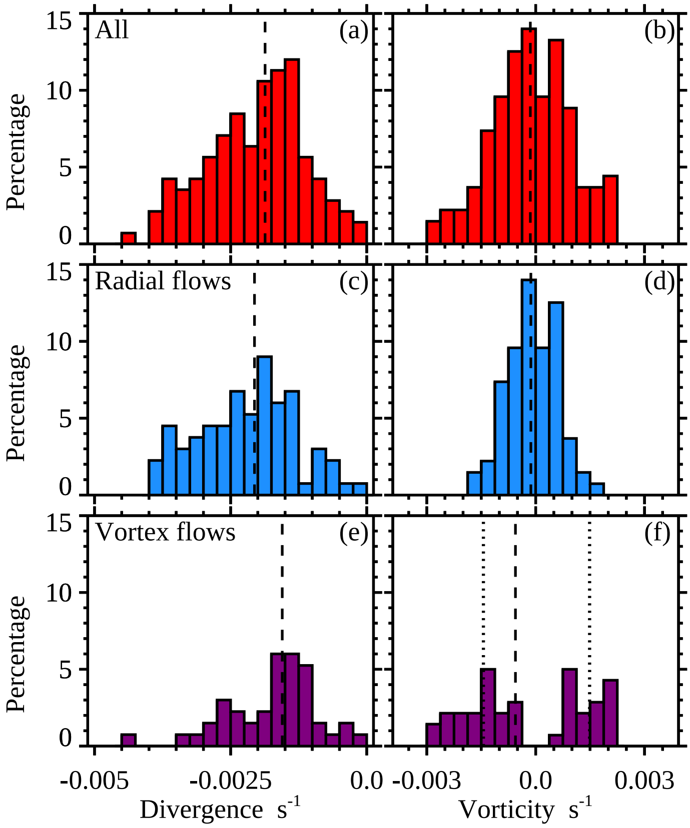

Figure 6.3: Histograms of divergence (a, c, and e) and vertical vorticity (b, d, and f) obtained from LCT proper motions at the convergence centers. Top panels are for all the 131 converging flows, middle panels are for the 85 radial flows, and bottom panels are for the 46 vortex flows. The vertical dashed lines indicate the median values of the distributions. In panel (f) the left and right vertical dotted lines mark the median value of the clockwise and counterclockwise vortices, respectively. We use a bin size of 2.5×10^{-4} s^{-1} and 3.75×10^{-4} s^{-1} for divergence and vertical vorticity, respectively.

6.3.4 Statistics of converging flows

We detect 46 vortex flows (35 % of the total sample of converging flows) and 85 radial flows. These result in densities of 2.4×10^{-2} vortex flows per Mm^2 and 4.4×10^{-2} radial flows per Mm^2, respectively. Our values for vortices is comparable to the number obtained by Vargas Domínguez et al. (2011) of 2.8–3.1 $\times 10^{-3}$ vortices per Mm^2.

In Figure 6.3 we display histograms of the divergence (left panels) and the vertical vorticity (right panels) at the convergence centers. By construction, all the converging flows (panel a) are located in negative divergence areas with a median value of -1.9×10^{-3} s^{-1}.

The divergence distribution is very similar for both vortex flows (panel e) and radial flows (panel c) with a 25 % smaller median value for the former, suggesting that vortex sinks are (25 %) less vigorous than uniform ones. Not surprisingly, the distribution of the vertical vorticity is completely different, however. Panel (d) shows that most of the radial flows have very low vorticity, whereas the negative and positive humps in panel (f) are produced by the distribution of whirls with clockwise and counterclockwise sense of rotation, respectively.[3] Both clockwise and counterclockwise vortices have a median absolute vertical vorticity of $1.5 \times 10^{-3}\,\mathrm{s}^{-1}$. We find a slightly larger number of clockwise (54 %) than counterclockwise motions (46 %), but the difference is not significant in view of the number of studied events.

6.3.5 LOS velocities in converging flows

If the computed horizontal flows are really describing true mass motions, then the horizontal proper motions should be related to vertical velocities. In particular, positive and negative divergences (i.e., mesogranules and mesolanes) must be correlated with upflows and downflows, respectively. Equivalently, converging flows should be coincident with downdrafts if they are indeed related to localized sinks.

In previous works (Bonet et al. 2008, 2010; Vargas Domínguez et al. 2011), the authors assumed without further examination that converging flows are locations of sinking gas. Here, we use the capabilities of IMaX to determine the LOS velocities at these locations. For this purpose, we build a binary mask by assuming that the spatial size of a converging flow is given by a 6 pixel (∼ 240 km) radius circle plus a 3 pixel wide annulus neighborhood. This 240 km radius corresponds to the mean radius found for converging flows by Vargas Domínguez et al. (2011). In addition, we divide the FOV into mesogranules and mesolanes. The former are defined as those areas in the FOV that are not covered by the latter (defined in Section 6.3.1). We then compare the histograms of the LOS velocities inferred from the SIR inversions at mesogranules, mesolanes and converging flows with that for the whole FOV.

The position of mesolanes and converging flows are influenced by the LCT average and therefore their comparison with each individual LOS velocity map of the time series is not straightforward. In a first instance, we compare them with the mean LOS velocities (averaged over the duration of the time series) at both observed regions (S_1+S_2). The resulting histograms are shown in Figure 6.4 (a). Different line colors indicate different locations, namely, red for converging flows, blue for mesogranules, green for mesolanes, and black for the whole FOV. The corresponding vertical dashed lines indicate the median values of each

---

[3] Since our classification is visual there is no clear threshold in vertical vorticity that separates vortex flows from radial flows.

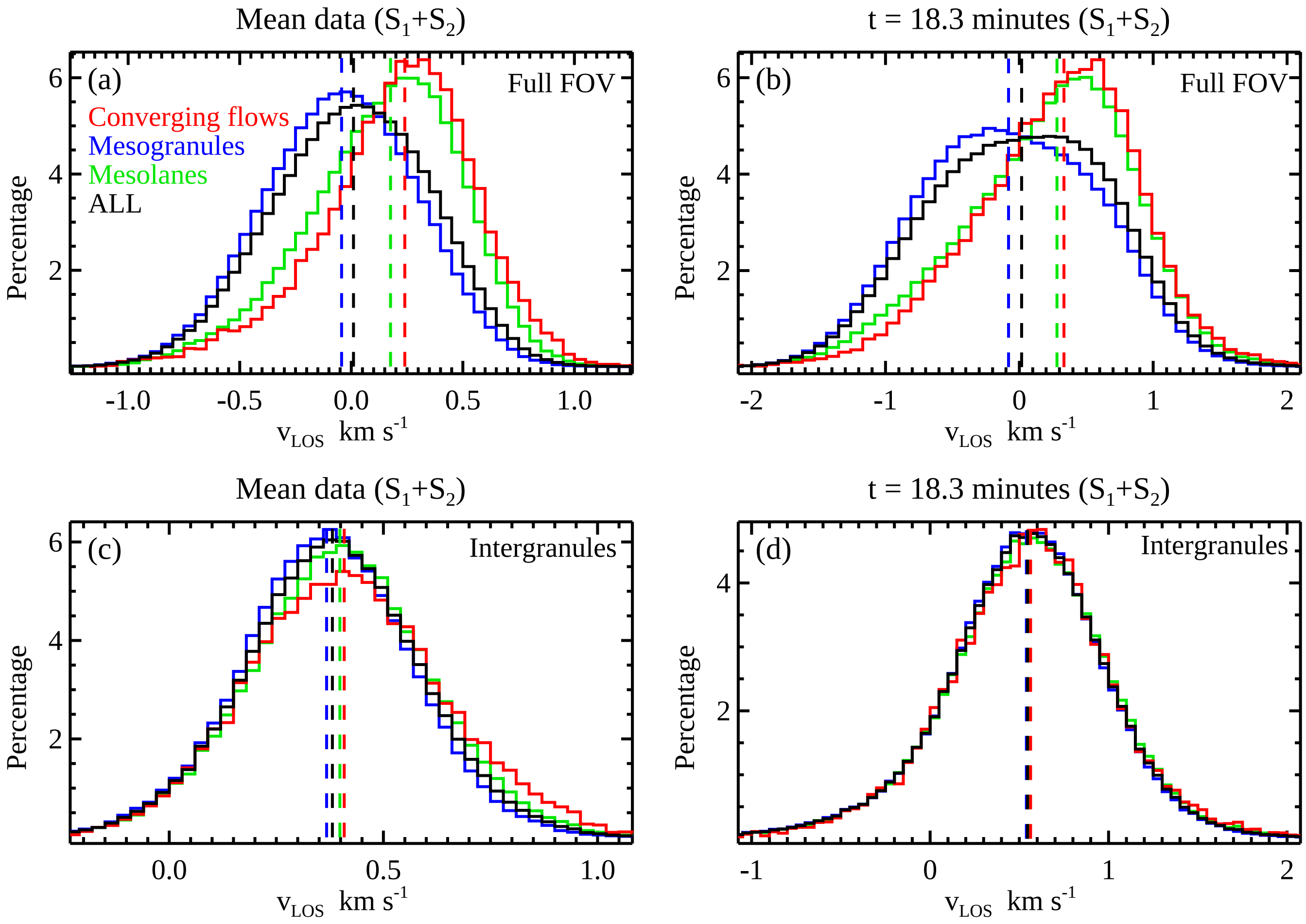
Mean data (S_1+S_2)
t = 18.3 minutes (S_1+S_2)
(a)
(b)
(c)
(d)
Full FOV
Intergranules
Converging flows
Mesogranules
Mesolanes
ALL
Percentage
v_{LOS} km s^{-1}
6
4
2
-1.0
-0.5
0.0
0.5
1.0
-2
-1
0
1
2

Figure 6.4: (Previous page.) Histograms of the LOS velocity for combined values within both observed areas (S_1+S_2). The left-panels plot mean values over the time series, whereas the right ones show values within a single snapshots at $t = 18.3$ minutes after the start of the time series. The upper-panels display values within the whole FOV, while the lower ones only account for values within intergranules. Solid lines stand for all pixels (black), converging flows (red), mesolanes (green), and mesogranules (blue), respectively. These regions are defined in the text. The corresponding vertical dashed lines indicate the median values of the distributions.

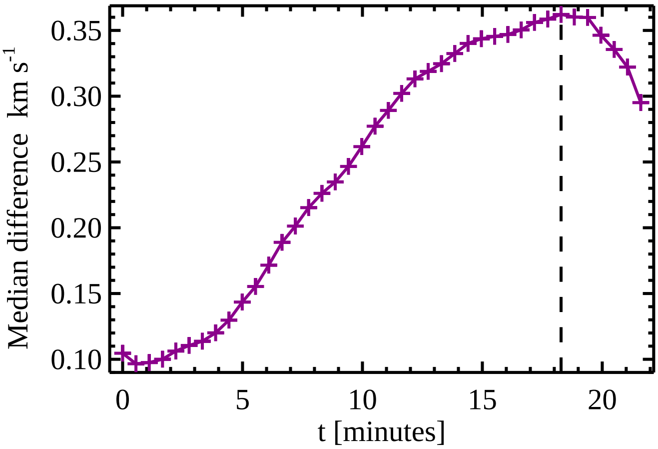

Figure 6.5: Differences between the LOS velocity median values at mesolanes and mesogranules over the duration of the time series. The vertical dashed line indicates the moment ($t = 18.3$ minutes) where the difference is largest.

distribution. Mesogranules are blueshifted and mesolanes redshifted with median values of -0.05 and 0.17 km s^{-1}, respectively. The redshift at convergence areas (red line) is even larger than in mesolanes, with a median value of 0.24 km s^{-1}. On average, mesogranules appear associated with upflows while mesolanes and converging flows are mostly located at downflows.

If we do the same for individual snapshots of the time series, we find that the correlation between mesolanes and downflows is highest at $t = 18.3$ minutes after the start of the time series. This is shown in Figure 6.5 where we display the differences between the median LOS velocity values at mesolanes and mesogranules over the time series. The vertical dashed line indicates the instant where the difference is largest. The corresponding histograms at $t = 18.3$ minutes are shown in Figure 6.4 (b). The results are similar to those obtained in Figure 6.4 (a). In this case, mesogranules (blue line), mesolanes (green line) and converging flows (red line) are characterized by median velocities of -0.1, 0.27, and 0.33 km s^{-1}, respectively. Figure 6.2 shows two representative examples of converging flows associated with downflows.

All the above distributions suggest that both mesolanes and converging flows are preferentially located at downdrafts, i.e., intergranular areas. Now we wonder whether these particular intergranular lanes are also places with stronger downflows than normal intergranules. To answer this question, in Figure 6.4 (c) and (d) we display the distributions of the same quantities as in Figure 6.4 (a) and (b), respectively, but considering only pixels coinciding with intergranular lanes. The separation between granular and intergranular regions has been performed using a threshold of $0.95\,I_{\rm c}$ in the corresponding continuum intensity images. The histograms at $t = 18.3$ minutes (Figure 6.4 d) are almost identical at all different locations, meaning that in a given moment intergranular lanes do not show particularly strong downflows within mesolanes or in converging flows. On the other hand, the distributions of the temporal mean LOS velocity values (Figure 6.4 c) show slight differences. In particular, mesolanes, and converging flows display larger mean downflow velocities than mesogranules. These slight differences suggest that mesolanes and converging flows are associated with persistent downflow areas.

In summary, we can say that mesolanes and in particular converging flows are (1) preferentially located within intergranular lanes and (2) associated with long-lived downdrafts. Therefore, we have shown that converging flows are indeed locations of sinking gas and we shall hereafter refer to them as *convectively driven sinks*.

At this point, we examine the question of whether mass is conserved at sinks. For that to occur, the lateral influx of mass over a scale height H should be equal to the vertical mass flux. Approximating the sink geometry by that of a circular cylinder of radius R and height H, mass conservation thus requires

$$2\pi R H \rho v_R \approx \pi R^2 \rho v_z. \tag{6.1}$$

To evaluate the lateral and vertical mass fluxes we need the radial velocity at the edge of the sink, v_R, and the vertical velocity, v_z. Assuming rotational invariance, the flow divergence can be expressed as $\nabla \boldsymbol{v} = \frac{1}{r}\frac{d(r v_r)}{dr}$ in cylindrical coordinates. Taking $v_r = \frac{r}{R} v_R$ yields $v_R = \frac{R \nabla \boldsymbol{v}}{2}$. With $R = 240\,\mathrm{km}$ and $\nabla \boldsymbol{v} = 1.9 \times 10^{-3}\,\mathrm{s}^{-1}$ (see Section 6.3.4), we obtain $v_R = 0.23\,\mathrm{km\,s^{-1}}$. The influx of mass is then $2\pi R H \rho v_R = 5.2 \times 10^{19}\,\rho\ [\mathrm{g\,s^{-1}}]$ over a density scale height of 150 km (e.g., Gingerich et al. 1971). On the other hand, taking $v_z = 0.33\,\mathrm{km\,s^{-1}}$ yields a vertical mass flux $\pi R^2 \rho v_z = 6 \times 10^{19}\,\rho\ [\mathrm{g\,s^{-1}}]$, which is in good agreement with the lateral mass influx. Thus, we conclude that mass is approximately conserved in sinks.

6.3.6 Spatial distribution of sinks

In Figure 6.1 we show the distribution of sinks (red circles) overlaid on the tachograms and longitudinal magnetograms of the two observed areas at $t = 18.3$ minutes. Green pixels in the tachograms represent the distribution of corks delineating the mesolanes. The sinks show a mesogranular distribution as most of them are located at the junctions of multiple mesogranular lanes. However, their spatial distribution is not completely uniform and there are some extended areas lacking detected sinks. There are two particularly prominent regions in time series S_2 (Figures 6.1 c and d). Interestingly they are coincident with the *dead calm* areas found by Martínez González et al. (2012a). Such areas are characterized by very low magnetic flux and a lack of small-scale magnetic loops. In Figures 6.1 (c) and (d) the dashed circles mark the two most prominent dead calm regions found by Martínez González et al. (2012a). These two regions contain several mesogranules within them but only a single sink is observed in the largest void. Visual inspection of the sinks in the longitudinal magnetograms (Figures 6.1 b and d) already reveals that many sinks harbor magnetic fields. This connection between magnetic fields and sinks gets even more evident if one looks at the evolution of magnetic elements. As we will describe in the following Section, magnetic structures are seen to be affected by convectively driven sinks.

6.4 The evolution of magnetic features driven by convective motions

This Section shows examples of three distinct processes that affect the evolution of quiet-Sun magnetic features: coalescence, cancellation and fragmentation. The statistics of such processes in the SUNRISE/IMaX data set has been studied in detail by Anusha et al. (2016). Here we show that these evolutionary processes of magnetic elements are seen to be driven by convective motions. In particular, coalescence and cancellation of magnetic structures are commonly observed at the sinks. Generally, fragmentation also takes place at sinks. At these locations, however, the resulting fragments are not usually completely detached from each other. Rather, the converging flows tends to merge them again into a single magnetic element. This phenomenon has already been described in Chapter 5: multi-cored magnetic structures are seen to live as a single entity for long periods; the individual cores merge and split. Our examples of fragmentation see Section 6.4.3 are taken from such multi-cored structures. Outside sinks, the complete splitting of magnetic elements is widely observed when the features are "squeezed" between two converging granules. Note that only illustrative examples are presented and discussed here, whose relevance for processes taking place in other magnetic features will need to be investigated on the basis of a much larger sample.

6.4.1 Coalescence

Figure 6.6 shows a coalescence process with a selection of three longitudinal magnetograms (upper row) and co-aligned CN-band filtergrams (bottom row). The CN-band filtergrams have been acquired with the Sunrise Filter Imager (SuFI; Gandorfer et al. 2011) and have been properly aligned with IMaX images as described in Chapter 5. The rightmost panel displays the horizontal velocity vectors obtained through the LCT technique averaged over the whole time series of 21.6 minutes (see Section 6.3). The background image shows the mean tachogram averaged over the duration of the time series.

The velocity map reveals a sink as the flows converge towards the center of the image where a downflow is present. In the first magnetogram two weak same-polarity magnetic patches are seen. As time goes by the patches move towards the convergence center where they merge into a single more intense magnetic element. During this coalescence process the longitudinal magnetic field increases from 100 G to about 200 G and a bright point (BP) is also formed as seen in the CN-band filtergrams. Contrary to the standard flux-tube theory (Spruit 1976), we find CN-band BPs related to magnetic elements with fields weaker than 1 kG (see also Section 6.4.3). Based on a comparison between the same Sunrise observations and MHD simulations, Riethmüller et al. (2014) concluded that all magnetic BPs are indeed associated with kG fields providing that the magnetic elements are spatially unresolved at the resolution of Sunrise/IMaX. However, from a simultaneous inversion of near infrared and visible spectral lines with a free magnetic filling factor, Beck et al. (2007a) found that the field strength of G-band BPs has a flat distribution that range from 500 G to 1500 G.

6.4.2 Cancellation

Figure 6.7 shows the temporal sequence of a partial cancellation process. The bottom row displays the line-core intensity instead of a CN-band filtergram as the event is located outside the FOV of SuFI. The line-core intensity has been determined by fitting the observed IMaX Stokes I profiles at the sampled spectral positions by a Gaussian (see Chapter 5). In the first frame, two diffuse opposite-polarity structures are observed. These structures are concentrated by the horizontal converging flows shown in the velocity map, thus forming two intense magnetic elements that interact with each other (see second frame). At this point, the positive and negative patches have magnetic fluxes of $+6.5 \times 10^{17}$ Mx and -9×10^{17} Mx, respectively. The positive polarity feature survives this interaction intact,

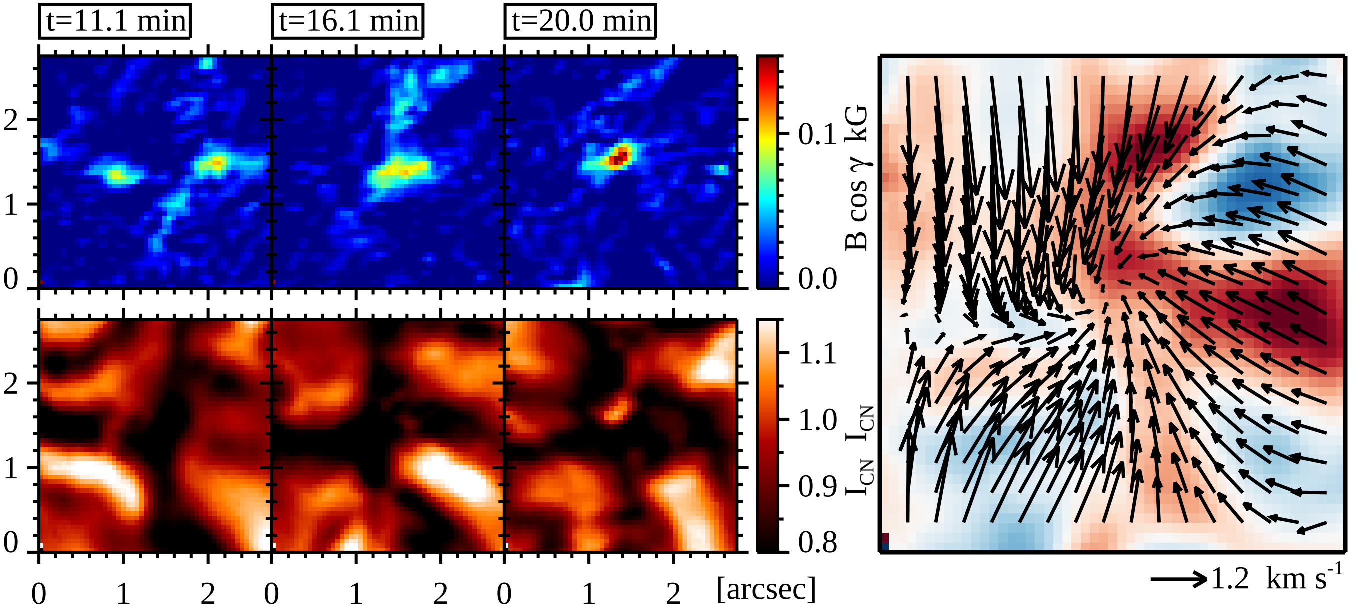

Figure 6.6: Temporal sequence of a coalescence process. Upper row: IMaX Fe I 525.02 nm longitudinal magnetic field. Lower row: SuFI images in the CN bandhead, centered at 388 nm with FWHM ≈ 0.8 nm. The rightmost panel shows the horizontal velocity maps (black arrows) derived through the LCT technique averaged over the whole time series of 21.6 minutes. The background image shows the mean tachogram averaged over the whole time series and saturated at ± 0.8 km s^{-1}. The black arrows display the horizontal velocity vectors. The length of the black arrow below the lower right corner of the figure corresponds to 1.2 km s^{-1}.

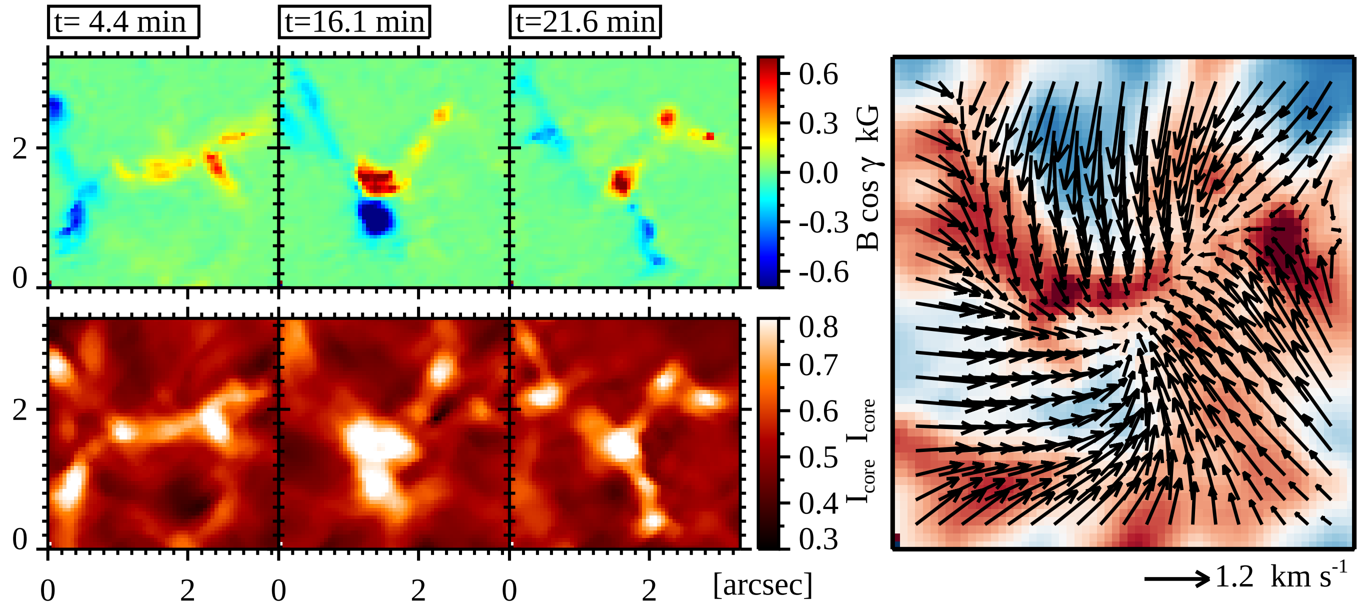

Figure 6.7: Same as Figure 6.6, during a partial cancellation process. Here the lower row shows the line-core intensity of the IMaX Fe I line at 525.02 nm in units of the continuum intensity. Please also note the different color scale in the upper row of images.

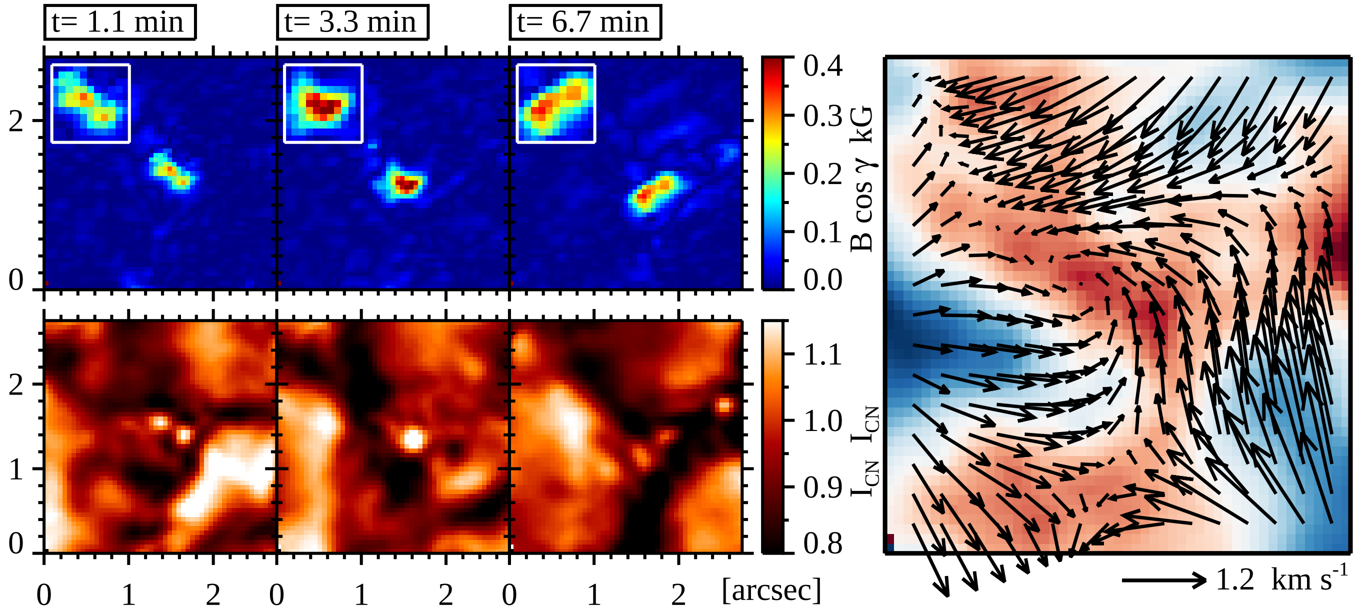

Figure 6.8: Same as Figure 6.6, during the evolution of a multi-cored magnetic structure. White boxes in the upper row display a zoom of the magnetic structure.

although with a greatly reduced magnetic flux of $+3.5 \times 10^{17}$ Mx, while the negative one gets more diffuse and decreases its magnetic flux down to -2.5×10^{17} Mx.

6.4.3 Fragmentation and merging in a multi-cored magnetic structure

Figure 6.8 shows the evolution of a small magnetic feature. The magnetic structure appears located within a vortex flow as indicated by the swirl displayed in the horizontal velocity map. In the first image the magnetic feature contains two cores with longitudinal magnetic field of 300 G each. Although these cores are likely spatially unresolved, the co-aligned CN-band image confirms that they are indeed separate as they appear associated with each CN bright point. This fact testifies to the outstanding quality of the SUNRISE/IMaX spectropolarimetric capabilities. The time sequence shows that the inner cores, and so the related BPs, merge to form a more intense magnetic element, which reaches up to 600 G. The coalescence process of magnetic cores is probably driven by the effect of the sink. Soon afterwards, however, the magnetic feature splits again into two weaker components. The evolution of such multi-cored magnetic structures has been studied in detail in Chapter 5. The continuous merging and splitting processes of the inner cores is governed by the evolution of surrounding granules and results in magnetic field oscillations of the global entity.

6.5 Correlation between mesogranules, sinks, and magnetic fields

From visual inspection of the sinks and the study of individual examples (see also Chapter 4 and Balmaceda et al. 2010; Bonet et al. 2010; Vargas Domínguez et al. 2015), we obtain indications that strong-field magnetic features concentrate preferentially at well localized places in the centers of sinks. In order to obtain a quantitative estimate of the spatial distribution of magnetic fields[4], for each threshold value B_{th} in the range $[0, 1000]$ G, we consider the number of pixels with $|B_{\text{long}}| > B_{\text{th}}$ in the FOV and compute the percentage of those pixels that are located within the different subareas (i.e., mesogranules, mesolanes, and sinks). The result is displayed in Figure 6.9 (a) for the combination of both observed regions (S_1+S_2) at $t = 18.3$ minutes. Different line colors indicate different locations, namely, green for mesolanes, blue for mesogranules, and red for sinks. Mesolane and mesogranule curves add up to 100 % at each B_{th} value according to our definition (i.e., the sum of both areas cover the entire FOV), whereas the red curve for sinks is just a subregion of

---

[4] In what follows, we remove from our analysis the prominent positive patch appearing at the top-left edge of the time series S_1 (Figure 6.1 (b)). This magnetic structure enters partially into the FOV in the course of the time series, and it is located at the edge of the FOV, where the horizontal flow fields are not properly determined.

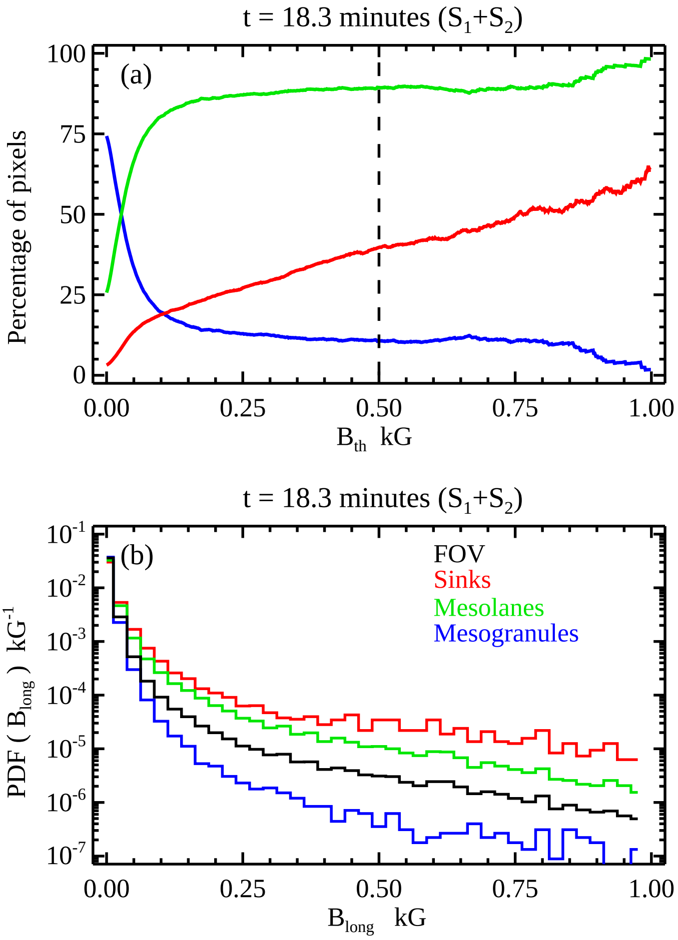

Figure 6.9: Panels (a): percentage of pixels with $|B_{\rm long}|$ above the value $B_{\rm th}$ given in the abscissa as obtained in both time series at $t = 18.3$ minutes. Panel (b): probability density functions of $|B_{\rm long}|$ at $t = 18.3$ minutes in both time series. The black, red, green, and blue solid lines stand for all pixels in the FOV, sinks, mesolanes, and mesogranules, respectively.

mesolanes. The curves show that the magnetic structures are mainly located at mesolanes. In agreement with Yelles Chaouche et al. (2011), 80 % of the pixels harboring fields with longitudinal component larger than 100 G are located in mesolanes. We also find that the fraction of pixels stronger than $B_{\rm th}$ increases linearly with $B_{\rm th}$ in sinks. Actually, 40 % of the pixels with $|B_{\rm long}| \gtrsim 500$ G (see vertical dashed line in Figure 6.9 (a)) are located in the sinks or in their close vicinity. Such a large concentration of strong fields in the sinks is very remarkable, since sinks occupy only 3 % of the surface area in contrast with the 26 %

of the mesolanes. This statement can be better visualized through the corresponding probability density functions (PDFs) displayed in Figure 6.9 (b). All the PDFs peak at 0 G, and then decrease rapidly toward stronger fields. This decrease is steeper for mesolanes than for sinks, and even more abrupt for mesogranules. All these measurements suggest that the magnetic fields in the quiet-Sun areas are preferentially located at well localized long-living downdrafts. In Appendix A we perform a statistical analysis of these longitudinal magnetic field distributions.

On granular scales, observations indicate that there is a continuous injection of magnetic flux in the form of small-scale magnetic loops (e.g., Martínez González & Bellot Rubio 2009). Exploring, then, whether any preferential location also applies to these loops is in order. In Figure 6.1 (a) and (c) black filled circles show the distribution of the average position between both footpoints of each detected loop. The locations of magnetic loops have been identified by Martínez González et al. (2012a). The average initial distance between footpoints was found to be ~ 0.25 Mm. To represent the surface area covered by loops, we have built a binary mask by defining them as 0.25 Mm diameter circles around the average position between both footpoints. We count the number of pixels in both observed regions and find that 69.5 % of them are located in mesogranules, 30.5 % in mesolanes, and only 4.5 % in sinks. These values are close to those of the surface fraction covered by each region (74 % mesogranules, 26 % mesolanes, and 3 % sinks), suggesting that magnetic loops are homogeneously distributed on mesogranular scales except in the dead calm areas where no loop is seen to emerge (Martínez González et al. 2012a).

6.5.1 Mesogranule: a case study

In Figure 6.10 we zoom in on one of the mesogranules. Panel (a) shows the divergence map with the overlaid white arrows displaying the horizontal flow field. The mesogranule is characterized by a strong positive divergence and a horizontal flow directed from the center of the map outward. The time sequence of the continuum intensity in panel (d) reveals the recurrent appearance of exploding granules. The location of these granules prior to their fragmentation is marked by white arrows. Such families of repeatedly splitting granules can persist for long times (up to 8 hours; Roudier et al. 2003) and when averaged in time they give rise to positive divergences that are identified as mesogranules (Roudier & Muller 2004).

In panel (b) a longitudinal magnetogram at $t = 18.3$ minutes is shown. The green contours trace the mesolanes and the red circles display the locations of sinks. Notice that in panel (a) the sinks are found at strong negative divergence areas in which the horizontal flows converge. In the magnetogram, the majority of the magnetic elements are located

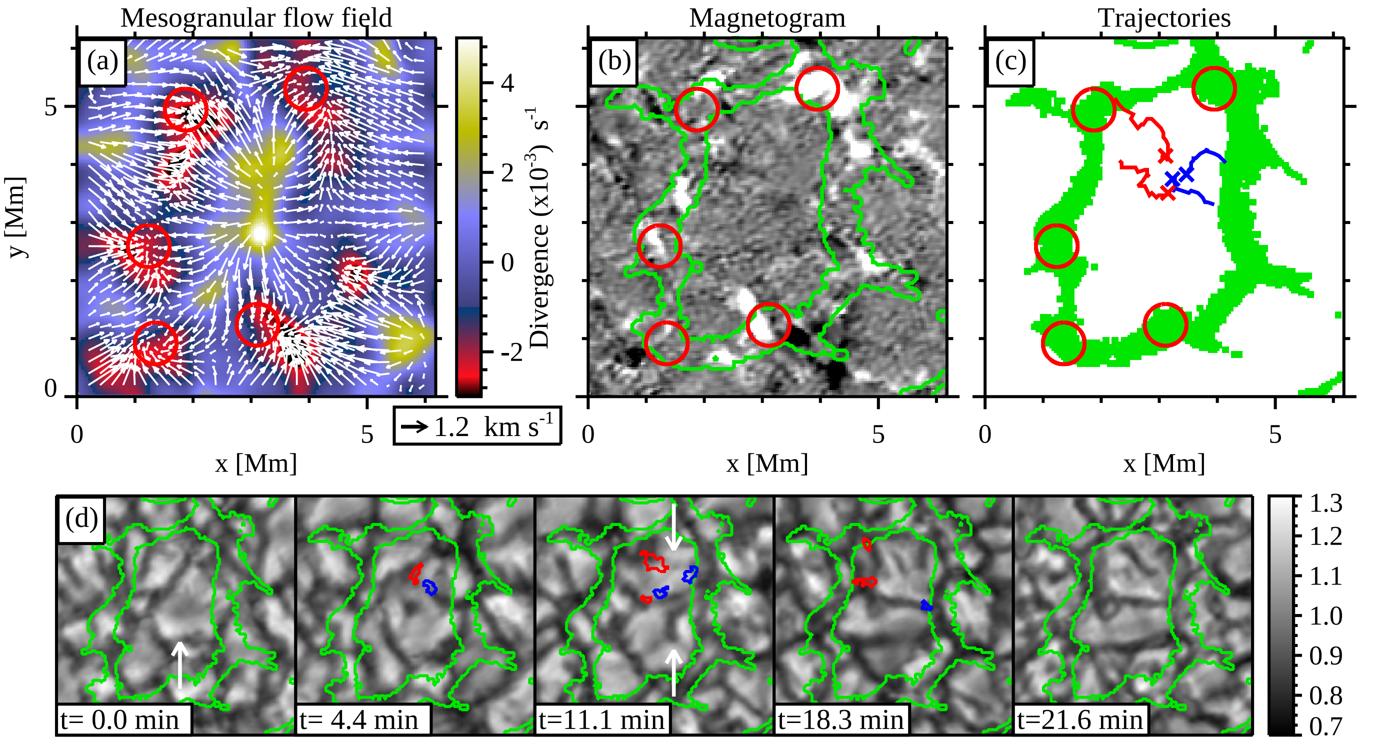

Figure 6.10: Closeup of a mesogranule. The area is located within the black solid rectangle in Figure 6.1. Panel (a): divergence map (background image) and mesogranular flow field (white arrows). Negative values represent convergence. Panel (b): longitudinal magnetogram at $t = 18.3$ minutes saturated at ± 50 G. Green contours delineate the mesolanes. Panel (c): mesolanes (green pixels) and trajectories followed by the footpoints of initially detected small-scale magnetic loops. Blue and red paths refer to the positive and negative polarity magnetic patches, respectively. Crosses indicate the initial position of the footpoints. Red circles (with a radius of 9 pixel ~ 360 km) represent the positions of sinks. Panel (d): a time sequence of continuum intensity maps covering the same field of view. Arrows indicate exploding granules. Blue and red contours represent positive and negative polarity magnetic patches, respectively.

within the mesolanes and in particular inside or near sinks. As an example, in the bottom right sink two opposite polarity features are found and in the upper right one a prominent magnetic element is observed. The evolution of the latter was studied in detail in Chapter 5. It contains multiple inner magnetic cores which are continuously being fragmented and merged driven by the evolution of surrounding granules. Here, we find that this structure is indeed anchored to a persistent downdraft. This constant inward attraction may help maintain all the fragments together in a single magnetic structure. This is just one example of the processes occurring when a magnetic structure is located in a sink (see Section 6.4).

In the interior of the mesogranular cell, smaller magnetic patches are also observed. These features are much weaker, with a longitudinal magnetic field component smaller than 50 G. Some of them have been identified as small loop-like structures because a linear polarization patch appears flanked by two opposite polarities in the longitudinal magnetograms. We have tracked the evolution of their footpoints manually until they merge, cancel with other features, or fade away below the detection limit. We display their trajectories in panel (c). Blue and red lines stand for positive and negative polarity patches and crosses indicate their initial positions. Interestingly, they move radially toward the mesolanes, although they also describe random motions at smaller scales (cf. Abramenko et al. 2011; Manso Sainz et al. 2011; Jafarzadeh et al. 2014). In panel (d) we also show the evolution of these patches overlaid on continuum intensity maps. Blue and red contours represent positive and negative polarity patches, respectively. They appear located at the edges of granules and are swept to the mesogranular lanes as the granules expand and explode. The uppermost negative polarity patch reaches the periphery of a sink where it soon cancels out with an opposite polarity feature. These two features are observed prior to their cancellation at the upper border of the top left sink in panel (b).

6.6 Discussion and conclusions

The accurate polarimetric measurements and high spatial resolution of the Sunrise/IMaX data have allowed us to quantify the relation between quiet-Sun magnetic fields, mesogranulation, and convectively driven sinks. We have computed the horizontal flow field through LCT of continuum intensity maps averaged over two time series of roughly 20 minutes each. From the inferred horizontal velocity vectors, we identified the mesogranular lanes and the convergence centers by tracking the evolution of Lagrange tracers. The converging flows are preferentially located at the junction of multiple mesograngranular lanes. According to the cork trajectories and the distribution of the converging flow fields we have found two types of *converging flows*, namely, (1) *radial flows*: radially symmetrical flow fields directed inwards to the convergence center; and (2) *vortex flows*: flow fields rotating around a vertical axis. We have detected 131 long-living converging flows, 65 % belonging to type 1, and the rest to type 2. This results in 6.7×10^{-2} converging flows per Mm^2, 4.4×10^{-2} radial flows per Mm^2 and 2.4×10^{-2} vortex flows per Mm^2, respectively. The value for vortex flows is comparable to that found by Vargas Domínguez et al. (2011). It is important to remember that our LCT temporal average (21.6 minutes) and the tracking window (600 km) is almost identical to those used by Vargas Domínguez et al. (2011) of 20 minutes and 725 km, respectively.

We did not find a preferred sense of rotation for the vortices (21 counterclockwise and 25 clockwise), compatible with Bonet et al. (2008) and Vargas Domínguez et al. (2011), but not with Bonet et al. (2010), who found a significant preference for the counterclockwise rotation. There are several possible reasons for this discrepancy. First, their detection is based on magnetograms, where they look for magnetic structures that seem to rotate, while here we detect them irrespectively of whether they harbor magnetic fields or not. Second, they focus only on an *effective* FOV of $28\farcs5 \times 28\farcs5$, where the magnetograph signals are largest within the second time series analyzed here (see Figure 6.1 (d)). Third, they detected short-lived vortices as well, which are diluted by the LCT temporal average in our analysis.

Unlike in previous works, here we have profited from the spectroscopic capabilities of IMaX to determine LOS velocities in converging flows. The LOS velocity histograms have revealed that converging flows are (1) preferentially located within intergranular lanes and (2) tend to be associated with long-lived downdrafts. Accordingly, converging flows are better described by convectively driven sinks.

By studying individual examples, we have shown that sinks can affect the evolution of magnetic elements. In particular, coalescence, cancellation and fragmentation processes are seen to take place at localized downdrafts. We have also provided quantitative measurements of the relationship between magnetic fields, mesogranules and sinks. We have first confirmed the finding of Yelles Chaouche et al. (2011) that the large majority (80 %) of magnetic fields with longitudinal component larger than 100 G are located in mesogranular lanes. In addition, we have shown that the strongest magnetic features tend to concentrate in long-living sinks, at the junction of mesogranules. Roughly 40 % of the magnetic elements with longitudinal magnetic fields above 500 G are found within 360 km of sink centers. In contrast, we found that 69.5 % of the 400 small-scale magnetic loops detected by Martínez González et al. (2012a) are located in mesogranules, 30.5 % in mesolanes, and only 4.5 % in the close neighborhood of long-living sinks. These values are very similar to the surface fractions covered by each region and we conclude that magnetic loops are homogeneously distributed on mesogranular scales.

We have analyzed the evolution of two particular loops appearing inside a mesogranule. Their footpoints are passively advected by the mesogranular horizontal flows, as they are swept by exploding granules. Through this process they reach the boundaries of the underlying mesogranules and well localized sinks located at the vertices of mesogranular lanes. In such a downdraft they can be confined by converging granular flows and later concentrated up to kG values (Bushby et al. 2008; Danilovic et al. 2010a, and Chapter 4). The advection of weak fields by mesogranular horizontal flows and their concentration in mesogranular vertices is also supported by magnetoconvection models that study the interaction of convective flows with an imposed field (see e.g., Stein & Nordlund 2006). However, a small-scale dynamo can be consistent as well with the organization of strong flux concentrations in mesogranular lanes, provided that the computational domain is large enough (Rempel 2014). In fact, a small-scale dynamo is more efficient when the mesogranulation is also present (Bushby & Favier 2014), and the coverage by kG fields doubles as a strong mesogranular network is formed (Rempel 2014).

Our results seem to reveal a hierarchical picture for the evolution of quiet Sun magnetic fields: flux emerges preferentially near the edges of granules in the form of small-scale magnetic loops (Centeno et al. 2007; Martínez González & Bellot Rubio 2009; Danilovic et al. 2010b); the footpoints are first swept to nearby intergranular lanes unless they cancel out before (Centeno et al. 2007, Chapter 4), and then advected to mesogranular lanes, particularly to the junctions where long-lived downdrafts are formed. The concentration of weak fields in the mesogranular vertices gives rise to internetwork magnetic elements. If these magnetic elements are strong (long-lived) enough, supergranular flows can drag them along (de Wijn et al. 2008; Orozco Suárez et al. 2012), until they reach the supergranular boundaries and eventually contribute to the magnetic network flux (Gošić et al. 2014). Interestingly, this qualitative scenario may explain why most of the newly detected internetwork flux is not in the form of bipolar elements, but instead seems to be unipolar (Lamb et al. 2008; Gošić 2015; Anusha et al. 2016). Unipolar appearances are thought to be the result of the coalescence of previously unobservable, very weak flux into stronger features, as first pointed out by Lamb et al. (2008). The concentration of weak fields in sinks provides a plausible mechanism whereby this can occur.

7

CONCLUSIONS

We have studied the evolution of quiet-Sun magnetic features based on high-quality spectropolarimetric observations. To this end, we have employed high spatial and temporal resolution time series of polarimetric images at the diffraction limit of a 1-m telescope. The data have been acquired with the IMaX spectropolarimeter during the first flight of the SUNRISE balloon-borne mission.

We have applied the SIR inversion code to the four Stokes profiles of the Fe I line at 525.02 nm measured by IMaX. Through this process we have inferred the model parameters that characterize the solar photosphere such as the vector magnetic field and the line-of-sight velocity. In the inversion, we have assumed that these physical parameters are constant with depth. We have also applied the local correlation tracking technique to the time series of continuum intensity images. This has allowed us to derive the horizontal proper motions of the solar granulation. Therefore we have obtained horizontal velocity flow field maps, and from those we have computed the flow divergence and the vertical vorticity images.

First of all, we have reported on the formation and evolution of an isolated quiet-Sun magnetic element and its interaction with the neighboring convection. Seen at a scale of one hundred kilometers, we have found that this is a complex process where many phenomena are involved. The formation starts when a small-scale magnetic Ω loop with field strength of ~ 200 G emerges to the solar surface in a granular upflow. Its footpoints are soon swept to nearby intergranular lanes where some, weak positive polarity patches are already present. The negative polarity footpoint cancels out, likely through a reconnection process, with an opposite polarity feature. Meanwhile the positive polarity footpoint and the other remaining patches are advected by converging granular flows toward a long-living sink. The magnetic fields are confined and concentrated in the sink and a magnetic element with field strength ($\sim 500\,\mathrm{G}$) in equipartition with the kinetic energy density of the convective motions is formed. The intergranular downflow then starts to increase within the magnetic feature and the surrounding granules compress the structure until the field strengths increases up to $\sim 1.5\,\mathrm{kG}$ values. During this process, a bright point (BP) appears at the edge of the flux concentration together with a co-spatial upflow feature. The evolution of the BP is closely related to that of the upflow as an anti-phase correlation between the continuum intensity and the line-of-sight velocity is observed. At the end of the intensification phase, strong downflow plumes, with speeds roughly up to $6\,\mathrm{km\,s^{-1}}$, also develop at the periphery of the magnetic element. The gas required for producing such strong and narrow downdrafts is likely provided by converging granules. The development of the magnetic element does not stop here, and we have discovered that it is indeed unstable. The magnetic element displays an oscillatory behavior as the field strength weakens and rises again with time.

In summary, we can say that the history of our magnetic element encompassed three main phases, namely, (1) flux concentration in a long-living sink by granular advection; (2) evacuation by a downflow and intensification to kG strength by granular compression; and (3) unstable evolution of the mature magnetic element.

We have also investigated the dynamics of quiet-Sun magnetic features. Specifically, we have focused on those magnetic structures that appear associated with chains of bright points. The dynamical interaction of these features with the convective flows have been analyzed and we have drawn the following conclusions:

- These magnetic structures are resolvable into a series of more elemental inner magnetic cores, each of which appears related with a single bright point.
- The strong and vertical inner cores are surrounded by common, weaker and more inclined fields, suggesting that we are witnessing a collection of flux concentrations in the lower photosphere that expand with height and merge into a common canopy in the upper photospheric layers.
- The evolution of the individual magnetic cores is completely governed by the local granular convection flows.
- They continuously intensify, fragment, and merge in the same way that chains of bright points in photometric observations have been reported to do.
- This evolutionary behavior results in magnetic field oscillations of the global entity.
- The magnetic field oscillations first reported by Martínez González et al. (2011) correspond to the forcing by granular motions and not to characteristic oscillatory modes of thin flux tubes.

Finally, we have studied the relation between mesogranular convective flows, localized downdrafts, and quiet-Sun magnetic fields. With this purpose in mind, we have first identified the mesogranular lanes and the central position of sinks. We have detected 131 sinks at the junctions of multiple mesogranular lanes. We have found two types of sinks, namely, (1) *radial flows* displaying radially symmetrical converging flows; and (2) *vortex flows* that manifest as whirlpools. Their main properties are:

- The sinks are located in negative divergence areas with a median value of $-1.9 \times 10^{-3}\,\mathrm{s}^{-1}$.
- The 65 % of sinks display radial flows, and the remaining 35 % vortex flows.
- The vortices do not show a preferred sense of rotation with 46% being counterclockwise and 54% clockwise.

We have provided quantitative measurements of the spatial distribution of magnetic fields. We have found that the 40 % of the pixels with longitudinal magnetic fields above 500 G are located within sinks. From these results we have concluded that the strongest magnetic structures tend to concentrate at well localized long-living downdrafts at the mesogranular junctions. Among them are the magnetic elements studied in Chapter 4, and the multi-cored magnetic structure analyzed in detail in Chapter 5. Meanwhile the small-scale magnetic loops do not show any preferential distribution at mesogranular scales. However, we have observed that the footpoints of magnetic loops appearing inside the mesogranules can be advected by horizontal mesogranular flows toward the mesogranular boundaries and in particular to their vertices.

All these results could be understood in a single evolutionary path: flux emerges preferentially at granules in the form of small-scale magnetic loops. The footpoints are first swept to nearby intergranular lanes, and then advected further to mesogranular lanes, especially, to those junctions where long-living sinks are formed. The weak fields are confined in the mesogranular vertices, concentrated by converging granular flows and intensified up to kG values. The newly formed magnetic element is constantly being buffeted by surrounding granules and is fragmented into a series of more elemental inner magnetic cores. The continuous inward advection to the sink, however, prevents the cores to be detached from the global structure and even fuse them again into a single magnetic element. The recurrent coalescence and fragmentation of magnetic cores finally results in magnetic field oscillations of the magnetic feature.

A

DISTRIBUTION OF LONGITUDINAL MAGNETIC FIELDS

In this Appendix we perform a statistical analysis of the longitudinal magnetic field distribution. We consider all pixels with values $\geq 25\,\mathrm{G}$ (about 2 times the sensitivity of the longitudinal magnetograms, see Martínez Pillet et al. 2011a) and $< 1000\,\mathrm{G}$ (above this value it gets statistically poor) over the two observed areas at $t = 21.6$ minutes. Figure A.1 displays the resulting PDF for both log-linear (a) and log-log (b) graphs. From the log-linear plot it is evident that an exponential distribution can not describe the observed PDF over the whole range of magnetic fields. If such a distribution is able to fit the PDF at small fields where it drops steeply, then an excess of stronger fields should be found in the tail of the distribution, and vice versa. On the other hand, the log-log plot reveals that the distribution follows almost a straight line. This fact strongly suggests a power-law PDF as the most promising distribution for describing our observations. Accordingly, we first attempt to fit the distribution of magnetic fields with a power-law PDF, which has the form

$$\mathrm{PDF}(x) = C_1 x^{-\alpha} \tag{A.1}$$

where the exponent α is known as the *scaling parameter*.

In practice, if empirical data follow a power-law distribution, they do so only for values above some lower bound x_0 (Clauset et al. 2007a). In order to estimate this lower value we follow the approach proposed by Clauset et al. (2007b). This method consists in choosing the value of x_0 so that the PDFs of both the observed data and the best-fit model are as close as possible. A common way to quantify the difference between two PDFs is through

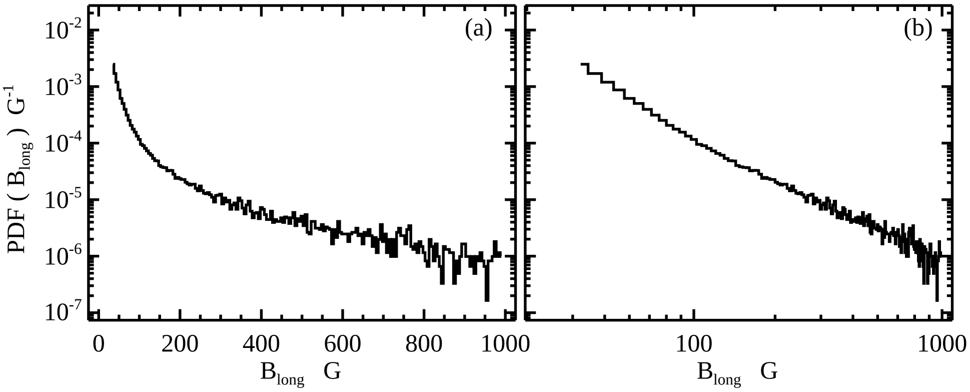

Figure A.1: (a) Log-linear and (b) log-log graph showing the PDF of $|B_{\text{long}}|$ over the two observed areas at $t = 21.6$ minutes for all pixels with $|B_{\text{long}}| \geq 25$ G.

the Kolmogorov-Smirnov (K-S), D, statistics (Press et al. 1992), which is given by the maximum absolute deviation between the cumulative distribution functions (CDFs) of the data and the model:

$$D = max\left|\text{CDF}_{\text{obs}}(x) - \text{CDF}_{\text{mod}}(x)\right|. \tag{A.2}$$

$\text{CDF}_{\text{obs}}(x)$ is derived from the observed PDF and $\text{CDF}_{\text{mod}}(x)$ from the model PDF as obtained through a least-square fitting. The CDFs are calculated from the corresponding PDFs by

$$\text{CDF}(x) = \int_{x_0}^{x} \text{PDF}(x')dx'. \tag{A.3}$$

Through this method we estimate a lower bound value of $x_0 = 135$ G. The resulting best-fitting power-law model is shown in Figure A.2 (b), where the solid black and the dashed red lines display the observed and the fitted distributions, respectively. The least-squares fitting gives a scaling parameter value of $\alpha = 2.02$. In order to quantify the uncertainty in our estimate for the scaling parameter we vary the truncation value x_0 in the range 35–235 G. This leads to a scaling parameter that range over 1.98–2.04.

For comparison, we attempt to fit the observed distribution with other three different PDFs, namely, exponential, Weibull, and lognormal distributions. Such distributions have been found to fit well different magnetogram data (e.g., Schrijver et al. 1997; Hagenaar 2001; Parnell 2002; Hagenaar et al. 2003; Abramenko & Longcope 2005). An exponential

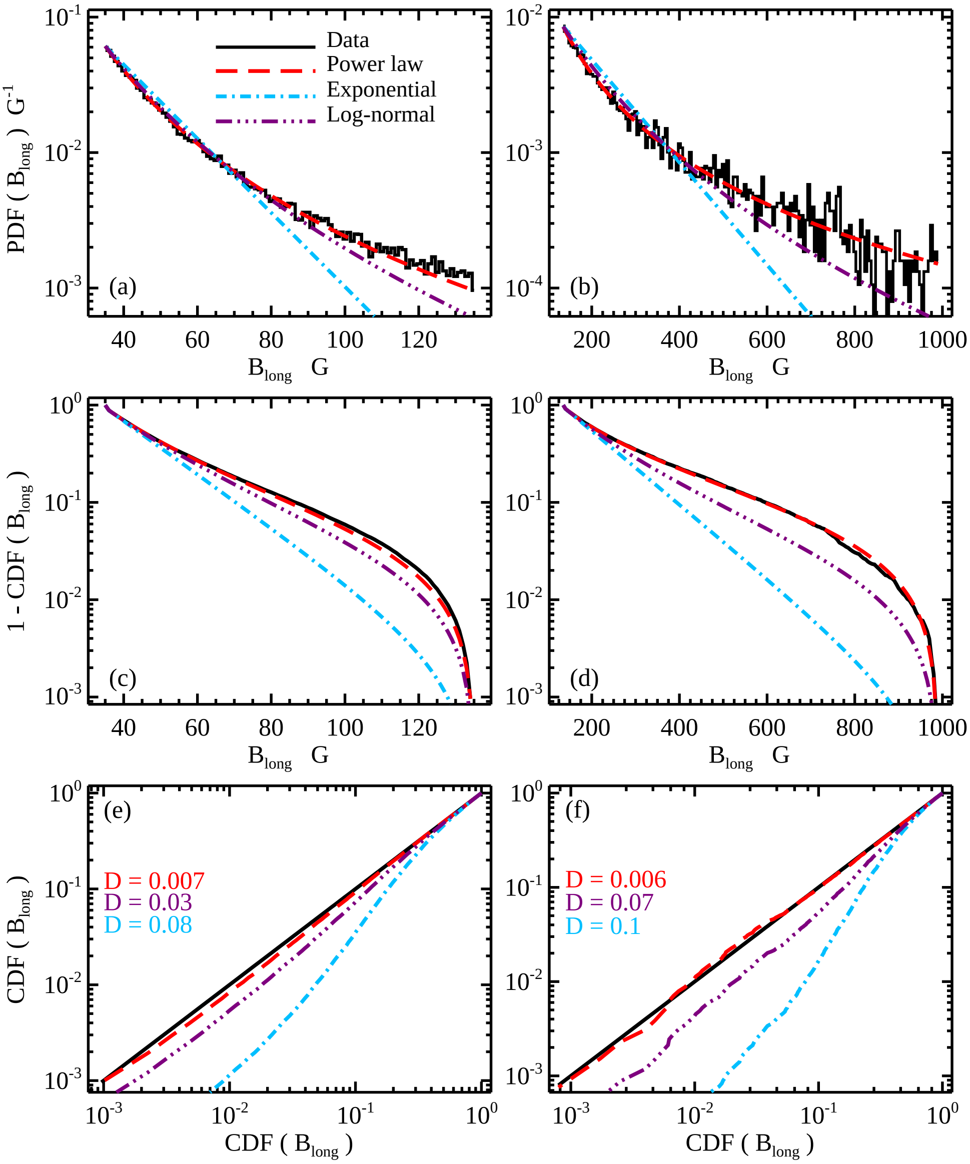

Figure A.2: Top panels: PDFs of the longitudinal magnetic field component calculated at $t = 21.6$ minutes over both time series in the range 35–135 G (left) and 135–1000 G (right). The different lines show the observed PDF (black) and the best-fitting PDFs for power-law (red), exponential (blue), and log-normal (purple) functions. Middle panels: corresponding survival functions, 1-CDF(x), versus $|B_{\text{long}}|$. Bottom panels: P-P plots of the best-fitting CDFs versus the observed CDF.

Table A.1: Parameters for the best-fitting PDFs in the range 135–1000 G. The errors are equal to the standard deviation of the parameters for 41 different values of x_0.

PDF	C_i	Parameters	D
Power law	173.45	$\alpha = 2.02 \pm 0.01$	0.006
Exponential	0.02	$\lambda = 0.009 \pm 0.001$	0.1
Weibull	18.25	$\gamma = -1.03 \pm 0.01$	0.007
		$\beta = 3 \pm 6$	
Lognormal	1.22	$\sigma = 4 \pm 1$	0.07
		$\mu = 18 \pm 6$	

distribution is given by

$$\mathrm{PDF}(x) = C_2 e^{-\lambda x}, \tag{A.4}$$

a Weibull PDF has the form

$$\mathrm{PDF}(x) = C_3 (\frac{x}{\beta})^{\gamma-1} e^{-(\frac{x}{\beta})^{\gamma}}, \tag{A.5}$$

and a lognormal distribution corresponds to

$$\mathrm{PDF}(x) = C_4 e^{-\frac{1}{2}(\frac{ln x-\mu}{\sigma})^2}. \tag{A.6}$$

Their best least-squares fit to the data are shown in Figure A.2 (b). The blue and purple lines represent the exponential and lognormal distributions, respectively, whilst the Weibull PDF is not displayed as it follows the same distribution as that for the power-law (red line). The Weibull PDF has a combination of a power law and an exponential term. It has two unknowns, γ and β with values of -1.03 and 3, respectively. Notice that with these values the Weibull PDF recovers a power-law distribution with a scaling parameter of 2.03. The different best-fitting parameter values are listed in column (3) of Table A.1.

In order to quantify the quality of each fitted model we use the K-S goodness-of-fit test. The K-S statistics D, namely, the maximum absolute deviations between the model and the observed CDF, are listed in column (4) of Table A.1. Another way to compare the quality of each model is to plot the model CDF versus the observed one. Such a plot is called a P-P plot and is displayed in Figure A.2 (f). The model is better as it approaches the $x = y$ line. From both the P-P plot and the K-S statistics D we find that the PDF that better describes the observations is a power-law distribution. This can already be concluded from Figure A.2 (d) through direct comparison of the model and observed survival functions, 1-CDF(x).

Table A.2: Parameters for the best-fitting PDFs in the range 35–135 G. The errors are equal to the standard deviation of the parameters for 31 different values of x_0.

PDF	C$_i$	Parameters	D
Power law	3469.25	$\alpha = 3.08 \pm 0.05$	0.007
Exponential	0.51	$\lambda = 0.06 \pm 0.01$	0.08
Weibull	8.42	$\gamma = -2.12 \pm 0.06$ $\beta = 7 \pm 2$	0.008
Lognormal	9.59	$\sigma = 18 \pm 58$ $\mu = 33 \pm 113$	0.03

Now that we have identified the most plausible distribution in the range 135–1000 G, we wonder if the lower part of the observed PDF also follows a given trend. In order to answer this question we proceed in the same way as before but this time with an upper value in the distribution of 135 G. We estimate a lower bound value of $x_0 = 35$ G, which is equal to 2.5 times the sensitivity of the longitudinal magnetograms of 14 G (see, Martínez Pillet et al. 2011a). The best-fitting parameters and the K-S statistics of each model are listed in Table A.2. In Figure A.2 we also display the PDFs (a), the survival functions (c), and the P-P plots (e) of the different distributions. We find that a power-law PDF with a scaling parameter of $\alpha = 3.08$ is the most consistent distribution in the range 35–135 G.

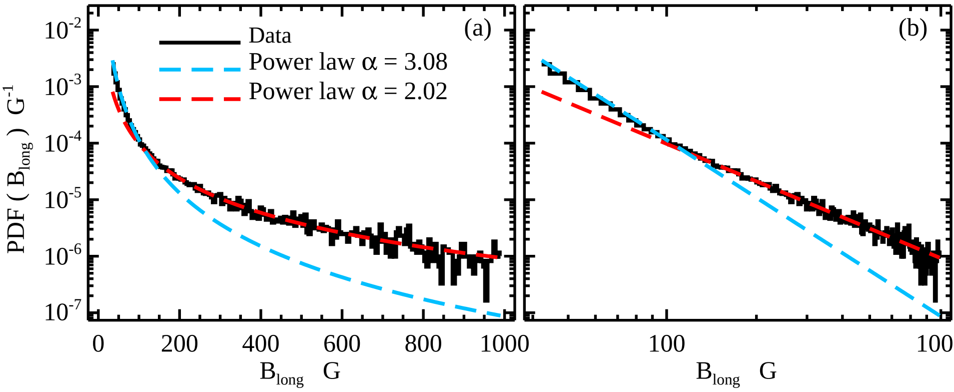

Figure A.3: (a) Log-linear and (b) log-log plot of the observed PDF of $|B_{\mathrm{long}}|$ in the range of 35–1000 G (black line). The blue and red dashed line display the fitted power-law PDFs with scaling parameters of 3.08 and 2.02, respectively.

A.0.1 Physical interpretation

The above results suggest that a double power-law PDF is consistent with the distribution of the longitudinal magnetic field component observed in the quiet Sun. Figure A.3 displays the observed PDF and the two derived power-law distributions in the range of 35–1000 G. It is worth noting that the distribution is steeply divided into two well-behaved power laws. This is particularly evident in the log-log plot of Figure A.3 (b) where the slope of the distribution is seen to change abruptly at the value of 135 G. This behavior suggests that magnetic fields found below and above 135 G could be generated by two different mechanisms.

In the quiet Sun, a large amount of the weakest magnetic fields are found in the form of small-scale emerging loops (see e.g., Martínez González & Bellot Rubio 2009). On the other hand, roughly 85 % of pixels with longitudinal magnetic field higher than ~ 100 G are located in the near neighborhood of mesogranular lanes (Yelles Chaouche et al. 2011). Remarkably, as shown by the green lines in the upper panels of Figure 6.9, this percentage of pixels reaches a plateau above the values between 100–150 G. In addition, in Section 6.5, we have seen that the strongest magnetic fields tends to concentrate in well localized downdrafts. At these sinks the magnetic elements are seen to merge, fragment, and partially cancel with opposite polarity features. Taking into account these evolutionary behavior of magnetic structures, we can conjecture that the steepest power law found in the range 35–135 G can be dominated by the emergence of small-scale loops, while the power law observed in the range 135–1000 G may be produced by surface processes such as coalescence, fragmentation and cancellation (see Section 6.4).

This idea could indeed be supported by previous observations of the magnetic flux distribution in the solar photosphere. In particular, Parnell et al. (2009) analyzed longitudinal magnetograms taken by *Hinode*/NFI and SOHO/MDI (Scherrer et al. 1995) using a magnetic feature identification algorithm. They found that the flux distribution of the magnetic features follow a single power law with a scaling parameter of 1.85 over 5 orders of magnitude in flux, from the smallest internetwork features to the largest sunspots. They suggest that this result indicate that either all photospheric magnetic features are generated by the same physical mechanism, or that they are dominated by surface processes, which determine their flux contents and produce a scale-free distribution. To discriminate between these two scenarios, Thornton & Parnell (2011) focused only on emergence events and found that they follow a single power law with a negative slope 2.69 over a broad range of sizes in the Sun. They concluded that this favors the first scenario, namely that all magnetic features are created by the same dynamo mechanism.

If their results are also valid in the smaller scales that we detect with our improved spatial resolution, then we would expect that the steepest power law that we have found in the range

35–135 G is produced by emergence events while the more moderate slope found in the tail of the distribution could be related with surface processes. Even if in our inversions the filling factor is equal to one and thus the longitudinal magnetic field that we measure is proportional to the magnetic flux, we can not directly compare our scaling parameter values with those obtained by Parnell et al. (2009) and Thornton & Parnell (2011): we study the distribution of the flux found in each pixel and not that of individual features.

REFERENCES

Abramenko, V. I., & Longcope, D. W. 2005, ApJ, 619, 1160

Abramenko, V. I., Carbone, V., Yurchyshyn, V., et al. 2011, ApJ, 743, 133

Anusha, L. S., Solanki, S. K., Hirzberger, J., et al. 2016, A&A, submitted

Asensio Ramos, A. 2009, ApJ, 701, 1032

Attie, R., Innes, D. E., & Potts, H. E. 2009, A&A, 493, L13

Babcock, H. W., & Babcock, H. D. 1955, ApJ, 121, 349

Balmaceda, L., Vargas Domínguez, S., Palacios, J., Cabello, I., & Domingo, V. 2010, A&A, 513, L6

Barthol, P., Gandorfer, A., Solanki, S. K., et al. 2011, SoPh, 268, 1

Beck, C., Bellot Rubio, L. R., Schlichenmaier, R., Sütterlin, P. 2007a, A&A, 472, 607

Beck, C., Mikurda, K., Bellot Rubio, L. R., Schlichenmaier, R., Sütterlin, P. 2007b, Modern Solar Facilities–Advanced Solar Science, ed. F. Kneer, K. G. Puschmann & A. D. Wittmann. Published by Universitätsverlag Göttingen, 165

Bellot Rubio, L. R., Ruiz Cobo, B., & Collados, M. 1997, ApJL, 478, L45

Bellot Rubio, L. R., Ruiz Cobo, B., & Collados, M. 1998, ApJ, 506, 805

Bellot Rubio, L. R., Ruiz Cobo, B., & Collados, M. 2000, ApJ, 535, 489

Bellot Rubio, L. R., Rodríguez Hidalgo, I., Collados, M., Khomenko, E., & Ruiz Cobo, B. 2001, ApJ, 560, 1010

Bellot Rubio, L. R., & Collados, M. 2003, A&A, 406, 357

Bellot Rubio, L. R., & Orozco Suárez, D. 2015, Living Reviews in Solar Physics, in press

Berger, T. E., & Title, A. M. 1996, ApJ, 463, 365

Berger, T. E., Löfdahl, M. G., Shine, R. S., & Title, A. M. 1998, ApJ, 495, 973

Berger, T. E., & Title, A. M. 2001, ApJ, 553, 449

Berger, T. E., Rouppe van der Voort, L. H. M., Löfdahl, M. G., et al. 2004, A&A, 428, 613

Berkefeld, T., Schmidt, W., Soltau, D., et al. 2011, SoPh, 268, 103

Bonet, J. A., Márquez, I., Sánchez Almeida, J., Cabello, I., & Domingo, V. 2008, ApJL, 687, L131

Bonet, J. A., Márquez, I., Sánchez Almeida, J., et al. 2010, ApJL, 723, L139

Borrero, J. M., Martínez-Pillet, V., Schlichenmaier, R., et al. 2010, ApJL, 723, L144

Borrero, J. M., & Kobel, P. 2011, A&A, 527, A29

Brandt, P. N., Scharmer, G. B., Ferguson, S., Shine, R. A., & Tarbell, T. D. 1988, Nature, 335, 238

Brandt, P. N., Ferguson, S., Shine, R. A., Tarbell, T. D., & Scharmer, G. B. 1991, A&A, 241, 219

Buehler, D., Lagg, A., Solanki, S. K., & van Noort, M. 2015, A&A, 576, A27

Bünte, M., Steiner, O., & Pizzo, V. J. 1993, A&A, 268, 299

Bünte, M. 1993, A&A, 276, 236

Bushby, P. J., Houghton, S. M., Proctor, M. R. E., & Weiss, N. O. 2008, MNRAS, 387, 698

Bushby, P. J., Favier, B., Proctor, M. R. E., & Weiss, N. O. 2012, Geophysical and Astrophysical Fluid Dynamics, 106, 508

Bushby, P. J., & Favier, B. 2014, A&A, 562, A72

Cattaneo, F. 1999, ApJL, 515, L39

Cattaneo, F., Lenz, D., & Weiss, N. 2001, ApJL, 563, L91

Centeno, R., Socas-Navarro, H., Lites, B., et al. 2007, ApJL, 666, L137

Clauset, A., Rohilla Shalizi, C., & Newman, M. E. J. 2007a, arXiv:0706.1062

Clauset, A., Young, M., & Gleditsch, K. S. 2007b, The Journal of Conflict Resolution, 51, 58

Danilovic, S., Schüssler, M., & Solanki, S. K. 2010a, A&A, 509, A76

Danilovic, S., Beeck, B., Pietarila, A., et al. 2010b, ApJL, 723, L149

Deinzer, W., Hensler, G., Schüssler, M., & Weisshaar, E. 1984, A&A, 139, 435

Del Toro Iniesta, J. C. 1996, Vistas in Astronomy, 40, 241

Del Toro Iniesta, J. C., & Ruiz Cobo, B. 1996, SoPh, 164, 169

Del Toro Iniesta, J. C., & Collados, M. 2000, AO, 39, 1637

Del Toro Iniesta, J. C. 2003, Introduction to Spectropolarimetry (Cambridge: Cambridge Univ. Press)

Del Toro Iniesta, J. C., Orozco Suárez, D., & Bellot Rubio, L. R. 2010, ApJ, 711, 312

Del Toro Iniesta, J. C., & Martínez Pillet, V. 2012, ApJS, 201, 22

de Wijn, A. G., Rutten, R. J., Haverkamp, E. M. W. P., Sütterlin, P. 2005, A&A, 441, 1183

de Wijn, A. G., Lites, B. W., Berger, T. E., et al. 2008, ApJ, 684, 1469

de Wijn, A. G., Stenflo, J. O., Solanki, S. K., & Tsuneta, S. 2009, ssr, 144, 275

Domínguez Cerdeña, I. 2003, A&A, 412, L65

Domínguez Cerdeña, I., Kneer, F., & Sánchez Almeida, J. 2003a, ApJL, 582, L55

Domínguez Cerdeña, I., Sánchez Almeida, J., & Kneer, F. 2003b, A&A, 407, 741

Edwin, P. M., & Roberts, B. 1983, SoPh, 88, 179

Fischer, C. E., de Wijn, A. G., Centeno, R., Lites, B. W., & Keller, C. U. 2009, A&A, 504, 583

Foukal, P. V. 2004, Solar Astrophysics, 2nd ed. New York, Wiley-Interscience, 2004

Gandorfer, A., Grauf, B., Barthol, P., et al. 2011, SoPh, 268, 35

Gingerich, O., Noyes, R. W., Kalkofen, W., & Cuny, Y. 1971, SoPh, 18, 347

Gonsalves, R. A. 1982, Optical Engineering, 21, 829

Goode, P. R., Yurchyshyn, V., Cao, W., et al. 2010, ApJL, 714, L31

Gošić, M., Bellot Rubio, L. R., Orozco Suárez, D., Katsukawa, Y., & Del Toro Iniesta, J. C. 2014, ApJ, 797, 49

Gošić, M., Bellot Rubio, L. R., Del Toro Iniesta, J. C., Orozco Suárez, D., & Katsukawa, Y. 2015, ApJ, submitted

Gošić, M. 2015, Ph.D. Thesis, Universidad de Granada

Grossmann-Doerth, U., Schüssler, M., & Solanki, S. K. 1988, A&A, 206, L37

Grossmann-Doerth, U., Keller, C. U., & Schuessler, M. 1996, A&A, 315, 610

Grossmann-Doerth, U., Schüssler, M., & Steiner, O. 1998, A&A, 337, 928

Guglielmino, S. L., Martínez Pillet, V., Bonet, J. A., et al. 2012, ApJ, 745, 160

Hagenaar, H. J. 2001, ApJ, 555, 448

Hagenaar, H. J., Schrijver, C. J., & Title, A. M. 2003, ApJ, 584, 1107

Hale, G. E. 1908, ApJ, 28, 315

Hasan, S. S. 1985, A&A, 143, 3

Hirzberger, J., Feller, A., Riethmüller, T. L., Gandorfer, A., & Solanki, S. K. 2011, A&A, 529, A132

Howard, R., & Stenflo, J. O. 1972, SoPh, 22, 402

Ishikawa, R., Tsuneta, S., Kitakoshi, Y., et al. 2007, A&A, 472, 911

Ishikawa, R., & Tsuneta, S. 2009, A&A, 495, 607

Ishikawa, R., & Tsuneta, S. 2010, ApJL, 718, L171

Jafarzadeh, S., Solanki, S. K., Feller, A., et al. 2013, A&A, 549, A116

Jafarzadeh, S., Cameron, R. H., Solanki, S. K., et al. 2014, A&A, 563, A101

Jess, D. B., Shelyag, S., Mathioudakis, M., et al. 2012, ApJ, 746, 183

Jin, C., Wang, J., & Zhou, G. 2009, ApJ, 697, 693

Jin, C. L., Wang, J. X., & Xie, Z. X. 2012, SoPh, 280, 51

Jin, C., & Wang, J. 2015a, ApJ, 806, 174

Jin, C. L., & Wang, J. X. 2015b, ApJ, 807, 70

Kato, Y., Steiner, O., Steffen, M., & Suematsu, Y. 2011, ApJL, 730, L24

Keller, C. U. 1992, Nature, 359, 307

Kentischer, T. J., Schmidt, W., Sigwarth, M., & Uexkuell, M. V. 1998, A&A, 340, 569

Khomenko, E. V., Collados, M., Solanki, S. K., Lagg, A., & Trujillo Bueno, J. 2003, A&A, 408, 1115

Khomenko, E. V., Shelyag, S., Solanki, S. K., Vögler, A. 2005, A&A, 442, 1059

Khomenko, E., Martínez Pillet, V., Solanki, S. K., et al. 2010, ApJL, 723, L159

Kiselman, D., Rutten, R. J., & Plez, B. 2001, Recent Insights into the Physics of the Sun and Heliosphere: Highlights from SOHO and Other Space Missions, 203, 287

Kitiashvili, I. N., Kosovichev, A. G., Wray, A. A., & Mansour, N. N. 2010, ApJ, 719, 307

Kitiashvili, I. N., Kosovichev, A. G., Mansour, N. N., & Wray, A. A. 2011, ApJL, 727, L50

Klimchuk, J. A. 2006, SoPh, 234, 41

Kosugi, T., Matsuzaki, K., Sakao, T., et al. 2007, SoPh, 243, 3

Krall, N. A., & Trivelpiece, A. W. 1973, Principles of Plasma Physics (Tokyo: McGraw-Hill)

Lagg, A., Solanki, S. K., Riethmüller, T. L., et al. 2010, ApJL, 723, L164

Lamb, D. A., DeForest, C. E., Hagenaar, H. J., Parnell, C. E., & Welsch, B. T. 2008, ApJ, 674, 520-529

Landi Degl'Innocenti, E. 1987, Numerical Radiative Transfer, 265

Landi Degl'Innocenti, E., & Landolfi, M. 2004, Astrophysics and Space Science Library, 307,

Langangen, Ø., De Pontieu, B., Carlsson, M., et al. 2008, ApJL, 679, L167

Leitzinger, M., Brandt, P. N., Hanslmeier, A., Pötzi, W., & Hirzberger, J. 2005, A&A, 444, 245

Lin, H. 1995, ApJ, 446, 421

Lin, H., & Rimmele, T. 1999, ApJ, 514, 448

Lites, B. W., Rutten, R. J., & Kalkofen, W. 1993, ApJ, 414, 345

Lites, B. W., Leka, K. D., Skumanich, A., Martinez Pillet, V., & Shimizu, T. 1996, ApJ, 460, 1019

Lites, B. W., & Socas-Navarro, H. 2004, ApJ, 613, 600

Lites, B. W., Kubo, M., Socas-Navarro, H., et al. 2008, ApJ, 672, 1237

Lites, B. W. 2011, ApJ, 737, 52

Lites, B. W., Akin, D. L., Card, G., et al. 2013, SoPh, 283, 579

Livingston, W., & Harvey, J. 1971, Solar Magnetic Fields, 43, 51

Livingston, W. C., & Harvey, J. 1975, BAAS, 7, 346

Manso Sainz, R., Martínez González, M. J., & Asensio Ramos, A. 2011, A&A, 531, L9

Márquez, I., Sánchez Almeida, J., & Bonet, J. A. 2006, ApJ, 638, 553

Martin, S. F. 1984, Small-Scale Dynamical Processes in Quiet Stellar Atmospheres, 30

Martínez González, M. J., Collados, M., & Ruiz Cobo, B. 2006, A&A, 456, 1159

Martínez González, M. J., Collados, M., Ruiz Cobo, B., & Solanki, S. K. 2007, A&A, 469, L39

Martínez González, M. J., Collados, M., Ruiz Cobo, B., & Beck, C. 2008, A&A, 477, 953

Martínez González, M. J., & Bellot Rubio, L. R. 2009, ApJ, 700, 1391

Martínez González, M. J., Manso Sainz, R., Asensio Ramos, A., & Bellot Rubio, L. R. 2010, ApJL, 714, L94

Martínez González, M. J., Asensio Ramos, A., Manso Sainz, R., et al. 2011, ApJL, 730, L37

Martínez González, M. J., Manso Sainz, R., Asensio Ramos, A., & Hijano, E. 2012a, ApJ, 755, 175

Martínez González, M. J., Bellot Rubio, L. R., Solanki, S. K., et al. 2012b, ApJL, 758, L40

Martínez Pillet, V., Lites, B. W., & Skumanich, A. 1997, ApJ, 474, 810

Martínez Pillet, V., Bonet, J. A., Collados, M. V., et al. 2004, SPIE, 5487, 1152

Martínez Pillet, V. 2007, in Proc. Second Solar Orbiter Workshop, ed. L. Conroy (ESA SP-641; Noordwijk: ESA), www.esa.int/esapub/conferences/toc/tocSP641.pdf

Martínez Pillet, V., Del Toro Iniesta, J. C., Álvarez-Herrero, A., et al. 2011a, SoPh, 268, 57

Martínez Pillet, V., Del Toro Iniesta, J. C., & Quintero Noda, C. 2011b, A&A, 530, A111

Martínez Pillet, V. 2013, ssr, 178, 141

Matloch, Ł., Cameron, R., Schmitt, D., & Schüssler, M. 2009, A&A, 504, 1041

Matloch, Ł., Cameron, R., Shelyag, S., Schmitt, D., & Schüssler, M. 2010, A&A, 519, A52

Meyer, F., Schmidt, H. U., & Weiss, N. O. 1977, MNRAS, 179, 741

Moll, R., Cameron, R. H., & Schüssler, M. 2011, A&A, 533, A126

Molowny-Horas, R., & Yi, Z. 1994, Internal Rep. 31, Institute of Theoretical Astrophysics (Oslo: Univ. Oslo)

Muller, R. 1983, SoPh, 85, 113

Muller, R., & Roudier, T. 1984, SoPh, 94, 33

Muller, R., Hulot, J. C., & Roudier, T. 1989, SoPh, 119, 229

Muller, R., Auffret, H., Roudier, T., et al. 1992, Nature, 356, 322

Muller, R., & Roudier, T. 1992, SoPh, 141, 27

Muller, R., Dollfus, A., Montagne, M., Moity, J., & Vigneau, J. 2000, A&A, 359, 373

Nagata, S., Tsuneta, S., Suematsu, Y., et al. 2008, ApJL, 677, L145

Narayan, G., & Scharmer, G. B. 2010, A&A, 524, A3

Nordlund, Å. 1985, SoPh, 100, 209

Nordlund, Å., Stein, R. F., & Asplund, M. 2009, Living Reviews in Solar Physics, 6, 2

November, L. J., Toomre, J., Gebbie, K. B., & Simon, G. W. 1981, ApJL, 245, L123

November, L. J. 1986, AO, 25, 392

November, L. J., & Simon, G. W. 1988, ApJ, 333, 427

Orozco Suárez, D., Bellot Rubio, L. R., Del Toro Iniesta, J. C., et al. 2007a, PASJ, 59, 837

Orozco Suárez, D., Bellot Rubio, L. R., Del Toro Iniesta, J. C., et al. 2007b, ApJL, 670, L61

Orozco Suárez, D., & Bellot Rubio, L. R. 2012, ApJ, 751, 2

Orozco Suárez, D., Katsukawa, Y., & Bellot Rubio, L. R. 2012, ApJL, 758, L38

Park, S.-H., Tsiropoula, G., Kontogiannis, I., et al. 2016, A&A, 586, A25

Parker, E. N. 1963, ApJ, 138, 552

Parker, E. N. 1975, SoPh, 40, 291

Parker, E. N. 1978, ApJ, 221, 368

Parnell, C. E. 2002, MNRAS, 335, 389

Parnell, C. E., DeForest, C. E., Hagenaar, H. J., et al. 2009, ApJ, 698, 75

Parnell, C. E., & De Moortel, I. 2012, Royal Society of London Philosophical Transactions Series A, 370, 3217

Paxman, R. G., Seldin, J. H., Loefdahl, M. G., Scharmer, G. B., & Keller, C. U. 1996, ApJ, 466, 1087

Pesnell, W. D., Thompson, B. J., & Chamberlin, P. C. 2012, SoPh, 275, 3

Petrovay, K., & Szakaly, G. 1993, A&A, 274, 543

Piddington, J. H. 1975, APSS, 34, 347

Pötzi, W., & Brandt, P. N. 2005, Hvar Observatory Bulletin, 29, 61

Pötzi, W., & Brandt, P. N. 2007, Central European Astrophysical Bulletin, 31, 11

Press, W. H., Teukolsky, S. A., Vetterling, W. T., & Flannery, B. P. 1992, Cambridge: University Press, |c1992, 2nd ed.,

Priest, E. 2014, Magnetohydrodynamics of the Sun, by Eric Priest, Cambridge, UK: Cambridge University Press, 2014,

Quintero Noda, C., Martínez Pillet, V., Borrero, J. M., & Solanki, S. K. 2013, A&A, 558, A30

Quintero Noda, C., Ruiz Cobo, B., & Orozco Suárez, D. 2014, A&A, 566, AA139

Rast, M. P. 2003, ApJ, 597, 1200

Rees, D. E., Durrant, C. J., & Murphy, G. A. 1989, ApJ, 339, 1093

Rempel, M. 2014, ApJ, 789, 132

Requerey, I. S., Del Toro Iniesta, J. C., Bellot Rubio, L. R., et al. 2014, ApJ, 789, 6

Requerey, I. S., Del Toro Iniesta, J. C., Bellot Rubio, L. R., et al. 2015, ApJ, 810, 79

Rezaei, R., Steiner, O., Wedemeyer-Böhm, S., et al. 2007, A&A, 476, L33

Riethmüller, T. L., Solanki, S. K., Berdyugina, S. V., et al. 2014, A&A, 568, A13

Rieutord, M., Roudier, T., Malherbe, J. M., & Rincon, F. 2000, A&A, 357, 1063

Rieutord, M., & Rincon, F. 2010, Living Reviews in Solar Physics, 7, 2

Rimmele, T. R. 2004, ApJ, 604, 906

Roudier, T., Espagnet, O., Muller, R., & Vigneau, J. 1994, A&A, 287, 982

Roudier, T., Malherbe, J. M., Vigneau, J., & Pfeiffer, B. 1998, A&A, 330, 1136

Roudier, T., Lignières, F., Rieutord, M., Brandt, P. N., & Malherbe, J. M. 2003, A&A, 409, 299

Roudier, T., & Muller, R. 2004, A&A, 419, 757

Rouppe van der Voort, L. H. M., Hansteen, V. H., Carlsson, M., et al. 2005, A&A, 435, 327

Ruiz Cobo, B., & Del Toro Iniesta, J. C. 1992, ApJ, 398, 375

Ruiz Cobo, B., & Del Toro Iniesta, J. C. 1994, A&A, 283, 129

Sánchez Almeida, J., Bonet, J. A., Viticchié, B., & Del Moro, D. 2010, ApJL, 715, L26

Sánchez Almeida, J., & Lites, B. W. 2000, ApJ, 532, 1215

Sánchez Almeida, J., & Martínez González, M. 2011, Solar Polarization 6, 437, 451

Scharmer, G. B., Pettersson, L., Brown, D. S., & Rehn, J. 1985, AO, 24, 2558

Scherrer, P. H., Bogart, R. S., Bush, R. I., et al. 1995, SoPh, 162, 129

Scherrer, P. H., Schou, J., Bush, R. I., et al. 2012, SoPh, 275, 207

Schrijver, C. J., Title, A. M., van Ballegooijen, A. A., Hagenaar, H. J., & Shine, R. A. 1997, ApJ, 487, 424

Schüssler, M. 1984, A&A, 140, 453

Semel, M., & López Ariste, A. 1999, A&A, 342, 201

Shelyag, S., Keys, P., Mathioudakis, M., & Keenan, F. P. 2011, A&A, 526, A5

Shimizu, T., Lites, B. W., Katsukawa, Y., et al. 2008, ApJ, 680, 1467

Shine, R. A., Simon, G. W., & Hurlburt, N. E. 2000, SoPh, 193, 313

Simon, G. W., Title, A. M., Topka, K. P., et al. 1988, ApJ, 327, 964

Smithson, R. C. 1975, BAAS, 7, 346

Sobotka, M., Vázquez, M., Bonet, J. A., Hanslmeier, A., & Hirzberger, J. 1999, ApJ, 511, 436

Solanki, S. K., & Stenflo, J. O. 1984, A&A, 140, 185

Solanki, S. K. 1986, A&A, 168, 311

Solanki, S. K., Keller, C., & Stenflo, J. O. 1987, A&A, 188, 183

Solanki, S. K. 1993, ssr, 63, 1

Solanki, S. K., Barthol, P., Danilovic, S., et al. 2010, ApJL, 723, L127

Spruit, H. C. 1976, SoPh, 50, 269

Spruit, H. C. 1979, SoPh, 61, 363

Spruit, H. C., & Zweibel, E. G. 1979, SoPh, 62, 15

Spruit, H. C., Nordlund, Å., & Title, A. M. 1990, ARAA, 28, 263

Stein, R. F., & Nordlund, Å. 1998, ApJ, 499, 914

Stein, R. F., & Nordlund, Å. 2006, ApJ, 642, 1246

Steiner, O., Grossmann-Doerth, U., Schüssler, M., & Knölker, M. 1996, SoPh, 164, 223

Steiner, O., Grossmann-Doerth, U., Knölker, M., & Schüssler, M. 1998, ApJ, 495, 468

Steiner, O. 1999, in ASP Conf. Ser. 184, Third Advances in Solar Physics Euroconference: Magnetic Fields and Oscillations, ed. B. Schmieder, A. Hofmann, & J. Staude (San Francisco, CA: ASP), 38

Steiner, O., Franz, M., Bello González, N., et al. 2010, ApJL, 723, L180

Steiner, O., & Rezaei, R. 2012, Fifth Hinode Science Meeting, 456, 3

Stenflo, J. O. 1973, SoPh, 32, 41

Stenflo, J. O., & Harvey, J. W. 1985, SoPh, 95, 99

Stix, M. 2002, The sun : an introduction – 2nd ed. /Michael Stix. Berlin : Springer, 2002. QB 521 .S75,

Takeuchi, A. 1999, ApJ, 522, 518

Thornton, L. M., & Parnell, C. E. 2011, SoPh, 269, 13

Title, A. M., Tarbell, T. D., Topka, K. P., et al. 1989, ApJ, 336, 475

Title, A. M., Topka, K. P., Tarbell, T. D., et al. 1992, ApJ, 393, 782

Tsuneta, S., Ichimoto, K., Katsukawa, Y., et al. 2008, SoPh, 249, 167

Usoskin, I. G. 2013, Living Reviews in Solar Physics, 10, 1

Utz, D., Del Toro Iniesta, J. C., Bellot Rubio, L. R., et al. 2014, ApJ, 796, 79

Vargas Domínguez, S., Palacios, J., Balmaceda, L., Cabello, I., & Domingo, V. 2011, MNRAS, 416, 148

Vargas Domínguez, S., Palacios, J., Balmaceda, L., Cabello, I., & Domingo, V. 2015, SoPh, 290, 301

Verma, M., Steffen, M., & Denker, C. 2013, A&A, 555, A136

Viticchié, B., Del Moro, D., Berrilli, F., Bellot Rubio, L., & Tritschler, A. 2009, ApJL, 700, L145

Viticchié, B., Del Moro, D., Criscuoli, S., & Berrilli, F. 2010, ApJ, 723, 787

Vögler, A., Shelyag, S., Schüssler, M., et al. 2005, A&A, 429, 335

Vögler, A., & Schüssler, M. 2007, A&A, 465, L43

Wang, H., & Zirin, H. 1988, SoPh, 115, 205

Wang, J., Wang, H., Tang, F., Lee, J. W., & Zirin, H. 1995a, SoPh, 160, 277

Wang, Y., Noyes, R. W., Tarbell, T. D., & Title, A. M. 1995b, ApJ, 447, 419

Webb, A. R., & Roberts, B. 1978, SoPh, 59, 249

Wedemeyer-Böhm, S., & Rouppe van der Voort, L. 2009, A&A, 507, L9

Wedemeyer-Böhm, S., Scullion, E., Steiner, O., et al. 2012, Nature, 486, 505

Weiss, N. O. 1964, MNRAS, 128, 225

Weiss, N. O. 1966, Royal Soc. London Proc. Ser. A, 293, 310

Weiss, N. O., Brownjohn, D. P., Matthews, P. C., & Proctor, M. R. E. 1996, MNRAS, 283, 1153

Wiegelmann, T., Thalmann, J. K., & Solanki, S. K. 2014, A&A Revs, 22, 78

Wiehr, E. 1978, A&A, 69, 279

Yelles Chaouche, L., Moreno-Insertis, F., Martínez Pillet, V., et al. 2011, ApJL, 727, L30

Yi, Z. 1992, PhD thesis, University of Oslo, Oslo

Yi, Z., & Engvold, O. 1993, SoPh, 144, 1

Zhou, G. P., Wang, J. X., & Jin, C. L. 2010, SoPh, 267, 63

Zhou, G., Wang, J., & Jin, C. 2013, SoPh, 283, 273